UNIVERSITY OF CALIFORNIA SAN DIEGO

Multiscale Simulations of Complex Interfacial Dynamics

A dissertation submitted in partial satisfaction of the
requirements for the degree
Doctor of Philosophy

in

Engineering Sciences (Engineering Physics)

by

Nataliia Siuliukina

Committee in charge:

Professor Daniel M. Tartakovsky, Chair
Professor Prabhakar Bandaru, Co-Chair
Professor Marcos Intaglietta
Professor Ratneshwar Lal
Professor Kesong Yang

2018

The dissertation of Nataliia Siuliukina is approved, and it is acceptable in quality and form for publication on microfilm and electronically:

_____

_____

_____

_____
Co-Chair

_____
Chair

University of California, San Diego

2018

DEDICATION

To my family.

TABLE OF CONTENTS

LIST OF FIGURES

LIST OF TABLES

ACKNOWLEDGEMENTS

This work could not have been completed without the help of a great number of people. I would like to acknowledge Professor Daniel Tartakovsky for his support and guidance during the past five years. Through drafts of journal papers and dissertation his guidance was invaluable to me. His inspiration helped me to finish this research and to write this thesis. I could not have imagined having a better advisor and mentor for my Ph.D. study.

I would like to thank my mentors Boian S. Alexandrov and Velimir V. Vesselinov from my internship at Los Alamos National Laboratory for their wonderful collaboration. Boian, you supported me greatly and were always willing to help me. Thank you for all your guidance and countless conversations and ability to always be there for me no matter what it is. I would like to single out my another supervisor Monty for your excellent cooperation and for all of the opportunities I was given to conduct my research and further my dissertation at LANL.

The other members of my committee, Professors Prabhakar Bandaru, Ratneshwar Lal, Kesong Yang and Marcos Intaglietta, also kept me on the right path with their helpful suggestions and insightful comments.

Ludmil had to tolerate more than anyone should, but he was always there to help in every possible way. Without him, I never would have made it. I am also very grateful to my parents who miss me terribly by being so far way but always supported me in everything.

Above all, I would like to express sincere appreciation to the many friends and labmates who provided help, feedback, criticism, encouragement, and all the necessary and unnecessary advices.

The text of the dissertation includes the reprints of the following papers, either accepted or prepared for consideration at the time of publication. The dissertation author was primary investigator and author of these publications.

Chapter 2.

Natalia Siuliukina, Daniel M. Tartakovsky, ”A Hybrid Multiscale Model of Miscible Reactive

Fronts", *Water Resources Research*, 54, 2018.

Chapter 3.

Natalia Siuliukina, Daniel M. Tartakovsky, "Viscous Fingering in Non-Isothermal Filtration', *in preparation*.

Chapter 4.

Nataliia Siuliukina, Boian S. Alexandrov, "Global sensitivity analyses using a surrogate model based on support vector regression approach", *in preparation*.

VITA

2011	B. S. in Mathematics, Moscow State University, Moscow, Russia
2014	M. S. in Engineering Sciences (Engineering Physics), University of California San Diego
2018	Ph. D. in Engineering Sciences (Engineering Physics), University of California San Diego

PUBLICATIONS

Natalia Siuliukina, Daniel M. Tartakovsky, "A Hybrid Multiscale Model of Miscible Reactive Fronts", *Water Resources Research*, 54, 2018.

Natalia Siuliukina, Daniel M. Tartakovsky, "Viscous Fingering in Non-Isothermal Filtration", *in preparation*,

Nataliia Siuliukina, Boian S. Alexandrov, "Global sensitivity analyses using a surrogate model based on support vector regression approach", *in preparation*.

ABSTRACT OF THE DISSERTATION

Multiscale Simulations of Complex Interfacial Dynamics

by

Nataliia Siuliukina

Doctor of Philosophy in Engineering Sciences (Engineering Physics)

University of California, San Diego, 2018

Professor Daniel M. Tartakovsky, Chair
Professor Prabhakar Bandaru, Co-Chair

Subsurface processes represent a class of important phenomena that occurs in many natural and anthropogenic settings. This dissertation deals with mathematical modeling of multiscale subsurface processes. Subsurface processes can be simulated at multiple scales with variable degrees of fidelity. We investigate the effect of subsurface phenomena on macroscopic dynamics in three particular cases.

In Chapter 2, we consider microscopic (pore-scale) features of reactive transport that cannot be properly resolved in macroscopic (Darcy-scale) models. While microscopic descriptors might be closer to reality, they are computationally unfeasible when deployed on a macroscale.

Hybrid algorithms combine the physical fidelity of a microscopic model with the computational efficiency of its macroscopic counterpart. We develop a hybrid model of dynamic reactive fronts in an open fracture, with a chemical reaction occurring in the zone of contact between two dissolved species. Our numerical experiments demonstrate that the hybrid model outperforms its microscopic and macroscopic counterparts in terms of computational time and representational accuracy, respectively.

In Chapter 3, we consider the effect of temperature on interfacial dynamics where small fluctuations affect instabilities. Viscous fingering is a hydrodynamic instability that can be caused by a viscosity difference across a traveling thermal front. We investigate the problem of displacement stability in the filtration flow for two-phase filtration in the presence of heat transfer. Fingers instability was analyzed for isothermal and non-isothermal processes. Our synergistic numerical and theoretical investigation confirms the development of instability due to differences in viscosities. Our results demonstrate that controlling the stability of such a system requires exponentially lowering the fluid's viscosity when the temperature is increased.

Even by implementing multiple simplifying assumptions, most real-world problems are extremely complex and, therefore, quite costly to thoroughly analyze. In Chapter 4, we utilize a supporting vector regression (SVR) method to create a surrogate model, based on a limited amount of data, capable of describing the behavior of a set of wells with various input parameters. SVR is applied to analyze and to deconstruct the groundwater geochemistry observed in the regional aquifer for characterization of contaminant sources. Using synthetic and real-world data, we demonstrate that our SVR model is capable of accurately building a surrogate model using only a limited amount of experimental data and simulation results. Further, we demonstrate that global sensitivity analysis can be applied to our SVR model and it can produce accurate results at significantly lower computational cost.

Overall, this thesis investigates multiple aspects of multi-scale fluid dynamics by both developing physics-based numerical models and data-driven computational approaches.

Chapter 1

Introduction

1.0.1 Multi-scale modeling in subsurface and biological processes

Interfaces between two fluids occur everywhere, for example in natural environments or in industrial applications. The two-fluid flows development are powerful in many engineering applications. For example, the instability of fluid-fluid flows affects the spray combustion breakdown, the sea sprays breakdown, and carbon dioxide sequestration in oil recovery processes. A large amount of fluid dynamic problems involve dynamic interfaces. Some of the applications include dynamics of air and water, breaking surface waves , oil recovery problems and reacting flows in porous media.

Any mathematical or physical model is based on an general system simplification on a different scales. These models are solved with the assumptions that enable their formulation and predictive tool usage. To make a model with a certain accuracy we need to describe the behavior of the system and provide the necessary computational cost to solve the original model. Different models provide various performances in different regimes. Also, there are further complications in they systems when the prediction scales is much bigger than the governing equations scales are described. This problem is very common for flow and transport equations in porous media where the prediction scales are much larger than the scales where these equations are represented. We

are very interested in the following complex systems, since their characteristics are based on a large scale environments such as geologic formations to biological singe cells cells and from oil reservoir modeling on a field scale to nano products on a pore scale.

As a matter of our particular interest, the subsurface systems involve various processes taking place at a wide range of spatial and temporal scales. Subsurface systems have spatial scales with range from kilometers e.g., oil production and CO2 sequestration, and from meters to microns when dealing with a biological single cell or multiple cells when we are considering the problem of the spread of cancer.

Flow and transport in porous media can be modeled on a various scales: at the pore- (microscopic) or Darcy- (macroscopic) scales. The Darcy scale have a solid physical foundation and consists of Stokes equations for fluid flow and advection-reaction- diffusion equations (ARDEs) for solutes and transport; The Darcy-scale equations for flow and ARDEs for transport are impractical for large-scale simulations because of the lack of knowledge about the detailed pore geometry and high computational costs. The heterogeneity and uncertainty of most natural porous media, such as oil reservoirs and aquifers make pore scale simulations impractical in terms of the predictive tool at continuum scales that are many orders of magnitude larger than the pore scale.

Macroscopic models describe porous medium as an ”averaged continuum” and solve these constrains by relying on a set of simplified conditions which are required to solve equations for averaged flow velocity and solute concentrations, which provide Darcy-scale constrains of flow and transport in porous media. Such macroscopic models fail when some of these assumptions become violated where the heterogeneity in porous systems could lead to localized violation of homogenizability constrains in continuum models.

1.0.2 The porous medium

Fluids play a vary important role in a wide range of geological and biological processes. The advective transport of dissolved species is valuable in a many applications for geochemical transformations where contaminants travel through large distances in the subsurface or blood vessels as a result of fluid flow. Although many fractured and porous biological geological systems are saturated with a single fluid (water with a many dissolved minerals and gasses, blood with the contaminants), pore spaces and fractures are often occupied simultaneously by two and more fluids and gases.

Simulations of pore-phases in multiphase fluid flow are much more complicating than single phase flow simulations for several reasons: the complex dynamics of fluid-fluid interfaces has to be tracked fast and precisely and the behavior of multiphase fluids with large density and viscosity ratios is difficult to accurately simulate. Pore scale models have been used to simulate several cases of multiphase and single-phase fluid flow in porous media. However, pore models are based on simplified models using the pore space geometry and simplified physics assumptions. Also, pore models are not well developed for the simulation of multiphase fluid flow in heterogeneous porous media [58]. It is still not possible to accurately describe the multiphase fluid flow models for the large ratios of densities and viscosities. Due to the high scientific attention, multiphase fluid dynamics of moving fronts has been investigated using both experiments and computational methods by a large community of scientists and engineers. Consequently, a quite large number of methods have been developed to simulate multiphase fluid flow.

1.0.3 Types of displacement processes

Instabilities between interfaces develop at the interface between the displacing and the displaced fluids due to the growth of perturbations that forms complex interface topologies. These perturbations will grow and interact with one another in a non-linear way, affecting the

overall fluid flow and resulting displacement characteristics. The viscous fingering instability is an interfacial instability caused by a difference in the fluids' viscosity. If a high viscosity fluid is displacing the low viscosity fluid, perturbations that are greater than a certain wavelength develop instabilities along the fluid interface and promote the growth of a nonlinear displacements which affects the more viscous fluid ([21], [70]).

The development of viscous fingers is an important effect in many applications, such as the fluid flow in porous media, enhanced oil recovery [75], geothermal heat extraction [57] and carbon dioxide sequestration [94]. In these flows, the fluid-fluid front interface separate the displacing and the displaced fluid and front can be described as a smooth or sharp interface. In immiscible displacements the the fluid-fluid interface is sharp, well defined and controlled by viscous forces, where the fluid properties observe discontinues profiles, and in miscible displacements the front is smooth (due to the dispersion) and the diffusion is mixing the concentrations of both fluids [64]. Any process that helps to reduce instabilities or the control of the growth rate of viscous fingers, is the key importance for technology development.

During the immiscible displacement in porous media, the flow regime depends on the mobility ratio at the interface between the fluids which describes the viscous driving forces [10]. The motivation behind the current studies is propagation of the immiscible flows in porous media driven by the pressure gradient with the influence of variable temperature. There is an instability at the interface in the problem of the water-oil spreading, due to the deference in fluid properties, which can give rise to the viscous fingering phenomena. The injection of water will typically occur at a temperature different to that of the fracture creating temperature gradients in the domain that will alter mechanical fluid quantities such as viscosity, density and surface tension. The water may also be injected at a higher temperature than the oil in the fracture, for front evolution monitoring. The difference in temperatures can create a thermo-viscous fingering problem there the dependence of viscosity on temperature affects the mechanisms of the fingering process.

The observations of the viscous fingering process in a subsurface contaminant flow

caused several research attempts on viscous fingering in Hele-Shaw cells, studying the fluid flow between two separated plates [70]. The study of viscous fingering in Hele-Shaw cells is often used as the simplification approach for more complex problems in porous media, allowing the simplified models to describe mechanisms that control the viscous fingering regime [21]. In addition to analytical and numerical models, it is possible to dtudy fingering instabilities experimentally using a relatively simple Hele-Shaw cell setup.

The majority of existing studies have focused on isothermal displacements where both fluids are at the same temperature. Extensive reviews of theoretical, experimental, and numerical simulation studies can be found in the study of ([32]), [46], [67]).

The instability development is driven by the different viscosity ratios may vary as a result of a change in the flow temperature. The resulting instability may be observed under two conditions. In the first one, a fluid flows through a porous medium having a temperature different than that of the fluid. Such instability may be observed in magma flow in fissure eruptions, geothermal flows as well as flow of polymer melts in injection molding. In the second one, the two fluids are at two different temperatures resulting in two traveling fronts, a fluid front and a thermal front along which the instability may be observed. Such flows are encountered in many thermal enhanced oil recovery processes such as hot water flooding, steam flooding and hot solvent injection, as well as in some polymer processing systems.

Fingering problems operate on many spatial scales, such as pore scale and the Darcy-scale which triggers the existence of a characteristic macroscopic length scale or wavelength. We want to explore the linear stability stages of the viscous fingering instability in immiscible flows, and understand the mechanisms of the processes that can occur during the water-oil displacements within the inclusion of temperature dependence. By studying the problem of the two dimensional two phase filtration in a homogeneous fracture and using advanced numerical methods, the mechanisms for the instability in the linear stages of finger growth can be explicitly studied and the different thermal and structural effects explored in detail.

Kong et al. (1992) conducted one of the first research studies on this topic [51]. These authors developed the steam displacement problem of crude oils in vertical and horizontal Hele-Shaw cells. In their studies the steam tended to condense in contact with the cold oil. The authors also compared isothermal water-oil and non-isothermal steam-oil displacements problems.

In terms of mathematical or numerical modeling of the thermo-viscous fingering instability, there are not a lot of conducted studies. The first numerical study to research this instability was made by Saghir et al. (2000) [71]. These authors studied nonlinear double-diffusive convection in a vertical homogeneous porous medium, and applied the finite element methods for solving the fluid flow in porous media. They included Isothermal and non-isothermal displacements. Variations of the distance traveled by the base and the tip were studied for each case and not a lot of differences were conducted between the isothermal and non-isothermal cases. Pritchard (2004) analyzed the stability regimes of non-isothermal miscible displacements in a porous medium of radial geometry [64]. The author developed the stability of the fluid and thermal traveling fronts and since viscosity may change across each front, viscous fingering instability was observed on both fronts. In order to find the flow instability, the viscosity changes corresponding to thermal and concentration changes must be studied separately. In general, both variations were developing fingering instabilities however the growth rate could be varied by the coupling between the two thermal and solutal mechanisms. Recently, MN Islam, J Azaiez (2010) are fully examined the development of the thermo-viscous fingering instability of miscible displacements in homogeneous porous media [46].

1.0.4 Thesis aims and objectives

The focus of this dissertation is to investigate the problems of how subscale phenomena affects macroscopic dynamics of moving fronts. We developed three problems that deserved not a lot of attention. For the first problem in Chapter 2 we investigated the pore-scale/Darcy-scale, physics based model of moving reactive miscible fronts of bi-molecular reaction. The second

problem in Chapter 3 we developed the field scale model of immiscible two phase filtration of two displacing fluids with the inclusion of temperature. A third problem in Chapter 4 was chosen to be a data driven simulation of miscible displacement in contaminant flow where we are interested in the movement of the front and thus in creation of surrogate model capable of analyzing and deconstructing the groundwater geochemistry observed in the regional aquifer for characterization of contaminant sources. These case studies are lined to each other in various ways and at various spatial scales and serve as excellent test-beds in multi-scale mathematical modeling of fluid flow in subsurface environments.

The evolution of a reaction $A + B \rightarrow C$ in a spatially extended system is characterized by the propagation of reaction fronts that separate the species A and B. The motion of these fronts is well understood for reaction-diffusion systems in the absence of any substrate flow. The effects of fluid motion on fronts in the more general advection-reaction-diffusion system have only recently received significant attention. This is somewhat surprising, given the applicability of advection-reaction-diffusion to a wide range of systems, including microfluidic chemical reactors [29], plasmas [87], the dynamics of ecosystems in the oceans (e.g.,plankton blooms) [81], cellular- and embryonic-scale biological processes ([93], [86]), and the propagation of diseases in society [82]. Some microscopic (pore-scale) features of reactive transport cannot be properly resolved in macroscopic (Darcy-scale) models. While microscopic descriptors might be closer to reality, they are computationally unfeasible when deployed on a macroscale. Hybrid algorithms combine the physical fidelity of a microscopic model with the computational efficiency of its macroscopic counterpart. In Chapter 2 we develop a hybrid model of dynamic reactive fronts in an open fracture, with a chemical reaction occurring in the zone of contact between two dissolved species. Our numerical experiments demonstrate that the hybrid model outperforms its microscopic and macroscopic counterparts in terms of computational time and representational accuracy, respectively.

In chapter 3, we aim to model the 2D evolution of the water oil displacement process

in porous media and explore certain aspects of the displacement regime and viscous instability to better understand the underlying mechanisms that control the immiscible thermo viscous fingering process. We consider the effect on temperature on interfacial dynamics where small fluctuations affects instabilities. Viscous fingering is a hydrodynamic instability that can be caused by a viscosity difference across a traveling thermal front. We investigate the problem of displacement stability in the filtration flow for two-phase filtration in the presence of temperature. Fingers instability was analyzed for isothermal and non-isothermal processes. Were confirmed the results of theoretical investigations about the developing the instability due to the difference in viscosities. Results demonstrate that it's possible to control the the stability of the system when the increase of temperature causes the exponential lowering the viscosity of the fluid.

Even with the implementation of many simplifying assumptions, most real-world problems are extremely complex and therefore quite costly to analyze thoroughly. In Chapter 4, we utilize a Supporting Vector Regression (SVR) method for creation a surrogate model capable of describing the behavior of a set of wells with the various input parameters, based on a limited amount of data samples. SVR method is applied to analyze and deconstruct the groundwater geochemistry observed in the regional aquifer for characterization of contaminant sources. Using synthetic and real world site data, we demonstrate that SVR method is capable of accurately build a surrogate model of set of monitoring wells, using only a limited amount of experimental data and simulation results. A comprehensive analysis of the model's output and sensitivity indices via Global Sensitivity Analysis (GSA) method can be accurately calculated with much lower computational costs.

Chapter 2

A Hybrid Multiscale Model of Miscible Reactive Fronts

2.1 Introduction

Reaction fronts moving with a fluid are a characteristic feature of many physical, chemical and biological processes [24, 26, 32, 49]. This phenomenon occurs when a fluid with a dissolved species A displaces a fluid (the same or different) with a dissolved species B. A chemical reaction, e.g., $A + B \rightarrow C$, occurs within a spatially localized region (a "front") separating these two solutions. The position and width of this front change with time due to fluid flow, molecular diffusion, and hydrodynamic dispersion. While localized reaction fronts might occupy a minuscule fraction of a flow domain, their effects on flow transport can be felt over much larger regions [36].

Like all subsurface flow and transport processes, dynamic reaction fronts can be described with either pore-scale (microscopic) or Darcy-scale (macroscopic) models. The former have a solid physical foundation consisting of Stokes equations for flow and advection-reaction-diffusion equations for transport; yet they are impractical for large-scale simulations of practical

interest because of the lack of knowledge about pore geometry and prohibitively high computational cost. A set of simplifying assumptions is required to derive equations for average flow velocity (Darcy's law) and solute concentration (advection-dispersion equation or ADE), which provide Darcy-scale descriptors of flow and transport in porous media. Such macroscopic models fail when some of these assumptions become invalid ([11], [15]). If the failure of macroscopic models is confined to a small region of a computational domain, hybrid pore-scale/Darcy-scale algorithms [82] allow one to combine the high-fidelity of microscopic models with the computational efficiency of their macroscopic counterparts. Hybrid algorithms yield accurate predictions, while keeping computational cost relatively low by restricting microscopic simulations in subdomains where macroscopic models break down and solving macroscopic equations in the rest of the computational domain [3], [4], [5], [83]. Hybrid algorithms for subsurface applications have been developed by [9, 12, 69, 79, 84]. In these and other similar analyses, the micro- and macroscopic simulation domains are fixed in space.

A major goal of our analysis is to develop a hybrid model of dynamic reactive fronts, which involve two dissolved species undergoing a nonlinear homogeneous reaction to produce another solute. A set of numerical experiments is performed to investigate the validity of the homogenizability conditions for multicomponent reactive flow in a horizontal open fracture. When these conditions are not met, we deploy the hybrid algorithm that couples a pore-scale model in the vicinity of a moving reaction front with a corresponding Darcy-scale model elsewhere in the fracture. The two models are coupled via an iterative procedure, which enforces the continuity of concentrations and mass fluxes across the interface between the two models.

Section 2.2 contains pore- and Darcy-scale formulations of flow and reactive transport in both general porous media and an open fracture; it also summarizes, in the form of a phase diagram in the space of Péclet and Damköhler numbers, the conditions under which the Darcy-scale model becomes invalid. In section 2.3 we develop our hybrid algorithm for dynamic reactive fronts. In section 2.4 we report results of our numerical experiments in various transport

regimes, including those under which the Darcy-scale model becomes invalid and either the pore-scale model or the hybrid must be used. The relative performance of the three modeling strategies is compared in terms of both accuracy and computational time. Main conclusions drawn from our study are presented in section 2.6.

2.2 Problem Formulation

We consider both pore-scale and Darcy-scale descriptions of fluid flow and reactive solute transport in a generic porous medium $\hat{\Omega}$. The material's pore space, denoted by $\hat{\Re} \subset \hat{\Omega}$, is fully saturated with a fluid of dynamic viscosity μ. The (multi-connected) solid-fluid interface is denoted by $\hat{\Gamma}$. The fluid is a dilute solution of two chemical species A and B, which undergo an irreversible fast bimolecular reaction,

$$A + B \xrightarrow{k} C, \tag{2.1}$$

to form the reaction product C with the homogeneous reaction rate constant k [L/T]. We assume that this chemical reaction does not alter the pore space $\hat{\Re}$ and, hence, does not affect the flow velocity.

The pore-scale molar concentrations of the dissolved species A, B and C are denoted by $\hat{c}_i$ [M/L^3], where $i = A, B$ and C, respectively. The corresponding Darcy-scale concentrations $\hat{C}_i$ [M/L^3] are averages of $\hat{c}_i$ over a representative elementary volume $\hat{\mathcal{V}} \subset \hat{\Omega}$ centered around a point $\mathbf{x}$,

$$\hat{C}_i(\mathbf{x},t) = \frac{1}{\|\hat{\mathcal{V}}\|} \int_{\hat{\mathcal{V}}(\mathbf{x})} \hat{c}_i(\mathbf{y},t) \mathrm{d}\mathbf{y}, \qquad i = A, B, C. \tag{2.2}$$

A characteristic length of $\hat{\mathcal{V}}$, ℓ, is much smaller than that of $\hat{\Omega}$, $\ell \ll L$, so that $\varepsilon \equiv \ell / L \ll 1$. Equations describing the spatiotemporal evolution of $\hat{c}_i(\hat{\mathbf{x}},\hat{t})$ and $\hat{C}_i(\hat{\mathbf{x}},\hat{t})$ are described below.

Consider reactive transport in an open fracture $\hat{\Omega}$ with a characteristic length L. Let us assume that the fracture has microscopical representation by the set of unit cells $\hat{Y}$ whose characteristic length scale is l such that $\varepsilon \equiv l \leq 1$. The medium consists of the spaces $\hat{\Re}$ of each cell $\hat{Y}$ and the impermeable solid matrix $\hat{G}$ such that $\hat{\Omega} = \hat{\Re} \cup \hat{G}$. The smooth multi-connected boundary between space $\hat{\Re}$ and the solid matrix $\hat{G}$ is denoted by the surface $\hat{\Gamma}$.

2.2.1 Pore-Scale Equations

Steady-state pressure-driven single-phase incompressible fluid flow is described by Stokes and continuity equations,

$$\mu \hat{\nabla}^2 \hat{\mathbf{v}} - \hat{\nabla} \hat{p} = \mathbf{0}, \tag{2.3}$$

$$\hat{\nabla} \cdot \hat{\mathbf{v}} = 0, \qquad \hat{\mathbf{x}} \in \hat{\Re}, \tag{2.4}$$

where $\hat{\mathbf{v}}(\hat{\mathbf{x}})$ is the fluid velocity, $\hat{p}(\hat{\mathbf{x}})$ is the fluid pressure, and $\hat{\mathbf{x}}$ is a point in $\hat{\Re}$. Flow equations (2.3) are subject to no-slip boundary conditions on the impermeable solid-fluid interface $\hat{\Gamma}$, i.e., $\hat{\mathbf{v}} = \mathbf{0}$ for $\hat{\mathbf{x}} \in \hat{\Gamma}$.

The pore-scale concentrations $\hat{c}_i(\hat{\mathbf{x}}, t)$ are described by a system of coupled advection-diffusion-reaction equations,

$$\frac{\partial \hat{c}_A}{\partial \hat{t}} + \hat{\nabla} \cdot (\hat{\mathbf{v}} \hat{c}_A) = D \hat{\nabla}^2 \hat{c}_A - k \hat{c}_A \hat{c}_B, \qquad \hat{\mathbf{x}} \in \hat{\Re}, \qquad \hat{t} > 0 \tag{2.5a}$$

$$\frac{\partial \hat{c}_B}{\partial \hat{t}} + \hat{\nabla} \cdot (\hat{\mathbf{v}} \hat{c}_B) = D \hat{\nabla}^2 \hat{c}_B - k \hat{c}_A \hat{c}_B, \qquad \hat{\mathbf{x}} \in \hat{\Re}, \qquad \hat{t} > 0 \tag{2.5b}$$

and

$$\frac{\partial \hat{c}_C}{\partial \hat{t}} + \hat{\nabla} \cdot (\hat{\mathbf{v}} \hat{c}_C) = D \hat{\nabla}^2 \hat{c}_C + k \hat{c}_A \hat{c}_B, \qquad \hat{\mathbf{x}} \in \hat{\Re}, \qquad \hat{t} > 0. \tag{2.5c}$$

Here, for the sake of simplicity and without loss of generality, we assume that the three dissolved species have the same molecular diffusion coefficient D [L^2/T]. Transport equations (2.5) are subject to no-flux boundary conditions on the solid-fluid interface $\hat{\Gamma}$ with unit normal vector $\hat{\mathbf{n}}(\mathbf{x})$,

$$\hat{\mathbf{n}} \cdot \hat{\nabla} \hat{c}_i = 0, \quad i = A,B,C; \qquad \hat{\mathbf{x}} \in \hat{\Gamma}. \tag{2.6a}$$

and initial conditions

$$\hat{c}_i(\hat{\mathbf{x}},0) = \hat{c}_{\text{in},i}, \quad i = A,B,C; \qquad \hat{\mathbf{x}} \in \hat{\Re} \tag{2.6b}$$

where $\hat{c}_{\text{in},i}(\hat{\mathbf{x}})$ are known (possibly spatially varying) initial concentrations.

2.2.2 Dimensionless Formulation.

Let L and v denote characteristic length and characteristic velocity magnitude, respectively; and set $c^\star = \max\{\hat{c}_{\text{in},A}, \hat{c}_{\text{in},B}\}$. We introduce dimensionless parameters and independent and dependent variables,

$$\text{Pe} = \frac{vL}{D}, \quad \text{Da} = \frac{L^2 k c^\star}{D}, \quad \mathbf{x} = \frac{\hat{\mathbf{x}}}{L}, \quad t = \frac{\hat{t}D}{L^2}, \quad \mathbf{v} = \frac{\hat{\mathbf{v}}}{v}, \quad p = \frac{\hat{p} l^2}{\mu v L}, \quad c_i = \frac{\hat{c}_i}{c^\star}. \tag{2.7}$$

The Péclet number $\text{Pe} = t_\text{d}/t_\text{a}$ represents the ratio between the diffusion ($t_\text{d} = L^2/D$) and advection ($t_\text{a} = L/v$) time scales, while the Damköhler number $\text{Da} = t_\text{d}/t_\text{r}$ is defined as the ratio between the diffusion and reaction ($t_\text{r} = 1/kc^\star$) time scales. (This scaling of pressure $\hat{p}$ ensures that the rescaled viscous term has the same order of magnitude of as that in the Stokes original equations.) We also introduce a space variable $\mathbf{y}$ defined in the unit cell Y and dimensionless

time $t = \hat{t}/\hat{t}_d$ and time variables associated with advection and reaction

$$\mathbf{y} = \varepsilon^{-1}\mathbf{x}, \quad t_a = \mathrm{Pe}\, t = \varepsilon^{-\alpha} t, \quad t_r = \mathrm{Da}\, t = \varepsilon^{\beta} t, \tag{2.8}$$

where α and β are determining the system's behavior. Rewriting (2.3) and (2.5) in terms of the dimensionless quantities (3.4) yields a dimensionless form of the governing equations

$$\varepsilon^2 \nabla^2 \mathbf{v} - \nabla p = \mathbf{0}, \qquad \nabla \cdot \mathbf{v} = 0, \qquad \mathbf{x} \in \Re; \tag{2.9}$$

and

$$\frac{\partial c_A}{\partial t} + \mathrm{Pe}\nabla \cdot (\mathbf{v} c_A) = \nabla^2 c_A - \mathrm{Da}\, c_A c_B, \qquad \mathbf{x} \in \Re, \quad t > 0, \tag{2.10a}$$

$$\frac{\partial c_B}{\partial t} + \mathrm{Pe}\nabla \cdot (\mathbf{v} c_B) = \nabla^2 c_B - \mathrm{Da}\, c_A c_B, \qquad \mathbf{x} \in \Re, \quad t > 0, \tag{2.10b}$$

and

$$\frac{\partial c_C}{\partial t} + \mathrm{Pe}\nabla \cdot (\mathbf{v} c_C) = \nabla^2 c_C + \mathrm{Da}\, c_A c_B, \qquad \mathbf{x} \in \Re, \qquad t > 0, \tag{2.10c}$$

subject to the correspondingly rescaled initial and boundary conditions.

$$c_{A_m}(\mathbf{x}, 0) = A_0(\mathbf{x}), \qquad c_{B_m}(\mathbf{x}, 0) = B_0(\mathbf{x}), \qquad c_{C_m}(\mathbf{x}, 0) = C_0(\mathbf{x}), \tag{2.11a}$$

$$\mathbf{n} \cdot \nabla c_{A_m} = \mathbf{n} \cdot \nabla c_{B_m} = \mathbf{n} \cdot \nabla c_{C_m} = 0. \tag{2.11b}$$

2.2.3 Darcy-Scale Equations

The macroscale flow and transport equations can be derived from their microscopic analogue by numerous homogenization (upscaling) techniques. One of the methods for homogenization uses the multiple-scale expansions to upscale transport equations from the micro to

macroscale and to operate with the averaged velocity and averaged concentrations. The method of multiple-scale expansions represent concentrations and velocity as an asymptotic series in powers of separation of scales parameter ε. Using this method it was shown that [11, 15] the microscopic reactive transport processes described by (2.10) and (2.11a) can be homogenized, i.e., approximated up to the order ε^2 and the macroscopic concentrations satisfies ARDEs Under certain conditions on Pe and Da, the spatial averaging of pore-scale equations (2.9) and (2.10) yields Darcy-scale (advection-dispersion-reaction) equations for the dimensionless macroscopic concentrations $C_i = \hat{C}_i/c^\star$,

$$\frac{\partial C_A}{\partial t} + \mathrm{Pe}\nabla\cdot(\mathbf{V}C_A) = \nabla\cdot(\mathbf{D}\nabla C_A) - \mathrm{Da}C_AC_B, \qquad \mathbf{x}\in\Omega, \quad t>0 \tag{2.12a}$$

$$\frac{\partial C_B}{\partial t} + \mathrm{Pe}\nabla\cdot(\mathbf{V}C_B) = \nabla\cdot(\mathbf{D}\nabla C_B) - \mathrm{Da}C_AC_B, \qquad \mathbf{x}\in\Omega, \quad t>0 \tag{2.12b}$$

and

$$\frac{\partial C_C}{\partial t} + \mathrm{Pe}\nabla\cdot(\mathbf{V}C_C) = \nabla\cdot(\mathbf{D}\nabla C_C) + \mathrm{Da}C_AC_B. \tag{2.12c}$$

Here $\mathbf{V}(\mathbf{x})$ is the Darcy flux (macroscopic velocity) computed by solving the groundwater flow equation, and $\mathbf{D}(\mathbf{U})$ is the dispersion coefficient tensor. Specifically, equations (2.12) are valid if [15]

$$\varepsilon \ll 1, \qquad \mathrm{Pe} < \varepsilon^{-2}, \qquad \mathrm{Da} < \varepsilon^{-2}, \qquad \mathrm{Da}/\mathrm{Pe} < \varepsilon^{-1}. \tag{2.13}$$

- The inequality $\varepsilon \ll 1$ is a condition that ensures spatial-scale separation,
- $\mathrm{Pe} < \varepsilon^{-2}$ ensures that the system is not dominated by advection at the microscale,
- $\mathrm{Da} < \varepsilon^{-2}$ is the sufficient condition for good mixing of the reactants,
- the condition $\mathrm{Da}/\mathrm{Pe} < \varepsilon^{-1}$ imposes a constraint on the advective and reactive time scales.

Combining all these conditions we impose the lower and upper bounds on the order of magnitude of Pe for any given Da.

These sufficient conditions delineate a homogenizability region in a two-dimensional Pe-Da space (Figure 4.3), where equations (2.12) are valid. The validity is guaranteed inside the region and not guaranteed outside.

Dynamic reactive fronts provide a challenging illustration of the possible breakdown of Darcy-scale models. Let us suppose that, at time $t = 0$, the solutes A and B occupy distinct subdomains Ω_A and Ω_B ($\Omega = \Omega_A \cup \Omega_B$), which are separated by an interface $\gamma = \Omega_A \cap \Omega_B$. This situation translates into (dimensionless) initial concentrations

$$C_{\text{in},A} = \begin{cases} 1 & \mathbf{x} \in \Omega_A \\ 0 & \mathbf{x} \in \Omega_B \end{cases} \quad \text{and} \quad C_{\text{in},B} = \begin{cases} 0 & \mathbf{x} \in \Omega_A \\ 1 & \mathbf{x} \in \Omega_B \end{cases}. \tag{2.14}$$

The reaction $A + B \to C$ takes place only in the immediate vicinity of the interface γ, which both is advected with the flow, $\gamma = \gamma(\mathbf{x}, t)$, and diffuses due to hydrodynamic dispersion. High concentration gradients in this diffuse reactive front can invalidate some of the homogenizability conditions (2.13), leading to a local breakdown of the Darcy-scale transport model (2.12). Our study has three interconnected objectives. First, we identify flow and transport regimes in which the breakdown indeed occurs, as predicted by the theory [15]. Second, we demonstrate that under these conditions no amount of mesh refinement around the front, used to numerically solve (2.12), can remedy the model's inadequacy. Third, we show that the hybrid model outperforms its microscopic and macroscopic counterparts in terms of computational time and representational accuracy, respectively. These objectives are achieved via numerical experimentation with diffusive reactive fronts propagating through an open fracture.

2.2.4 Pore- and Darcy-Scale Models of Front Propagation in Fractures

Consider an open fracture of length L and width $2w$, such that $\hat{\Omega} = \{\hat{\mathbf{x}} = (\hat{x},\hat{y})^\top : 0 < \hat{x} < L, -w < \hat{y} < w\}$. Flow is driven by the externally imposed pressure gradient $-J$ imposed in the $\hat{x}$ direction.

2.2.5 Pore-Scale Model.

Making use of the dimensionless quantities (3.4) and neglecting the boundary effects close to the fracture's entrance and exit, the solution of (2.9) in the rescaled fracture domain $\Omega = \{\mathbf{x} = (x,y)^\top : 0 < x < 1, -\varepsilon < y < \varepsilon\}$ is given by Poiseuille's formula $\mathbf{v} = (u,0)^\top$ with

$$u(y) = \frac{3}{2}\left(1 - \frac{y^2}{\varepsilon^2}\right), \qquad \varepsilon \equiv w/L. \tag{2.15}$$

(A dimensional form of Poiseuille's law obtained by solving (2.3) reads $\hat{u}(y) = J\varepsilon^2(1 - y^2/\varepsilon^2)/(2\mu)$. The average (characteristic) flow velocity is $v = (2\varepsilon)^{-1}\int_{-\varepsilon}^{\varepsilon}\hat{u}(y)\mathrm{d}y = J\varepsilon^2/(3\mu)$. The definition of the dimensionless velocity in (3.4), $u = \hat{u}/v$, gives (2.15).) Pore-scale transport equations (2.10) reduce to

$$\frac{\partial c_A}{\partial t} + \mathrm{Pe}\, u\frac{\partial c_A}{\partial x} = \frac{\partial^2 c_A}{\partial x^2} + \frac{\partial^2 c_A}{\partial y^2} - \mathrm{Da}\, c_A c_B, \qquad \mathbf{x} \in \Omega, \quad t > 0 \tag{2.16a}$$

$$\frac{\partial c_B}{\partial t} + \mathrm{Pe}\, u\frac{\partial c_B}{\partial x} = \frac{\partial^2 c_B}{\partial x^2} + \frac{\partial^2 c_B}{\partial y^2} - \mathrm{Da}\, c_A c_B, \qquad \mathbf{x} \in \Omega, \quad t > 0 \tag{2.16b}$$

and

$$\frac{\partial c_C}{\partial t} + \mathrm{Pe}\, u\frac{\partial c_C}{\partial x} = \frac{\partial^2 c_C}{\partial x^2} + \frac{\partial^2 c_C}{\partial y^2} + \mathrm{Da}\, c_A c_B. \tag{2.16c}$$

Initial conditions leading to formation of a localized reactive front, (2.14), become

$$c_A(\mathbf{x},0) = \begin{cases} 1 & x \le x_0 \\ 0 & x > 0 \end{cases}, \qquad c_B(\mathbf{x},0) = \begin{cases} 0 & x \le x_0 \\ 1 & x > 0 \end{cases}, \qquad c_C(\mathbf{x},0) = \frac{1}{4}, \tag{2.17}$$

where x_0 is an initial position front $\gamma(t)$. Boundary conditions at the fractures' inlet and outlet are

$$c_A(0,y,t) = 1, \qquad c_A(1,y,t) = 0, \qquad |y| < \varepsilon, \quad t > 0; \tag{2.18a}$$

$$c_B(1,y,t) = 0, \qquad c_B(0,y,t) = 1, \qquad |y| < \varepsilon, \quad t > 0; \tag{2.18b}$$

$$c_C(0,y,t) = \frac{1}{4}, \qquad c_C(1,y,t) = \frac{1}{4}, \qquad |y| < \varepsilon, \quad t > 0. \tag{2.18c}$$

Boundary conditions at the fracture's walls are

$$\frac{\partial c_i}{\partial y}(x,\pm\varepsilon,t) = 0, \quad i = A,B,C; \qquad 0 < x < 1, \quad t > 0. \tag{2.19}$$

2.2.6 Darcy-Scale Model.

The (dimensionless) Darcy-scale concentrations $C_i(x,t)$ satisfy transport equations (2.12), which for the problem under consideration reduce to

$$\frac{\partial C_A}{\partial t} + \mathrm{Pe}\frac{\partial C_A}{\partial x} = \mathcal{D}\frac{\partial^2 C_A}{\partial x^2} - \mathrm{Da}\, C_A C_B, \qquad 0 < x < 1, \quad t > 0 \tag{2.20a}$$

$$\frac{\partial C_B}{\partial t} + \mathrm{Pe}\frac{\partial C_B}{\partial x} = \mathcal{D}\frac{\partial^2 C_B}{\partial x^2} - \mathrm{Da}\, C_A C_B, \qquad 0 < x < 1, \quad t > 0 \tag{2.20b}$$

and

$$\frac{\partial C_C}{\partial t} + \mathrm{Pe}\frac{\partial C_C}{\partial x} = \mathcal{D}\frac{\partial^2 C_C}{\partial x^2} + \mathrm{Da}\, C_A C_B, \quad i = A,B; \qquad 0 < x < 1, \quad t > 0. \tag{2.20c}$$

2.2.7 Effective Dispersion parameter

The dispersion coefficient is now given by $\mathcal{D} = 1 + 2\varepsilon^2 \mathrm{Pe}^2/105$ [15]. Equations (2.20) are subject to initial conditions

$$C_A(x,0) = \begin{cases} 1 & x \le x_0 \\ 0 & x > x_0 \end{cases}, \qquad C_B(x,0) = \begin{cases} 0 & x \le x_0 \\ 1 & x > x_0 \end{cases}, \qquad C_C(x,0) = \frac{1}{4} \tag{2.21}$$

and boundary conditions

$$C_A(0,t) = 1, \quad C_A(1,t) = 0, \quad C_B(1,t) = 0, \quad C_B(0,t) = 1, \quad C_C(0,t) = \frac{1}{4}, \quad C_C(1,t) = \frac{1}{4}. \tag{2.22}$$

A solution of Darcy-scale model (2.20)–(2.17), $C_i(x,y,t)$ with $i = A,B$ and C, is consistent with its pore-scale counterpart (2.16)–(2.19), $c_i(x,y,t)$ with $i = A,B$ and C, if they satisfy the definition of Darcy-scale concentration (2.2),

$$\bar{c}_i(x,t) = \frac{1}{2\varepsilon} \int_{-\varepsilon}^{\varepsilon} c_i(x,y,t)\mathrm{d}y, \qquad i = A,B,C; \tag{2.23}$$

i.e., if $C_i(x,t) = \bar{c}_i(x,t)$ for $i = A,B$ and C.

2.3 Hybrid Models of Dynamic Reactive Fronts

We present a general formulation of our hybrid model in section 2.3.1 and its implementation for transport in fractures in section 2.3.2.

2.3.1 General Hybrid Formulation

Let us suppose that, in the immediate neighborhood $\mathcal{N}_\delta[\gamma(\mathbf{x},t)]$ of the reactive front's core $\gamma(\mathbf{x},t)$, macroscopic equations (2.12) become invalid because some of the conditions in (2.13) are violated (see section 2.2.3). The dynamics of $\gamma(\mathbf{x},t)$ is determined by advection, while the envelope $\partial\mathcal{N}_\delta(\mathbf{x},t) = \gamma(\mathbf{x},t) \pm \delta(\mathbf{x})$ represents the diffusive nature of dynamic reactive fronts. While the width of the reaction zone increases with time, we keep the width of $\mathcal{N}_\delta[\gamma(\mathbf{x},t)]$ constant and set to $\delta \sim \sqrt{\|\mathbf{D}\|\Delta t}$ where Δt is a time step of the Darcy-scale simulations. That is because the concentration gradients in the outer edges of the diffuse reaction front are sufficiently small for the Darcy-scale model to be valid. The pore-scale model (2.9)–(2.10) is solved inside $\mathcal{N}_\delta[\gamma(\mathbf{x},t)]$, and the Darcy-scale model (2.12) is solved elsewhere in the computational domain. The two models are coupled by enforcing the continuity of concentrations and the normal component of mass flux along the envelope $\partial\mathcal{N}_\delta$,

$$C_i(\mathbf{x},t) = \frac{1}{\|\partial\mathcal{N}_\delta(\mathbf{x},t)\|} \int\limits_{\partial\mathcal{N}_\delta(\mathbf{x},t)} c_i(s,t)\mathrm{d}s, \tag{2.24}$$

$$J_i(\mathbf{x},t) = \frac{1}{\|\partial\mathcal{N}_\delta(\mathbf{x},t)\|} \int\limits_{\partial\mathcal{N}_\delta(\mathbf{x},t)} j_i(s,t)\mathrm{d}s, \tag{2.25}$$

for $i = A, B$ and C. Here j_i and J_i are the normal components of the pore- and Darcy-scale dimensionless mass fluxes

$$\mathbf{j}_i = \mathbf{v}c_i - \nabla c_i$$

and

$$\mathbf{J}_i = \mathbf{V}C_i - \mathbf{D}\nabla C_i,$$

respectively. The coordinate $\mathbf{x}$ designates a segment of $\partial\mathcal{N}_\delta(\mathbf{x},t)$ that falls within the corresponding element of a numerical mesh used in the Darcy-scale computation.

2.3.2 Hybrid Model of Front Propagation in Fractures

The Darcy-scale description (2.20)–(2.17) reduces the front's core $\gamma(\mathbf{x},t)$ to a single point $x_{\rm f}(t)$. Starting with its initial position $x_{\rm f}(0)=x_0$, the core propagates with dimensionless velocity Pe, so that $\mathrm{d}x_{\rm f}/\mathrm{d}t = \mathrm{Pe}$. The domain of pore-scale model (2.15)–(2.19) becomes $\mathcal{N}_\delta = \{\mathbf{x} : x_{\rm f}(t)-\delta < x < x_{\rm f}(t)+\delta, -\varepsilon < y < \varepsilon\}$ with the envelope consisting of two segments, $\partial\mathcal{N}_\delta = \{(x,y) : x_{\rm f}(t)\pm\delta, -\varepsilon < y < \varepsilon\}$. Setting $\delta = m\sqrt{\mathcal{D}\Delta t}$, these points are given by

$$a(t) = x_{\rm f}(t) - m\sqrt{D\triangle t}, \tag{2.26}$$

$$b(t) = x_{\rm f}(t) + m\sqrt{D\triangle t} \tag{2.27}$$

where the coefficient m defines the dimensionless width of $\mathcal{N}_\delta$ (Figure 2.2). In the simulations reported below we set $m = 2800$, which corresponds to $\mathcal{N}_\delta$ occupying 20% of the whole simulation domain Ω. The Darcy-scale model (2.20)–(2.17) is solved in the rest of the fracture $\mathcal{N}_\delta^c = \{x : 0 < x < a(t), b(t) < x < 1\}$. The continuity conditions (2.24) used to couple the pore- and Darcy-scale simulations take the form,

$$C_i(x,t) = \frac{1}{2\varepsilon}\int_{-\varepsilon}^{\varepsilon} c_i(y,t)\mathrm{d}y, \tag{2.28}$$

$$J_i(x,t) = \frac{1}{2\varepsilon}\int_{-\varepsilon}^{\varepsilon} j_i(y,t)\mathrm{d}y, \tag{2.29}$$

$$\text{for} \quad x = a(t), b(t). \tag{2.30}$$

Our hybrid algorithm consists of the following steps.

1. Initiate simulations by setting $t=0$ and $x_{\rm f}(0)=x_0$; and by making an initial guess of the concentration values at $x=a$ and $x=b$, $\mathcal{C}_{a,i}$ and $\mathcal{C}_{b,i}$ with $i=A,B$ and C, respectively. (In the simulations reported below, we set $\mathcal{C}_{a,A}=0.8$, $\mathcal{C}_{a,B}=0.2$, $\mathcal{C}_{a,C}=0.5$, $\mathcal{C}_{b,A}=0.2$, $\mathcal{C}_{b,B}=0.8$, and $\mathcal{C}_{b,C}=0.5$.)

2. Compute $a(t)$ and $b(t)$ from (2.26), and assign pore- and Darcy-scale internal boundary conditions

$$c_i(a,y,t) = C_i(a,t) = \mathcal{C}_{a,i}, \qquad c_i(b,y,t) = C_i(b,t) = \mathcal{C}_{b,i}, \qquad i = A,B,C.$$

3. Solve the pore-scale equations (2.16) on domain $\mathcal{N}_\delta = \{x : a(t) < x < b(t), -\varepsilon < y < \varepsilon\}$. These equations are subject to initial and boundary conditions (2.17)–(2.19), which are supplemented with the interfacial conditions at $x = a(t)$ and $x = b(t)$ from step 2.

4. Solve the Darcy-scale equations (2.20) on domain $\mathcal{N}_\delta^c = \{x : 0 < x < a(t) \cup b(t) < x < 1\}$. These equations are subject to initial and boundary conditions (2.21) and (2.17), which are supplemented with the interfacial conditions at $x = a(t)$ and $x = b(t)$ from step 2.

5. Calculate pore-scale interfacial fluxes

$$j_i(x,y,t) = -\frac{\partial c_i}{\partial x}(x,y,t) + \mathrm{Pe}\, u(y)\mathcal{C}_{x,i}, \qquad x = a,b, \qquad i = A,B,C,$$

where $u(y)$ is given by (2.15) and $c_i(x,y,t)$ ($i = A,B$ and C) are computed in step 3. Evaluate average pore-scale interfacial fluxes

$$\bar{j}_i(x,t) = \frac{1}{2\varepsilon}\int_{-\varepsilon}^{\varepsilon} j_i(x,y,t)\mathrm{d}y, \qquad x = a,b, \qquad i = A,B,C.$$

Calculate Darcy-scale interfacial fluxes

$$J_i(x,t) = -\mathcal{D}\frac{\partial C_i}{\partial x}(x,t) + \mathrm{Pe}\, \mathcal{C}_{x,i}, \qquad x = a,b, \qquad i = A,B,C,$$

where $C_i(x,t)$ ($i = A,B$ and C) are computed in step 4.

6. Find the values of $\mathcal{C}_{a,i}$ and $\mathcal{C}_{b,i}$ ($i = A,B$ and C) that enforce the continuity conditions (2.28)

by solving an optimization problem

$$\underset{C_{a,i},C_{b,i}}{\operatorname{argmin}} \sqrt{\sum_{i=A,B,C} \left\{ [\bar{j}_i(a,t) - J_i(a,t)]^2 + [\bar{j}_i(b,t) - J_i(b,t)]^2 \right\}}.$$

In the simulations reported below we used the Matlab optimization procedure `fmincon` with convergence error of 10^{-9} to solve this problem.

7. Set $t = t + \Delta t$, advance the front's core $x_{\mathrm{f}}(t+\Delta t) = x_{\mathrm{f}}(t) + \mathrm{Pe}\,\Delta t$, and go to step 2.

2.4 Simulation Results

We use the Crank-Nicolson scheme with the upwind method for advection terms to solve both the pore-scale problem (2.16) and Darcy-scale (2.20) problems. The former was first solved on domain $\Omega = \{\mathbf{x} = (x,y)^\top : 0 < x < 1,\ -\varepsilon < y < \varepsilon = 0.0625\}$ discretized by a uniform mesh of size $\Delta_x = \Delta_y = 6.25 \times 10^{-5}$ with a time step $\Delta_t = 6.25 \times 10^{-7}$; the latter on domain $\Omega = \{x : 0 < x < 1\}$ discretized by a uniform mesh of size $\Delta_X = 1.25 \times 10^{-3}$ with a time step $\Delta_T = 1.25 \times 10^{-5}$ (Figure 2.2). This choice of discretization parameters ensures that any disagreement between the pore- and Darcy-scale simulations is solely due to limitations of the Darcy-scale model rather than numerical errors (see the Appendix for detail).

Next, we consider two transport regimes, hereafter referred to as Case 1 and Case 2, which are characterized by different combinations of Pe and Da or, equivalently, $\alpha = -\log_\varepsilon \mathrm{Pe}$ and $\beta = \log_\varepsilon \mathrm{Da}$ with $\varepsilon = 0.0625$. Case 1 corresponds to $\mathrm{Pe} = \mathrm{Da} = 0.0625$ which translates into $\alpha = -1$ and $\beta = 1$; this regime satisfies constraints (2.13) (see Figure 4.3). Case 2 is characterized by $\mathrm{Pe} = 2.0$ and $\mathrm{Da} = 64.0$, so that $\alpha = 0.25$ and $\beta = -1.5$; this regime lies outside the homogenizability domain (see Figure 4.3).

2.4.1 Impact of Breakdown of the Darcy-Scale Model

For both Cases 1 and 2 we compare the averaged pore-scale concentrations of reactant A and reaction product C with the corresponding Darcy-scale concentrations. The former, $\bar{c}_A(x,t)$ and $\bar{c}_C(x,t)$, are computed with (2.16) and (2.23); and the latter, $C_A(x,t)$ and $C_C(x,t)$, with (2.20). Also compared is the total mass of the reaction product in the fracture, computed with the pore-scale (m_C) and Darcy-scale (M_C) models as

$$m_C(t) = \int_0^1 \bar{c}_C(x,t)\mathrm{d}x \quad \text{and} \quad M_C(t) = \int_0^1 C_C(x,t)\mathrm{d}x. \tag{2.31}$$

Figure 2.3 exhibits these three quantities for Case 1. Since this regime falls within the homogenizability region (Figure 4.3), one should expect a good agreement between the pore- and Darcy-scale simulations. This is indeed the case. A slight disagreement between the two models' predictions, which can be quantified in terms of a model error $\mathcal{E}_i = \|\bar{c}_i - C_i\|_2$ ($i = A,B,C$), being approximately of order $O(\varepsilon^2)$, as predicted by the homogenization theory [15].

Case 2, which violates the homogenizability conditions, gives rise to a pronounced disagreement between predictions of the pore- and Darcy-scale models (Figure 2.4). It exemplifies a transport regime in which the advection and diffusion time-scales are significantly faster than the reaction time-scale. In this regime the model errors $\mathcal{E}_i > \varepsilon$ for all three quantities. By way of example, the relative model error in predictions of the concentration of solute A, introduced by the use of the Darcy-scale simulations, $\varepsilon_A = 100\% \times \|\bar{c}_A - C_A\|_2 / \|\bar{c}_A\|_2$, grows with time, reaching $\approx 12\%$ by $t = 5$ (Table 3.3). This apparent failure of the Darcy-scale model is not only quantitative but also qualitative. While the Darcy-scale model predicts a Gaussian behavior, the averaged pore-scale dynamics is non-Gaussian, as evidenced by the asymmetric, long-tailed concentration profiles.

Figure 2.4 shows the longitudinal concentrations for the species A and C as well as the mass M_{C_M} and mass M_{C_m} for macro- and micro-scale concentrations $\bar{c}_{C_M}$ and $\bar{c}_{C_m}$, respectively.

Figure 2.4 confirms that the total mass production M_{C_M} and M_{C_m} is not conserved. This is also verified by the theoretical prediction using the specific parameters in Case 2 that violate the homogenizability region. Note that, in our model, microscopic simulation are treated as exact due to numerical testing (Appendix A).

Its α and β parameters correspond to the faster advection and diffusion at the microscale. The faster advection and diffusion makes the constraints (2.13) to be violated and this system is outside of the the homogenizability regime. Faster diffusion rates makes values of Da being larger, while faster advection corresponds to the higher Pe number which forces the failure of macroscopic descriptions based on local ARDEs leading to an absolute error $E > \varepsilon$ along the fracture Ω.

2.4.2 Relative Performance of the Hybrid Model

While the transport regime in Case 2 invalidates the reliance of the Darcy-scale model, the use of the pore-scale simulations over the whole transport domain Ω is computationally expensive even for a single fracture (Table 3.1) and prohibitively so for more complex pore geometries. Instead, we employ the hybrid algorithm described in section 2.3.2. We start by setting the width of the pore-scale simulation domain to $|\mathcal{N}_\delta| \equiv \Delta = b(t) - a(t) = 0.2$; the Darcy-scale model is solved in the remaining 80% of the simulation domain, $(0,a) \cup (b,1)$. Visual inspection of Figure 2.5 demonstrates a close agreement between the exact (pore-scale) solution for the averaged pore-scale concentration $\bar{c}_A(x,t)$ and the hybrid solution $C_A^{\mathrm{h}}(x,t)$. Table 3.3 further corroborates this observation by collating values of the relative model error

$$\varepsilon_A^{\mathrm{h}} = 100\% \times \|\bar{c}_A - C_A^{\mathrm{h}}\|_2 / \|\bar{c}_A\|_2$$

of the hybrid model at different times t. This degree of the hybrid's accuracy is achieved at the fraction of computational cost, yielding a significant reduction relative to that of the pore-scale

simulations: 1053 s for the hybrid model (Table 3.2) versus 5975 s for the pore-scale simulations (Table 3.1). (All computations were carried out on a singe-processor laptop.)

The hybrid's accuracy (and computational cost) can be increased by enlarging the region of the computational domain, $\mathcal{N}_\delta(t)$, wherein the pore-scale simulations are performed. Alternatively, the hybrid's computational cost can be reduced by decreasing the size of $\mathcal{N}_\delta(t)$, at the cost of reducing the hybrid's accuracy (Table 3.2). Even the smallest size of $\mathcal{N}_\delta$ reported in Table 3.2, $|\mathcal{N}_\delta(t)| = \Delta = 0.05$, yields an acceptable relative model error ($\varepsilon_A^{\mathrm{h}} = 0.43\%$). The increase in the hybrid's accuracy and computational cost with Δ is to be expected, since the accurate and expensive pore-scale simulations are carried out over the progressively larger domain $\mathcal{N}_\delta$. Refining the mesh size and time step of the Darcy-scale component of the hybrid is relatively inexpensive but does not yield a significant improvement in the relative model error (Table 2.4 in the Appendix).

2.5 Verification of Numerical Simulations

To ensure that our numerical solutions of the pore-scale (2.16) and Darcy-scale (2.20) models are not significantly affected by their space-time discetization, we progressively refine the mesh size and time step. Starting with $\Delta_x = \Delta_y = 10^{-3}$ and $\Delta_t = 10^{-5}$, the space-time discretization of (2.16) is refined according to $\Delta_x/2^k = \Delta_y/2^k$ and $\Delta_t/2^k$ with $k = 0, 1, \cdots$. Likewise, starting with $\Delta_X = 10^{-2}$ and $\Delta_T = 10^{-4}$, the space-time discretization of (2.20) is refined according to $\Delta_X/2^k$ and $\Delta_T/2^k$ with $k = 0, 1, \cdots$. Results of this mesh refinement are reported in Figure 2.6 for the averaged pore-scale concentration $\bar{c}_A(x, \cdot)$ computed with (2.16) and (2.23) and for the Darcy-scale concentration $C_A(x, \cdot)$ computed with (2.20). The refinement beyond $k = 2$ shows no visual improvement. (Although not shown here, the concentrations of species B and C exhibit an identical behavior.)

This assessment is made more quantitative by defining a relative discretization error

$$\mathcal{E}_k(f) = \frac{\|f_k - f_{k+1})\|_2}{\|f_{k+1}\|_2}, \qquad k = 0, 1, 2, \cdots$$

where $f_k = \bar{c}_A(\Delta_x/2^k = \Delta_y/2^k, \Delta_t/2^k)$ or $f_k = C_A(\Delta_X/2^k, \Delta_T/2^k)$. Table 3.1 demonstrates that the discretization error of 10^{-4} is achieved with the refinement levels of $k = 4$ for the pore-scale simulations and $k = 3$ for the Darcy-scale simulations. Further refinement does not substantially improve the discretization error, but considerably increases the simulation time. These values of the discretization parameters are used in all the simulations reported in this study.

Finally, we explore benefits of refining the space-time discretization of the Darcy-scale component of the hybrid, $\{\Delta_X/2^k, \Delta_T/2^k\}$, while keeping the discretization of the pore-scale component fixed at $\{\Delta_x/2^4, \Delta_y/2^4, \Delta_t/2^4\}$. Such refinement does not improve the hybrid's accuracy, quantified in terms of the relative model error $\varepsilon_A^{\mathrm{h}} = 100\% \times \|\bar{c}_A - C_A^{\mathrm{h}}\|_2/\|\bar{c}_A\|_2$ for the hybrid model (Table 2.4). Hence, going above the refinement level $k = 3$ for the Darcy-scale component of the hybrid only increases the computational time.

2.6 Summary and Conclusions

We developed a hybrid model of propagation of reactive fronts. These fronts involve an irreversible homogeneous reaction $A + B \to C$ and are highly localized due to an initial distribution of reactants A and B. A set of numerical experiments for multicomponent reactive flow in a horizontal open fracture is performed to demonstrate that dynamic reactive fronts might not be amenable to Darcy-scale modeling. Our hybrid algorithm couples the pore-scale model in the vicinity of a moving reaction front with the Darcy-scale model elsewhere in the fracture.

Our study leads to the following major conclusions.

- Necessary conditions for the breakdown of Darcy-scale models of dynamic reactive fronts

are presented as a phase-diagram in the space of the Péclet (Pe) and Damköhler (Da) numbers. Our simulations provide an example of the failure of a Darcy-scale model whose parameters fall outside the homogenizability region in this diagram.

- The observed failure of the Darcy-scale model of reaction fronts in an open fracture is not only quantitative but also qualitative. While the Darcy-scale model predicts a Gaussian behavior, the true dynamics is non-Gaussian, as evidenced by the asymmetric, long-tailed concentration profiles.

- The representational accuracy of our hybrid algorithm is comparable to that of high-fidelity pore-scale simulations, but at the fraction of computational cost.

- The hybrid formulation does not require any additional parameters beyond those used in macroscopic or microscopic models.

- The hybrid formulation for the moving dynamic fronts suggests its high adaptability to a wide variety of problems and different numerical schemes.

In follow-up studies, we will employ our hybrid algorithm to model dynamic reaction fronts, which propagate in porous media and involve two-phase incompressible flow.

Table 2.1: Relative model errors, $\varepsilon_A = 100\% \times \|\bar{c}_A - C_A\|_2 / \|\bar{c}_A\|_2$ and $\varepsilon_A^{\mathrm{h}} = 100\% \times \|\bar{c}_A - C_A^{\mathrm{h}}\|_2 / \|\bar{c}_A\|_2$, introduced by the use of the Darcy-scale and hybrid simulations, respectively. The pore-scale result, $\bar{c}_A$, is treated as "ground-truth".

Model error	$t = 1$	$t = 2$	$t = 5$
Darcy-scale, ε_A	4.52	7.82	11.63
Hybrid, $\varepsilon_A^{\mathrm{h}}$	0.05	0.11	0.15

Table 2.2: Simulation time (in seconds) and relative model error of the hybrid simulations, $\varepsilon_A^{\mathrm{h}} = 100\% \times \|\bar{c}_A - C_A^{\mathrm{h}}\|_2 / \|\bar{c}_A\|_2$, at $t = 5$ and for several sizes $|\mathcal{N}_\delta| = \Delta$ of the pore-scale simulation domain $\mathcal{N}_\delta$.

Δ	0.05	0.10	0.15	0.20	0.30	0.40
$\varepsilon_A^{\mathrm{h}}$	0.4301	0.3051	0.2196	0.1573	0.0482	0.00053
Sim. time, [s]	391.62	650.71	891.74	1053.28	1768.05	2564.89

Table 2.3: Relative discretization errors, $\mathcal{E}_k$, and simulation times, in seconds, for the averaged pore-scale ($\bar{c}_A$) and Darcy-scale (C_A) estimates of the concentration of species A at time $t = 1$ on the meshes and time steps refined by the factor of 2^k.

Refinement level, k	Relative Error, $\mathcal{E}_k(f) \times 10^{-3}$		Simulation time, [s]	
	$f = \bar{c}_A$	$f = C_A$	$\bar{c}_A$	C_A
0	5.458	8.20763	57.19	2.24
1	2.542	1.31274	162.92	7.53
2	0.503	0.54580	546.83	20.69
3	0.285	0.05137	1760.09	69.48
4	0.09215	0.05011	5975.24	247.98
5	0.08973	–	15627.45	–

Table 2.4: Relative model error of the hybrid simulations, $\varepsilon_A^{\mathrm{h}}$, at $t = 1$ and for several levels of refinement, k, of the Darcy-scale component. The discretization of the pore-scale component is fixed at $\Delta_x/2^4, \Delta_y/2^4, \Delta_t/2^4$.

Refinement level, k	3	4	5
$\varepsilon_A^{\mathrm{h}}$, [%]	0.0529	0.0517	0.0503

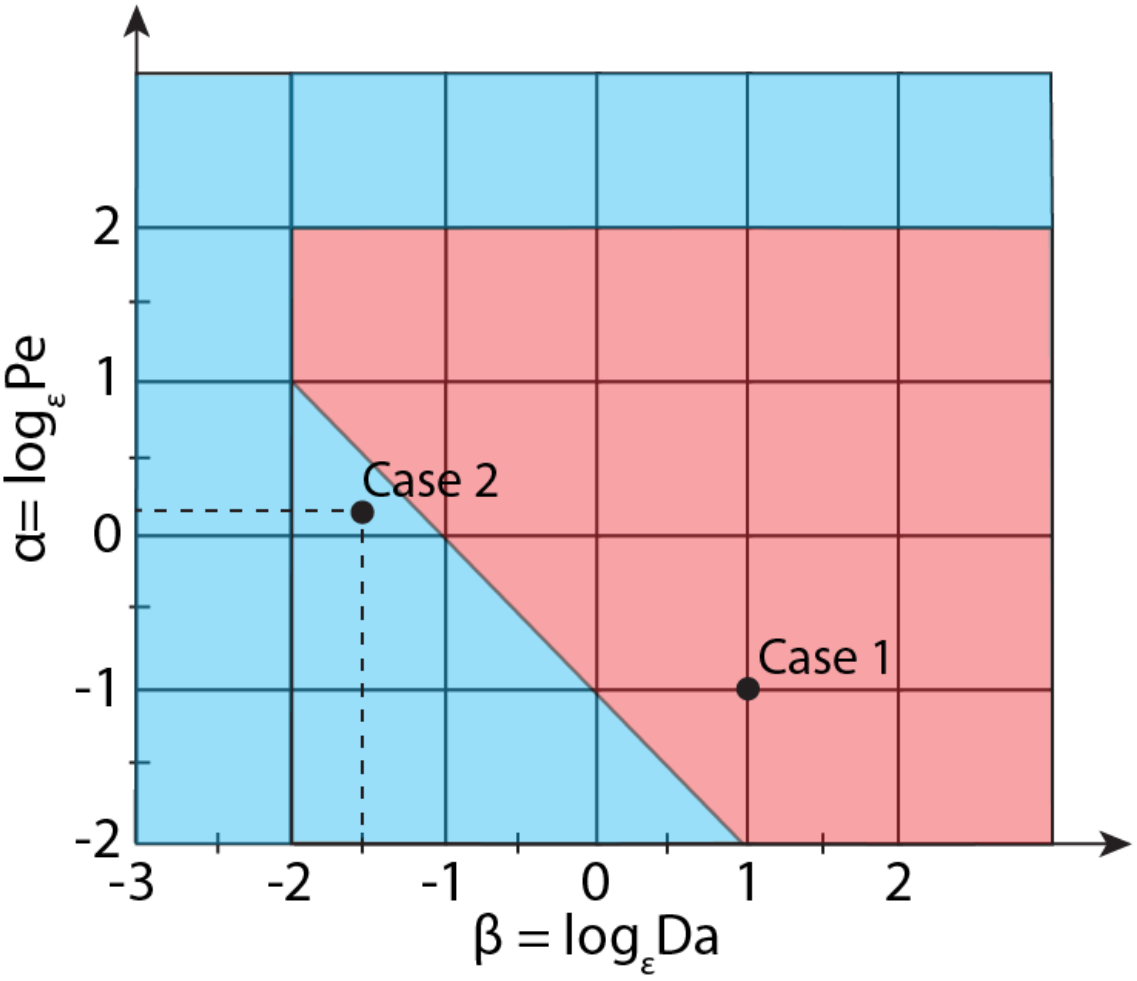

Figure 2.1: Region of the validity of the Darcy-scale transport model (2.12) in the Pe-Da phase space spanned by the Péclet (Pe) and Damköhler (Da) numbers. Case 1, $(\alpha, \beta) = (-1, 1)$, satisfies and Case 2, $(\alpha, \beta) = (1/4, -3/2)$, violates the homogenizability conditions (2.13).

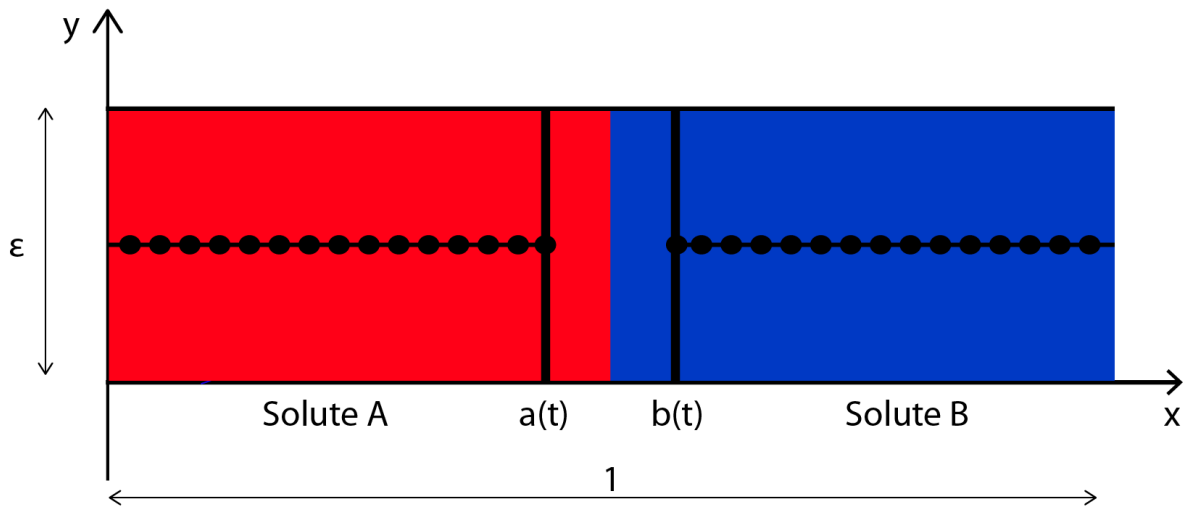

Figure 2.2: A dynamic diffused reaction front, centered at $x_{\mathrm{f}}(t)$, propagating in an open fracture of dimensionless unit length and dimensionless width 2ε. Our hybrid algorithm solves the (two-dimensional) pore-scale model in the front's neighborhood $\mathcal{N}_\delta = \{\mathbf{x} : x_{\mathrm{f}}(t) - a(t) < x < x_{\mathrm{f}}(t) + b(t),\ -\varepsilon < y < \varepsilon\}$ and the (one-dimensional) Darcy-scale model in the rest of the fracture. The two models are coupled by enforcing the continuity conditions at $a(t)$ and $b(t)$.

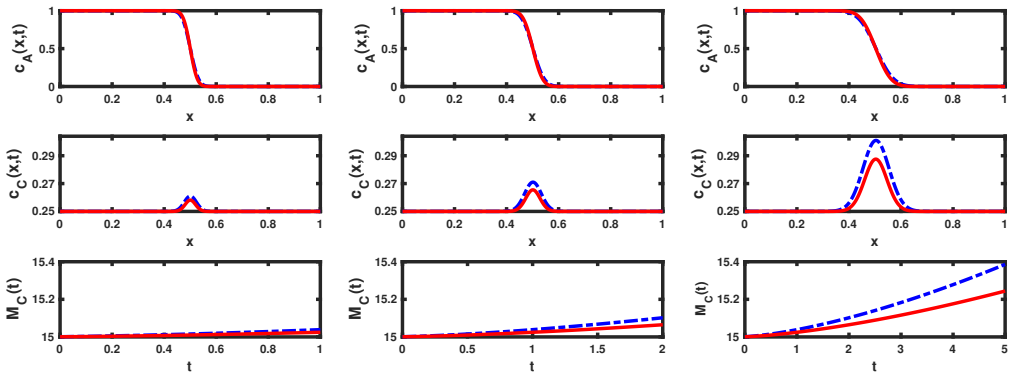

Figure 2.3: First two rows: Temporal snapshots, at $t = 1.0, 2.0$ and 5.0 (from left to right), of the averaged pore-scale concentrations $\bar{c}_A(x,t)$ and $\bar{c}_C(x,t)$ (solid line) and their Darcy-scale counterparts $C_A(x,t)$ and $C_C(x,t)$ (dashed line), for Case 1 which satisfies the homogenizability conditions. Bottom row: the corresponding total mass of the reaction product in the fracture, computed with the pore-scale (m_C) and Darcy-scale (M_C) models.

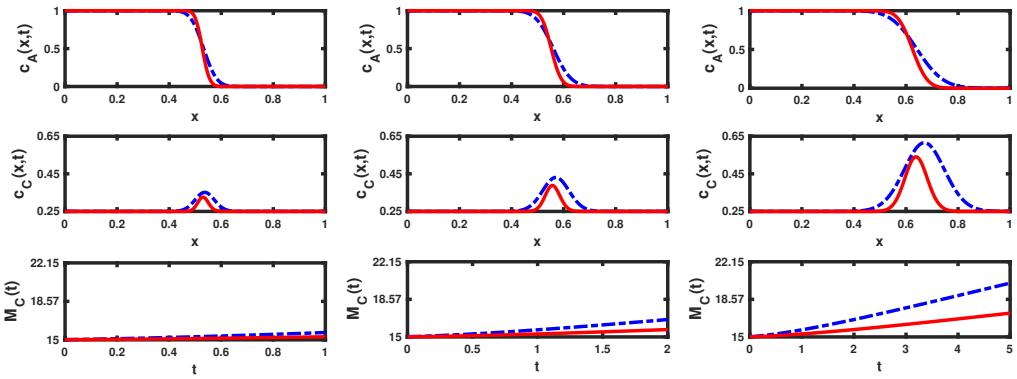

Figure 2.4: First two rows: Temporal snapshots, at $t = 1.0, 2.0$ and 5.0 (from left to right), of the averaged pore-scale concentrations $\bar{c}_A(x,t)$ and $\bar{c}_C(x,t)$ (solid line) and their Darcy-scale counterparts $C_A(x,t)$ and $C_C(x,t)$ (dashed line), for Case 2 which violates the homogenizability conditions. Bottom row: the corresponding total mass of the reaction product in the fracture, computed with the pore-scale (m_C) and Darcy-scale (M_C) models.

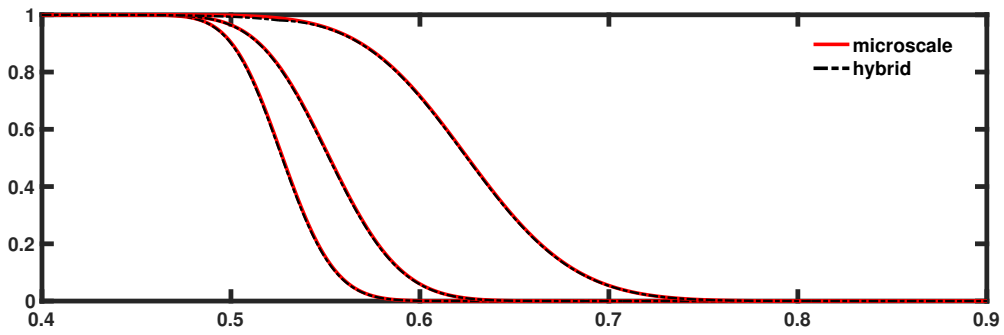

Figure 2.5: Temporal snapshots, at $t = 1.0, 2.0$ and 5.0 (from left to right), of the averaged pore-scale concentration $\bar{c}_A(x,t)$ and its counterpart $C_A^{\mathrm{h}}(x,t)$ computed with the hybrid simulations for Case 2.

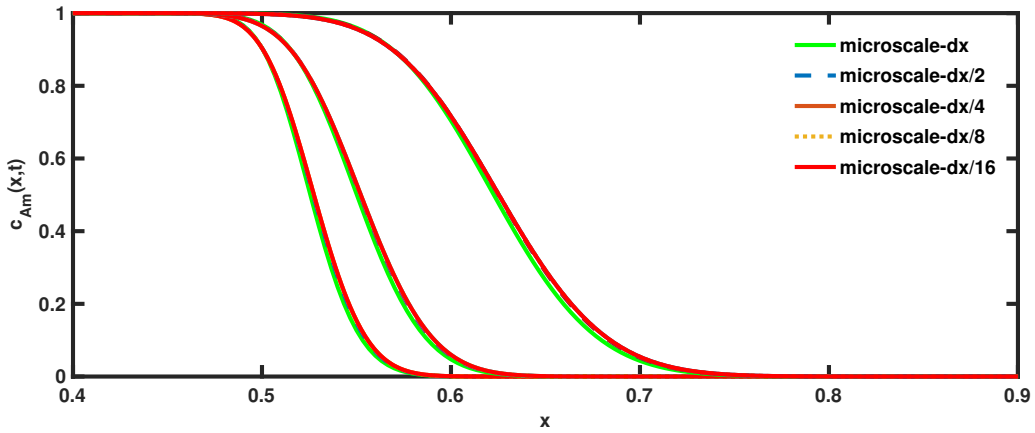

Figure 2.6: Spatial profiles of (top) averaged pore-scale concentration $\bar{c}_A(x,t)$ and (bottom) Darcy-scale concentration $C_A(x,t)$ at times $t = 1, 2$ and 5 (from left to right) for the transport regime characterized by $\alpha = 1/4$ and $\beta = -3/2$. The former is computed with (2.16) and (2.23), the latter with (2.20). Both use the progressively finer time-space discretizations.

Natalia Siuliukina, Daniel M. Tartakovsky, ”A Hybrid Multiscale Model of Miscible Reactive Fronts”, *Water Resources Research*, 54, 2018.

Chapter 3

Viscous fingering in non-isothermal filtration

3.1 Introduction

Flow displacements in porous media have been the subject of numerous studies due to their importance in many processes such as enhanced oil recovery, solute transport in aquifers, filtration and carbon dioxide sequestration ([27], [63], [39]).

In oil recovery processes it is very common to inject water or polymers into the oil field at certain points in an attempt to drive oil to various distant locations for pumping purposes. In large reservoirs the oil displacement by water assumes the form of a dynamic front which is a moving zone across which the saturation of water (the fraction of pore space occupied by water) changes fast compared to regions of constant saturation before and after the front respectively. In this process we can observe the problem of fingering instabilities. The water pushes the oil forward and penetrates the oil through formed channels that called fingers ([21], [20]). The mechanism that starts the fingering process is similar to the problem of the displacement of a viscous fluid by a less viscous one in Hele-Shaw cell, a pair of parallel glass plates that is separated by a

small gap ([70]). Here the instability is caused by the high mobility properties of the displacing fluid(water in our case). Linear stability analysis is a common technique based on triggering of small perturbations of state variables and identify whether these perturbations grow or decay over time([46], [98], [67]). We analyze numerically the instability of a front separating two fluids in a porous medium. The front is unstable for the large values of viscosity ratio. There could be two types of perturbations: the one that spatially smooth and the perturbations with large amplitude. In non-isothermal displacement problem the viscosity of fluids may vary with the temperature of the fluids. Due to the difference in the rates of heat and mass transport, the incusion of the heat transfer equation for the immiscible fluid flow involves two fronts, the first being the saturation front and the second the thermal front ([47], [46]). The fingering in each of the fronts contribute to the instability of the front and the rate of growth of fingers depends on both saturation and thermal hear transfer effects ([64], [28]). The special cases of viscous fingering with temperature dependence in which the displacing and the displaced fluids have similar compositions but different temperatures can be observed in phenomena such as magma flow through dikes, geothermal flows and the flow of the injected melt in injection molding process ([40], [35]). A very limited number of studies exists on immiscible thermo-viscous fingering, with most previous research focusing on miscible cases ([51], [53], [10]).

A major goal of our analysis is to develop a stability conditions for non-isothermal filtration problem which involves the investigation of the stability of displacement front with small perturbations with the temperature dependent viscosity. A set of numerical experiments is performed to investigate the validity of stabilizing conditions for the immiscible two phase fluid flow in a horizontal open fracture. When these conditions are not met, the flow becomes unstable and we can observe the development of fingers instabilities. One the other side, the validity of the stable conditions allows us to control viscous fingering and enhance the oil recovery.

Section 2 contains the problem formulation and the description of the flow of two immiscible fluids in porous medium in non-isothermal filtration. Section 3 summarizes the linear

stability conditions for isothermal and non-isothermal fluid flow in porous media. It also summarizes, in the form a phase diagram in the space of the dimensionless characteristic viscosity constants A and B, the conditions under which the linear stability of the flow becomes invalid in isothermal and non-isothermal cases. In section 4 we report the numerical model we used for solving the non-isothermal filtration problem. In section 5 we report results of our numerical experiments via various stability regimes, including validity isothermal and non-isothermal models. Main conclusions drawn from our study are present in section 6.

3.2 Problem Formulation

We consider a two-dimensional immiscible flow in a horizontal homogeneous generic medium with constant porosity m and constant absolute permeability K. A fluid with viscosity μ_1, saturation s_1 is driven forward by the pressure gradient to displace the second one of viscosity μ_2 and saturation s_2. The direction of the flow is along the $x-$axis an the $y-$axis is parallel to the initial plane of the interface (Figure 3.1).

The incompressible flow of two immiscible fluids in porous medium can be described by the following Darcy, continuity and heat equations:

$$\hat{u}_i = -\frac{K}{\mu_i} k_i(s_i) \bigtriangledown \hat{p}, \tag{3.1}$$

$$m\frac{\partial s_i}{\partial \hat{t}} + \nabla \cdot \hat{u}_i = 0, \qquad i = 1,2. \tag{3.2}$$

$$\frac{\partial}{\partial \hat{t}}(ms_1\rho C_1\hat{T} + ms_2\rho C_2\hat{T} + (1-m)\rho_r C_r\hat{T}) + \nabla\cdot(C_1\hat{u}_1\hat{T} + C_2\hat{u}_2\hat{T}) = \nabla\cdot(\hat{\lambda}\nabla\hat{T}). \tag{3.3}$$

Subject to the following boundary and initial conditions

- $\frac{\partial \hat{p}}{\partial n}|_{y=0} = \frac{\partial \hat{p}}{\partial n}|_{y=y_{max}} = 0, \quad \hat{p}|_{x=0} = p_{in}, \quad \hat{p}|_{x=x_{max}} = p_{fin},$

- $s|_{x=0} = s_{in}, \quad s|_{t=0} = \begin{cases} s_{in}, x \leq x_0 + 0.2sin^2(3\pi y), \\ s_{fin}, x \geq x_0 + 0.2sin^2(3\pi y) \end{cases}$
- $\frac{\partial \hat{T}}{\partial n}|_{y=0} = \frac{\partial \hat{T}}{\partial n}|_{y=y_{max}} = 0, \quad \hat{T}|_{x=0} = T_{in}, \quad \hat{T}|_{x=x_{max}} = T_{fin},$

where subscripts $i = 1,2$ are appended to the symbols which represent the displacing (water) and displaced (oil) fluids, respectively, $k_i(s_i)$ are the relative permeabilities, u_i - Darcy's velocity, p is the pressure, T is the temperature, C_i are the specific heats of the water, oil and rock, respectively. The values for initial conditions are presented in Table (3.1).

Considering large-scale motions, we ignore the gravity and capillary discontinuity of the pressure and assume that specific heats are constants. Assuming that the void space is completely filled by the two phases so that $s_1 + s_2 = 1$, the saturation of the water can be represented in terms of the saturation of the oil: $s_1 = 1 - s_2$. The indices are dropped from the previous notation in favor of s and $1 - s$ representing the saturations of the water and oil phases, respectively. At some arbitrary time $t = 0$, we begin to displace the oil by water. The Figure 3.1 shows the initial distribution of the water with concentration s_1 and viscosity μ_1 on the left and the oil with the concentration s_2 and viscosity μ_2 on the right. For the isothermal flow μ_2 is a constant and for the simplicity we will use the form $\mu_2 = e^A$, where $A = const$. In case of the non-isothermal flow, the temperature dependence of the viscosity μ_2 is well described by the Arhenius law, $\mu_2 = \mu^* e^{B/T}$, where μ^*, and B is a constant activation energy ([76], [25], [61]). For the simplicity, we use the following form for the temperature-dependent viscosity: $\mu_2 = e^{A+B/T}$, where $A, B = const$. Our objective is to carry out a linear stability analysis of this problem in isothermal and non-isothermal flow in order to determine parameter limits within which instabilities can be triggered by perturbations of the system.

3.2.1 Governing equations

Let L and U denote characteristic length and characteristic velocity magnitude, respectively. We introduce dimensionless parameters and independent variables:

$$\hat{\mathbf{x}} = \frac{\hat{\mathbf{x}}}{L}, \quad \hat{\mathbf{u}}_\mathbf{i} = \frac{\mathbf{u}}{U}, \quad \hat{t} = t\frac{U}{L}, \quad \hat{p_i} = p_i\frac{K}{\mu_1 UL},, \quad \hat{T} = \frac{T - T_{in}}{T_{fin} - T_{in}} \tag{3.4}$$

$$b = \frac{C_2 + \frac{1-m}{m}\frac{\rho_s}{\rho}C_s}{C_1 - C_2}, \quad h = \frac{C_2}{C_1 - C_2}, \quad \lambda = \frac{\hat{\lambda}}{m\rho(C_1 - C_2)}. \tag{3.5}$$

Let ω to be the total flow rate

$$\omega \equiv u_1 + u_2 = -\phi(s)\bigtriangledown p = -(\phi_1(s) + \phi_2(s))\bigtriangledown p. \tag{3.6}$$

We'll define fractional flow function $F(s)$ as the fraction of the displacing fluid in the total flow with the mobility ratio μ_0:

$$F(s) = \frac{k_1(s)}{k_1(s) + \mu_0 k_2(1-s)}, \quad F(s)\omega = u_1, \quad (1 - F(s))\omega = u_2, \quad \mu_0 = \frac{\mu_1}{\mu_2} \tag{3.7}$$

Rewriting (3.3) in terms on the dimensionless quantities (3.5) yields a dimensionless form of the governing equations.

$$m\frac{\partial s}{\partial t} + \nabla \cdot (F(s)\omega) = 0, \tag{3.8}$$

$$\nabla \cdot \omega = 0, \tag{3.9}$$

$$\frac{\partial}{\partial t}(sT + bT) + \frac{1}{m}\nabla \cdot (F(s)T + hT)\omega = \nabla \cdot (\lambda \nabla T), \tag{3.10}$$

subject to the correspondingly rescaled initial and boundary conditions. The following relative

permeabilities $k_i(s_i)$ are used in the quadratic form:

$$k_i(s_i) = \begin{cases} (\frac{s_i - s_0}{1 - s_0})^{\gamma}, & s \geq s_0 \\ 0, & s \leq s_0 \end{cases}, \qquad \gamma = 2. \tag{3.11}$$

with the residual saturation s_0.

3.3 Stability analysis of isothermal case.

We consider water/oil moving steadily along Ox axis with constant speed of filtration $\omega = 1$. Without loss of generality, $m = 1$ since it can be absorbed into the time variable. To investigate the stability of the front governing small disturbances, we rewrite the one dimensional version of isothermal part of (3.8) in terms of moving wave coordinate $\xi = x - V_s t$, y and t so that

$$\frac{\partial s}{\partial t} - V_s \frac{\partial s}{\partial \xi} + \nabla \cdot (\phi_1(s) \bigtriangledown p) = 0, \tag{3.12}$$

$$\nabla \cdot (\phi(s) \bigtriangledown p) = 0 \tag{3.13}$$

where the velocity of the shock region could be determined from the steady state analytical solution of (3.12)

$$V_s = \frac{F(s_+) - F(s_-)}{s_+ - s_-}, \tag{3.14}$$

here s_-, s_+ - values of the saturation behind (water) and ahead (oil) of the front respectively. These simplified equations (3.12) have solutions with sharp interfaces, i.e. jump discontinuities in the saturation s and the pressure gradient $\bigtriangledown p$. The saturation and pressure variables are

expressed in terms of the base state and perturbation components:

$$s(\xi,y,t) = s_0(\xi) + \hat{S}(\xi)e^{iny+\sigma t}, \tag{3.15}$$

$$p(\xi,y,t) = p_0(\xi) + \hat{P}(\xi)e^{iny+\sigma t}, \tag{3.16}$$

where n is the wavenumber of perturbation and σ is a growth rate and

$$\hat{S}, \frac{\partial \hat{S}}{\partial \xi}, \hat{P}, \frac{\partial \hat{P}}{\partial \xi} \to 0, \xi \to \pm\infty. \tag{3.17}$$

The base state steady solution (3.12) is subject to normalized boundary conditions of the Backley-Leverett problem $s = s(\xi)$, $s(-\infty) = s_-$, $s(+\infty) = s_+ = s_0$, It provides the basic saturation profile and the base state satisfies

$$\frac{ds_0}{d\xi} = \delta(\xi), \tag{3.18}$$

$$\frac{dp_0}{d\xi} = -\frac{1}{\phi(s_0)} \tag{3.19}$$

From (3.18) using interface and boundary conditions, $\hat{S} = C\delta(\xi)$ for some constant C. Substituting the expansion (3.15) into equations (3.12) and solving the resulting eigenvalue problem we get the system of equations for the linear stability problem:

$$\frac{\partial}{\partial \xi}(\phi(s_0) + \phi'(s_0)\hat{S}\frac{\partial p_0}{\partial \xi}) - n^2\hat{P}\phi(s_0) = 0, \tag{3.20}$$

$$\frac{\partial}{\partial \xi}(\phi_1(s_0)\frac{\partial \hat{P}}{\partial \xi} + \phi_1'(s_0)\hat{S}\frac{\partial p_0}{\partial \xi}) - V_s\frac{\partial \hat{S}}{\partial \xi} - n^2\hat{P}\phi_1(s_0) = -\sigma\hat{S} \tag{3.21}$$

This system can be solved numerically or by matched asymptotic expansions([98], [66]). One could enforce continuity of pressure and volume flux across the sharp interface at $\xi = 0$ [98]

$$\Delta(\hat{P}) = -C\Delta(\frac{dp_0}{d\xi}), \tag{3.22}$$

$$\Delta(\phi(s_0)\frac{d\hat{P}}{d\xi}) = 0, \tag{3.23}$$

$$\Delta(\phi_1(s_0)\frac{d\hat{P}}{d\xi}) = (s^- - s^+)\sigma C \tag{3.24}$$

Away from the discontinuity $\xi = 0$ we can solve (3.20) and (3.18)

$$\hat{P^-} = Ae^{-n\xi}, \quad \xi < 0, \tag{3.25}$$

$$\hat{P^+} = Be^{n\xi}, \quad \xi > 0, \tag{3.26}$$

$$\hat{S} = C\delta(\xi) \tag{3.27}$$

Using the jump conditions (3.22) for the linear stability equations (3.20) and eliminating constants A, B, C gives us the condition on the eigenvalue σ

$$\frac{\sigma}{n} = \frac{\phi(s_-) - \phi(s_+)}{\phi(s_-) + \phi(s_+)} \tag{3.28}$$

Or in case of the flow having a velocity ω_0, then

$$\frac{\sigma}{n} = \omega_0 \frac{\phi(s_-) - \phi(s_+)}{\phi(s_-) + \phi(s_+)}. \tag{3.29}$$

This relation dictates the growth or decay of perturbations to the leading order in the wave number. In particular, it controls whether the sharp interface is stable or unstable:when the total mobility upstream, $\phi(s_-)$, is larger than that downstream,$\phi(s_+)$, then for long waves, the growth rate is positive and the interface between the phases is affected by the Saffman-Taylor fingering

instability. We are only interested in $\sigma > 0$ leading to unstable solutions hence we simply need to investigate the mobility ratio M^* across the shock

$$M^* = \frac{\phi(s_+)}{\phi(s_-)} > 1. \tag{3.30}$$

Using Rankine-Hugoniot condition:

$$F^{'}(s_-) = \frac{F(s_-) - F(s_+)}{s_- - s_+}. \tag{3.31}$$

and applying the definition of the fractional flow function (3.7) to the left and to the right side of (3.31)) and also that $s_+ = s_0$ we'll get

$$s_- = s_0 + \frac{1 - 2s_0}{\sqrt{1/\mu_0 + 1}}, \tag{3.32}$$

From (3.30) - (3.32) if $M^* < 1$ then the system is not stable and if $M^* > 1$ the system is stable, which gives us if $\mu_0 = \mu_1/\mu_2 < 1/3$ the system is stable and if $\mu_0 > 1/3$ the system is unstable. Since the scaled water viscosity $\mu_1 \equiv 1$ and we pick μ_2 such as $\mu_2 = e^A, A = const$, then we can introduce the stability regime for isothermal flow on Figure (3.2).
If the relative permeabilities $k_i(s_i)$ in equation (3.11) are used in the cubic form $\gamma = 3$ then the system is stable if the mobility ratio $\mu_0 < 1/10$ and if $\gamma = 4$, then $\mu_0 < 1/19$.

3.3.1 Stability analysis of non-isothermal case.

We again restrict ourselves to the one-dimensional problem of frontal displacement, assuming that the motion takes place along the x axis and that the total flow rate ω does not depend on time. Considering large scale motions, we ignore the capillary discontinuity of the pressure and heat conduction λ in the system of equations (3.8) ([10]).

To make the stability analysis more simple in non-isothermal case, we rewrite the one

dimensional thermal balance as

$$\frac{\partial T}{\partial t} + \nabla \cdot (\hat{C_1} u_1 + \hat{C_2} u_2) T = 0, \tag{3.33}$$

where the average specific heat numbers $\hat{C_i}$ represented as the average ratio of energy transport to total heat energy,

$$\hat{C_i} = \frac{C_i}{\int_0^1 (msC_1 + m(1-s)C_2 + (1-m)\rho_r C_r) ds}, \quad i = 1,2. \tag{3.34}$$

We do rescaling based on $\hat{C_i}$ so we can observe the average effect each process has on the heat equation (3.8). The average convection numbers $\hat{C_i}$ are of the same order and close to one (within the order one factor). With this in mind, we will take for simplicity $\hat{C_i} = 1$. Then for one dimensional frontal displacement the mass conservation equation $\nabla \cdot \omega = 0$ and $\omega = 1$. Then we are able to simplify the temperature dependence as $\frac{\partial T}{\partial t} + \frac{\partial T}{\partial x} = 0$. We can now perform a linear stability analysis around the shock associated with the change of temperature, with the traveling wave expansion $\xi = x - V_T t$, where $V_T = 1$. We consider the temperature change around the shock and we must perturb variable T in addition to the variables s and p. We have a sharp front for the saturation variable and for the temperature as well and they are both centered around $\xi = 0$. The system of one dimensional non-isothermal equations (3.8) for the two phase filtration problem in terms of the traveling wave coordinate ξ

$$\frac{\partial s}{\partial t} + \nabla \cdot (\phi_1(s) \bigtriangledown p - s\hat{x}) = 0, \tag{3.35}$$

$$\nabla \cdot (\phi(s) \bigtriangledown p) = 0, \tag{3.36}$$

$$\frac{\partial T}{\partial t} + \nabla \cdot (\phi(s) \bigtriangledown p - \hat{x}) T = 0. \tag{3.37}$$

The saturation, pressure and temperature variables are expressed in terms of base state and per-

turbation component:

$$s(\xi,y,t) = s_0(\xi) + \hat{S}(\xi)e^{iny+\sigma t}, \tag{3.38}$$

$$p_0(\xi,y,t) = p_0(\xi) + \hat{P}(\xi)e^{iny+\sigma t}, \tag{3.39}$$

$$T(\xi,y,t) = T_0(\xi) + \hat{T}(\xi)e^{iny+\sigma t} \tag{3.40}$$

with

$$\hat{S}, \frac{\partial \hat{S}}{\partial \xi}, \hat{P}, \frac{\partial \hat{P}}{\partial \xi}, \hat{T}, \frac{\partial \hat{T}}{\partial \xi} \to 0, \xi \to \pm\infty. \tag{3.41}$$

Applying the perturbation variables, the eigenvalue problem to linear order is

$$\frac{\partial}{\partial \xi}(\phi(s_0)\frac{\partial \hat{P}}{\partial \xi} + \phi'(s_0)\hat{S}\frac{\partial p_0}{\partial \xi} - \phi_2(s_0)\frac{\mu_2'(T_0)}{\mu_2^2(T_0)}\frac{\partial p_0}{\partial \xi}\hat{T}) - n^2\hat{P}\phi(s_0) = 0, \tag{3.42}$$

$$\frac{\partial}{\partial \xi}(\phi_1(s_0)\frac{\partial \hat{P}}{\partial \xi} + \phi_1'(s_0)\hat{S}\frac{\partial p_0}{\partial \xi}) + \frac{\partial \hat{S}}{\partial \xi} - n^2\hat{P}\phi_1(s_0) = -\sigma\hat{S}, \tag{3.43}$$

$$\frac{\partial}{\partial \xi}(\phi(s_0)\frac{\partial \hat{P}}{\partial \xi}T_0 + \phi(s_0)\frac{\partial p_0}{\partial \xi}\hat{T} + \phi'(s_0)\frac{\partial p_0}{\partial \xi}T_0 - \phi_2(s_0)\frac{\mu_2'(T_0)}{\mu_2^2(T_0)}\frac{\partial p_0}{\partial \xi}T_0) + \frac{\partial \hat{T}}{\partial \xi} - n^2\hat{P}\phi(s_0)T_0 = -\sigma\hat{T} \tag{3.44}$$

These equations are valid away from $\xi = 0$ where steady states are well defined. The steady state satisfies:

$$\frac{dT_0}{d\xi} = \delta(\xi), \tag{3.45}$$

$$\frac{dp_0}{d\xi} = -\frac{1}{\phi}, \tag{3.46}$$

$$\frac{ds_0}{d\xi} = \delta(\xi) \tag{3.47}$$

If we substitute (3.45) into (3.42) to get $\hat{T} \equiv 0, \xi \neq 0$ for non-zero eigenvalues. It removes

temperature dependence from the eigenvalue problem and we get standard solutions (3.25). To find a unique eigenvalue we use eigenfunction in the form $\hat{T} = C_T\delta(\xi)$. With analogue to (3.22) we introduce the following jump conditions to find solutions for the eigenvalue problem

$$\Delta(\hat{P}) = -(C_s + C_T)\Delta(\frac{dp_0}{d\xi}), \tag{3.48}$$

$$\Delta(\phi(s_0)\frac{d\hat{P}}{d\xi}) = 0, \tag{3.49}$$

$$\Delta(\phi_1(s_0)\frac{d\hat{P}}{d\xi}) = (s^- - s^+)C_s\sigma, \tag{3.50}$$

$$\Delta(\phi(s_0)\frac{d\hat{P}}{d\xi}T_0) = C_T\sigma. \tag{3.51}$$

Which we can solve to get the solutions

$$\frac{\sigma}{n} = 2\frac{\phi(s_-) - \phi(s_+)}{\phi(s_-) + \phi(s_+)} \tag{3.52}$$

If the speed of the temperature front is some general ω_0, then

$$\frac{\sigma}{n} = 2\omega_o\frac{\phi(s_-) - \phi(s_+)}{\phi(s_-) + \phi(s_+)}. \tag{3.53}$$

The problem has two shock fronts, one in the classical sense where the jump in saturation is due to the viscosity difference of the two immiscible fluids and the other associated in change in viscosity due to a change of temperature. Each front goes unstable in the classical shock sense and then collaborates to create larger fingering instability with twice the growth rate.

Since we are interested in instability conditions leading to $\sigma > 0$ we get the same formulation as (3.30) $M* = \frac{\phi(s_-)}{\phi(s_+)} > 1$, or $\mu_2/\mu_1 > 3$. We know that $\mu_2(T) = e^{A-B/T}$ and scaled viscosity of water $\mu_1 \equiv 1$, then we can introduce stability region for the non-isothermal flow and we can control the stability regime by choosing parameters A and B. It gives us the condition for stability inequality: if $e^{A-B/T} < 3$ then we can observe the stable regime and viscous fingers

will dissolve with time, otherwise the viscous fingering will continue to spread out. The scaled temperature T is from 0 to 1 and we can find the stability region for parameters A and B on Figure (3.3). If we pick two parameters from the stable region, we can control viscous fingering and make the flow stable after the extended period of time.

3.4 Numerical Model

The pressure, saturation and temperature equations have been discretized using a finite difference scheme. Uniform rectangular spatial and temporal grids with steps h and τ are employed. The values of the grid functions pressure $P^n_{i,j}$, saturation $s^n_{i,j}$ and temperature $T^n_{i,j}$ on the time layer n at the nodes of the spatial grid (i, j) are found by the method of splitting by physical processes. Spatial derivatives are discretized using the forward difference formula. The scheme is fully implicit in time. Computations are carried out in three stages on each time layer. In the first stage, we calculate the distribution of the pressure $P^n_{i,j}$ for constant values of the concentrations and temperature. To calculate the pressure distribution we employ the difference analogs of Eqs. (3.8) written in conservative manner according to five point template [72]:

$$\sum \omega^n_{i,j,i',j'} = 0, \tag{3.54}$$

$$\omega^n_{i,j,i',j'} = G^{n-1}_{i,j,i',j'}(P^n_{i,j} - P^n_{i',j'}), \tag{3.55}$$

$$G^n_{i,j,i',j'} = 2\frac{\phi(s^n_{i,j})\phi(s^n_{i',j'})}{\phi(s^n_{i,j}) + \phi(s^n_{i',j'})} \tag{3.56}$$

where $\omega^n_{i,j,i',j'}$ and $G^n_{i,j,i',j'}$ are the fluid flow and the mobility function between the nodes (i, j) and (i', j'). Summation in expression (3.54) is made over all the nodes adjacent to (i, j). Equation is solved for the pressure $P^n_{i',j'}$ by the iteration method using the saturation and temperature distribution determined on the previous time layer.

For the second and third stage the saturation $s^n_{i,j}$ and temperature $T^n_{i,j}$ are calculated based

on the finite volume method with upwind scheme for $s^n_{i,j}$:

$$s^n_{i,j} - s^{n-1}_{i',j'} = -(K^{n-1}_{i,j} - K^{n-1}_{i',j'}), \tag{3.57}$$

$$K^{n-1}_{i,j} = -F(s^n_{up})(P^n_{i,j} - P^n_{i',j'}), \tag{3.58}$$

$$s^n_{up} = \begin{cases} s^n_{i,j}, & P^n_{i,j} - P^n_{i',j'} < 0 \\ s^n_{i',j'}, & P^n_{i,j} - P^n_{i',j'} > 0 \end{cases} \tag{3.59}$$

$$s^n_{i,j}T^n_{i,j} - s^{n-1}_{i',j'}T^{n-1}_{i',j'} + b(T^n_{i,j} - T^{n-1}_{i',j'}) + (W^n_{i,j} - W^n_{i',j'})) + h(\frac{T^n_{i,j} + T^n_{i',j'}}{2})) = \tilde{\lambda}(T^n_{i'',j''} - 2T^n_{i,j} + T^n_{i',j'}) \tag{3.60}$$

$$W^n_{i,j} = (1 + \frac{\mu_0(T^n_{i,j}) + \mu_0(T^n_{i',j'})}{2}\frac{k_1(s^n_{i,j}) + k_1(s^n_{i',j'})}{k_2(s^n_{i,j}) + k_2(s^n_{i',j'})})^{-1}\frac{T^n_{i,j} + T^n_{i',j'}}{2} \tag{3.61}$$

The solution technique is iterative and involves the linearization of the non-linear product terms for the evaluation of the finite difference coefficients. For the following implicit difference scheme for saturation and temperature we are using Newton's algorithm and for the linear system of equations we apply BiCGStab with a ILU(0) as a preconditioner (Appendix2.5). The system of equations governing the distribution of oil and water pressure, saturation and temperature are non-linear and strongly coupled.

A convergence criteria of 0.1% between successive iteratios on each time layer has been used in the present study. For the region size $20m \times 20m$, a grid consisting of 200×200 nodes for each of the variables p, s, T has been used. Convergence of numerical results has been tested by simulating the above results at spacial resolutions of 100×100, 200×200 and 400×400 . A similar finger structurus has been observed in the latter two cases and this level of refinement of 200×200 has been found to be adequate to obtain a grid-independent solution. The time step for all the calculations was kept at 0.005.

Rock properties in well-studied geothermal reservoirs are determined from field measurement data. The non-dimentioal parameters identified in Section 2 are used here to scale

down our numerical solutions. Typical non-dimensional reservoir parameters are presented in Table 3.2 below.

3.5 Results and discussion

Results obtained from the numerical simulation of oil displacement problem from a porous medium are discussed in the present section. The above analysis for the models without capillary and gravity allows us to investigate the influence the viscosity of displaced fluid on the viscous instability of the front. The instability of the front depends on a variety of factors such as an fluid viscosities and it's dependence on temperature, porosity and absolute and relative permeabilities of the medium. However, for the present discussion we are fixing the porosity and absolute permeability as constants. The displacement was modeled for different viscosity ratios μ_0 which may or may not depend on temperature. The parameters used in the following study are presented in Table 3.1. The model was employed to study the influence of displacement conditions and of the properties of porous medium on the development of the hydrodynamic instability in displacement of oil by hot and cold water. The temperature dependence of hot oil viscosity could be approximated by the exponential function $\mu_2(T) = e^{A+B/T}$, where we can determine coefficients A and B to observe stable and unstable regimes.

The following scenarios are addressed: two stability cases in isothermal flow($A = 0, B = 0$; $A = 3, B = 0$; Case 1-2) and two stability cases in non-isothermal flow ($A = -4, B = 4$; $A = 1, B = 6$; Case 3-4) in Table 3.3.

- Test case 1 describes a isothermal displacement process with the the viscosity of water is equal to the viscosity of water which is constant everywhere, i.e $\mu_0 = 1$. With time $t \to \infty$ the short wavelength perturbations decay, as they correspond to high, and thus stable, amplitudes. Hence the flow is characterized by the stable regime as shown in Figure (3.4).

- For the test case 2 we again consider an isothermal displacement front where the viscosity

of water is much less than the viscosity of oil, i.e $\mu_0 \approx 1/20, A = 3, B = 0$; The result of the modeling of instability development is shown on Figure (3.5). The pressure redistribution in the medium leads to accelerated growth of the fingers in displacing fluid. The obtained pattern of growth of the fingers is in qualitative agreement with the results of experimental investigations of the Saffman- Taylor instability and with the linear stability conditions for isothermal regime.

- Test case 3 simulates non-isothermal regime with the viscosity of oil depend on temperature. Based on the linear stability condition for non-isothermal case we pick two parameters $A = -4, B = 4$; and numerically verify that the flow become stable with the time. As shown in Figure (3.6) the saturation front is stable since the front is strong and no fingering behind is observed, which is in agreement with the linear stability results.

- Test case 4 shows non-isothermal regime with the viscosity of oil dependence on temperature. Based on the linear stability condition for non-isothermal case we again pick two parameters $A = 1, B = 6$; and numerically verify that the flow stays unstable with the extended period of time. The saturation front stays unstable and the simulation results are shown in Figure (3.7).

We can find analytically the growth rate σ from from equations (3.29) and (3.52), and calculate the amplitudes of instability $X(t) = X_0 e^{\sigma t}$ for cases 2 and 4. We calculate the dependence of $\alpha = ln(X/X_0)$ as a function of time. We see that that α is linear in the case of one-dimensional fluid flow since the velocity $\omega = 1$. But for the two dimensional flow we can not make this assumption, since the velocity of the flow is not constant anymore so after calculating equation (3.6) we can see that α is not linear with time but has the common tendency for amplitude to increase with $t \to \infty$ which is supported in Figure (3.8). We can observe that the linear growth rate is indeed two times as much in non-isothermal case than in non-isothermal.

3.6 Conclusions

We developed a non-isothermal model for the immiscible fluid flow in porous media. We investigated the conditions for instability in both isothermal and non-isothermal cases. We performed stability analysis for the non-isothermal case and found conditions when flow will be stable with the inclusion of temperature. A set of numerical experiments for isothermal and non-isothermal immiscible flow in a horizontal open fracture is performed to verify the stability regimes. Our study leads to the following major conclusions:

- The stability of planar fronts in two phase immiscible flow in a porous medium is governed by the mobility difference between the two phases. With realistic relative permeability ratios, to stabilize a front in which water is displacing oil, the displacing fluid should be an oil-rich mixture of oil and water. The analysis here indicate of how these fronts can be analyzed. In particular, the Saffman-Taylor analysis of sharp fronts can be extended to allow for variable saturations with the residual oil, demonstrating that stability depends on the interplay between the hyperbolic conservation law derived by Buckley and Leverett [16] and the elliptic equation that expresses incompressibility of the two phase mixture.

- The linear stability analysis made it clear that the dynamics of the front in non-isothermal case is governed by the mobility difference between the two phases.

- Necessary conditions for the breakdown of stability conditions of the immiscible non-isothermal fluid flow in porous media are presented as a phase diagram.

- The amplitude of the instability has the twice of the growth rate in non-isothermal regime versus isothermal regime.

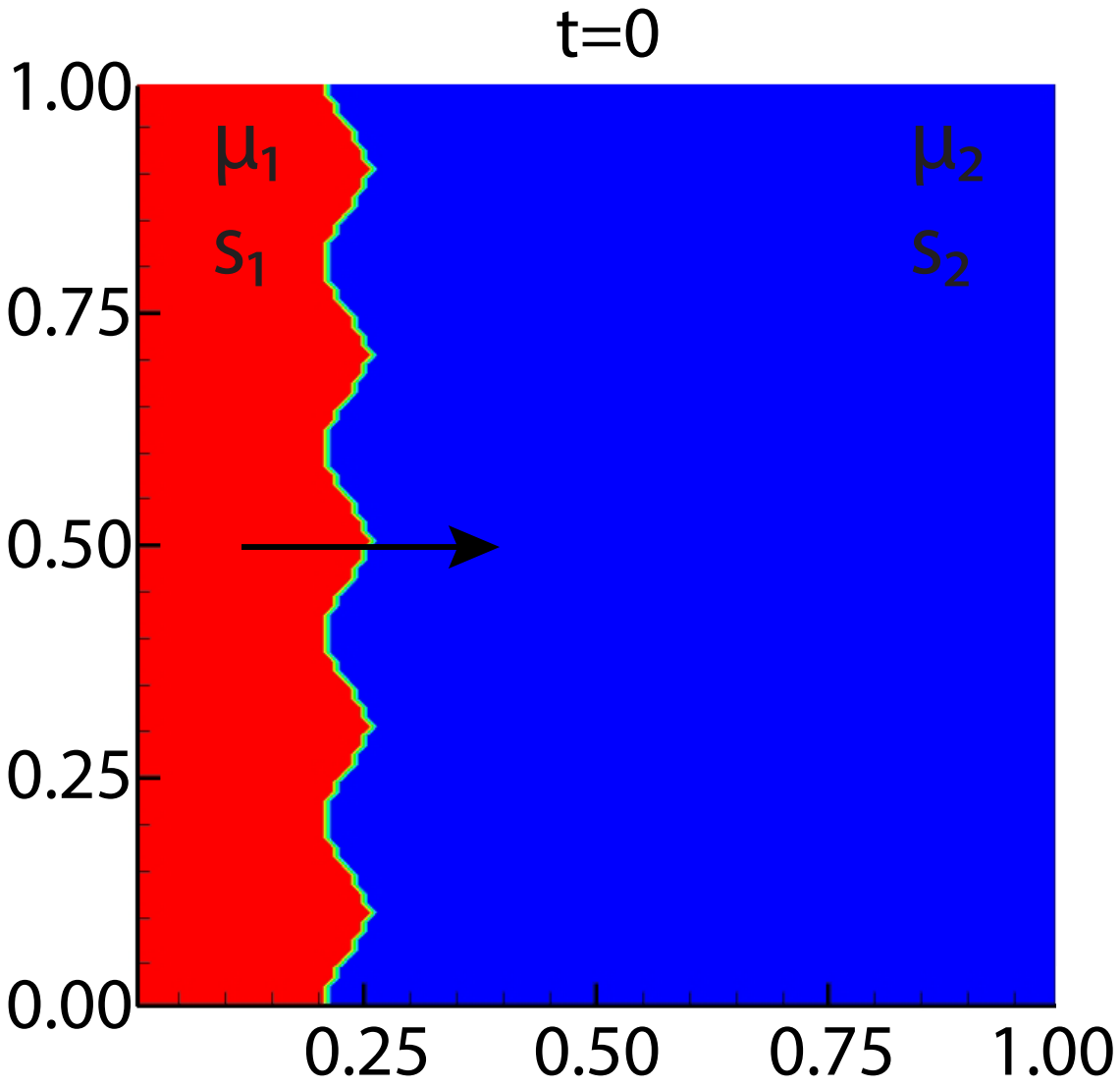

Figure 3.1: Initial distribution at $t = 0$ for a two-dimensional immiscible flow in a horizontal homogeneous porous medium. A fluid with viscosity μ_1, saturation s_1 is driven forward by the pressure gradient to displace the second one of viscosity μ_2 and saturation s_2.

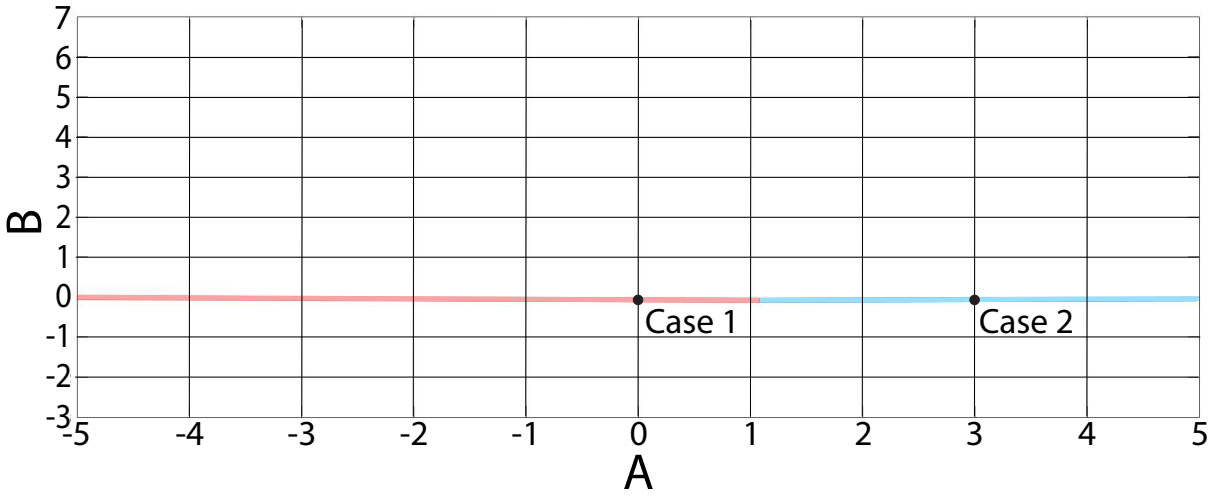

Figure 3.2: Region of validity for stability region for isothermal flow, spanned by viscosity phases. Case 1, $(A,B) = (0,0)$,satisfies and case 2, $(A,B) = (3,0)$, violates stability conditions.

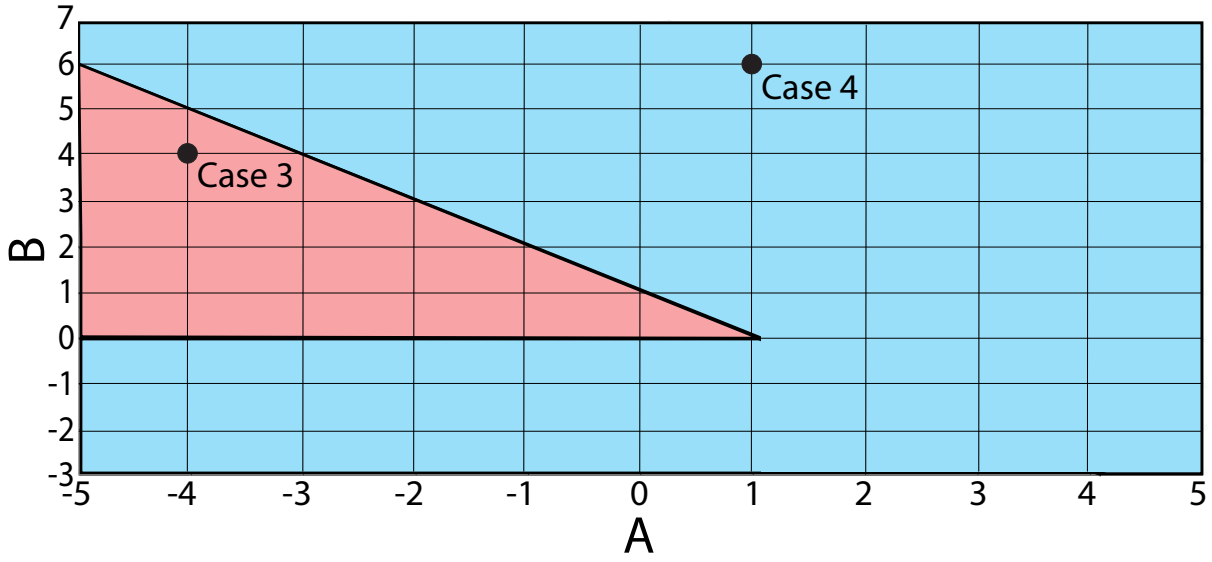

Figure 3.3: Region of validity for stability region for non-isothermal flow, spanned by viscosity phases. Case 3, $(A,B) = (-4,4)$, satisfies and case 4, $(A,B) = (1,6)$, violates stability conditions.

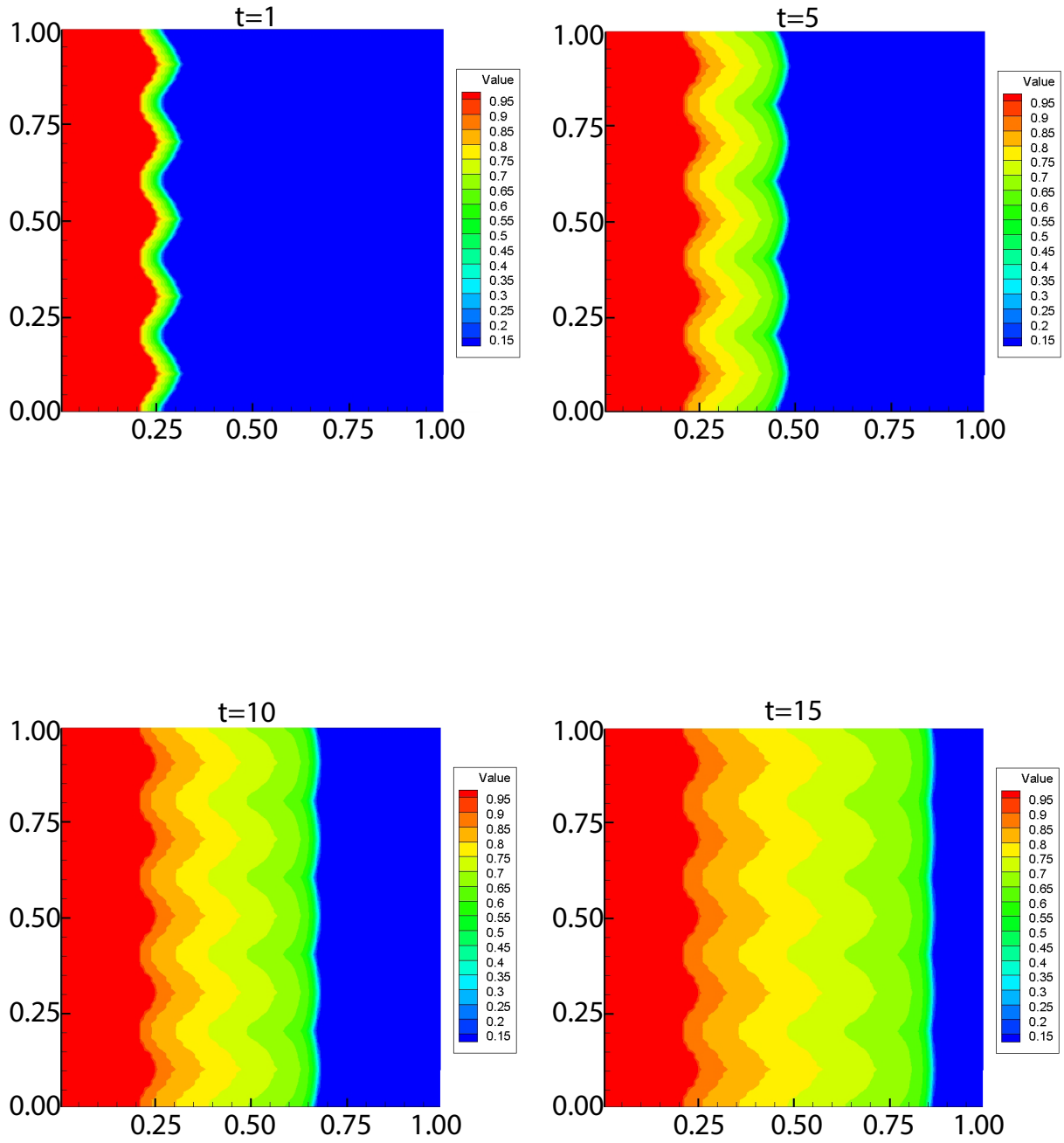

Figure 3.4: Temporal snapshots, at $t = 1, t = 5, t = 10, t = 15$ of the water saturation s for Case 1, $A = 0, B = 0$, which satisfies stability conditions of isothermal regime.

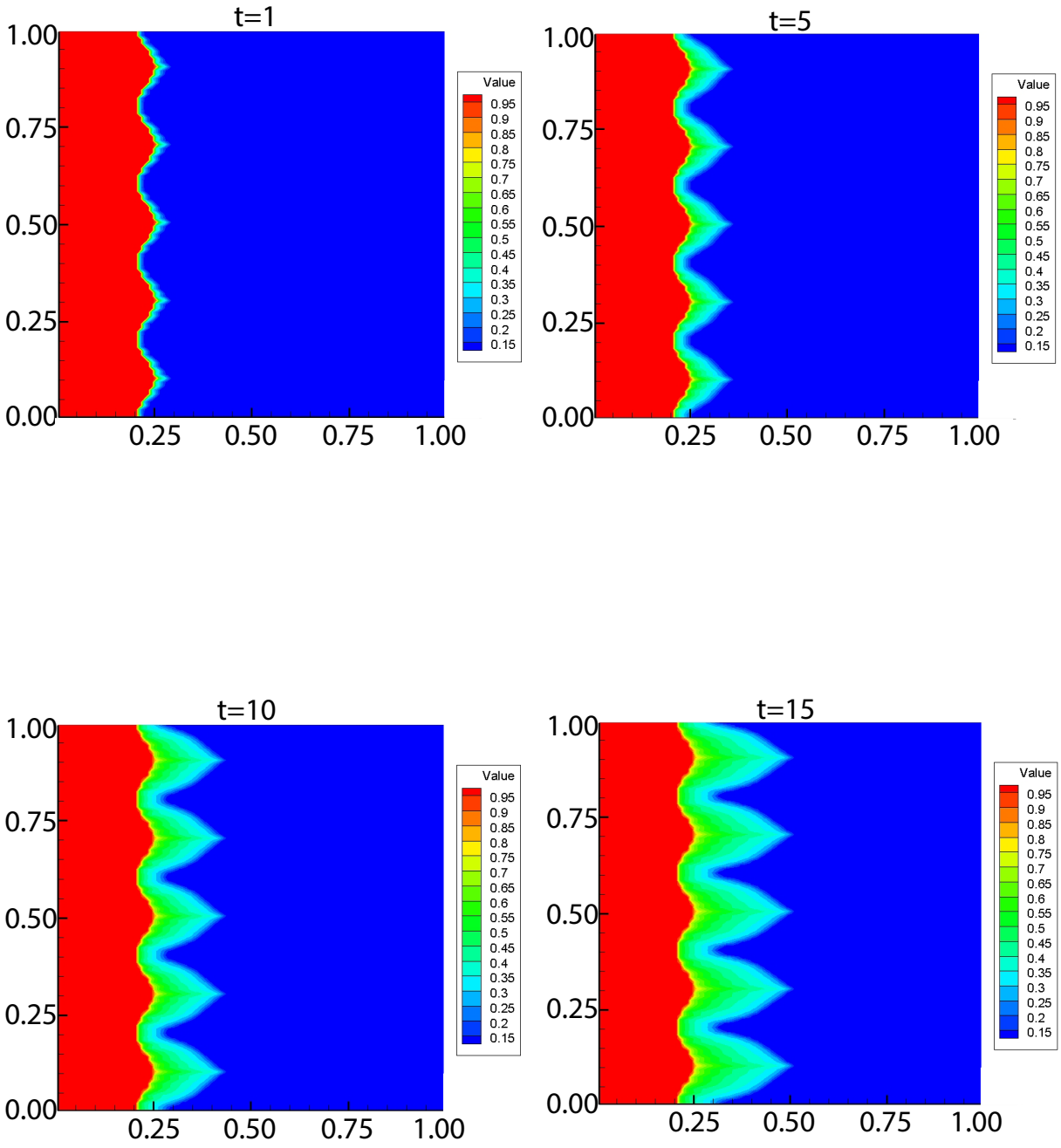

Figure 3.5: Temporal snapshots, at $t = 1, t = 5, t = 10, t = 15$ of the water saturation s for Case 2, $A = 3, B = 0$, which violates stability conditions of isothermal regime.

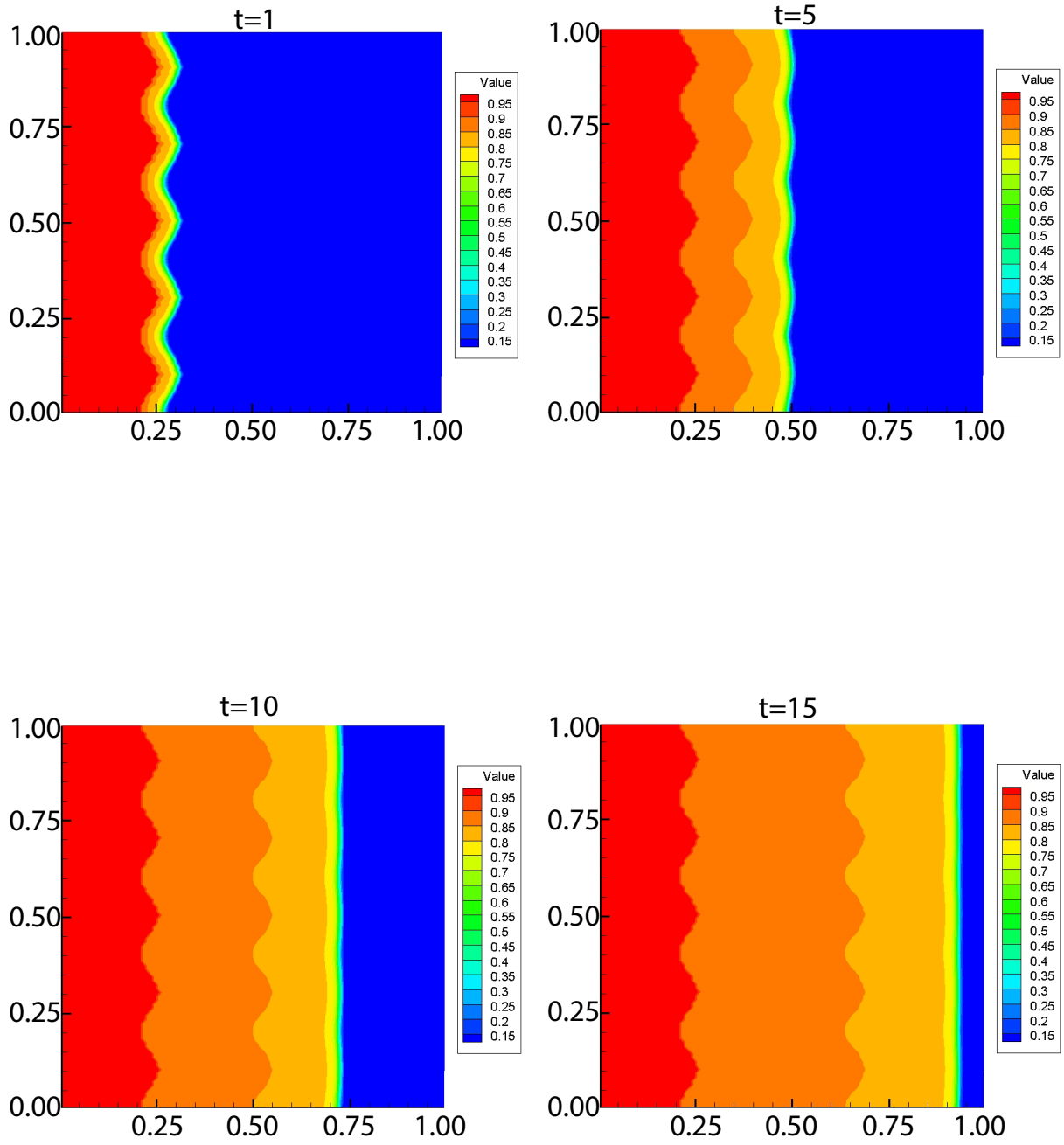

Figure 3.6: Temporal snapshots, at $t = 1, t = 5, t = 10, t = 15$ of the water saturation s for Case 3, $A = -4, B = 4$, which satisfies stability conditions of non-isothermal regime.

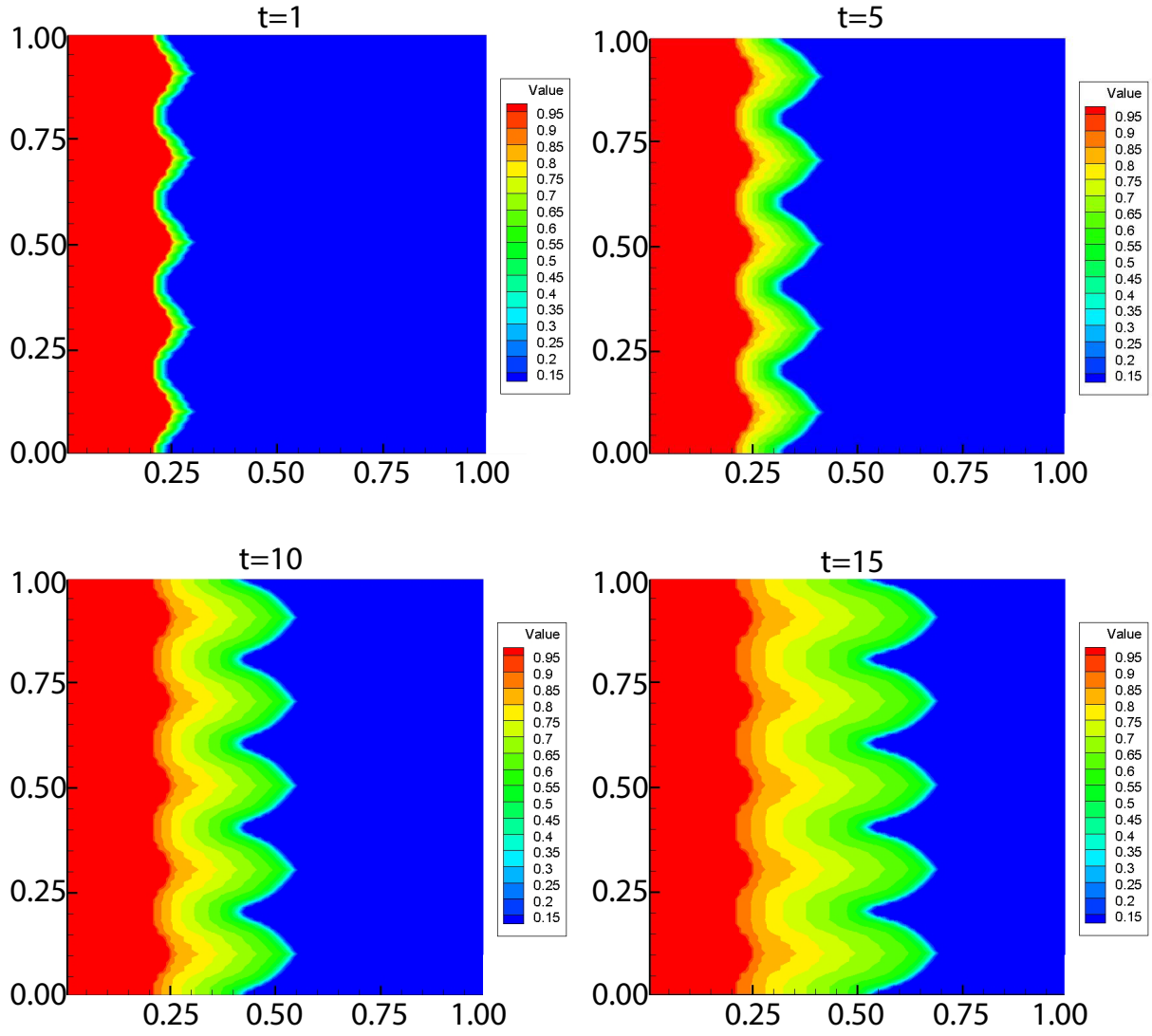

Figure 3.7: Temporal snapshots, at $t = 1, t = 5, t = 10, t = 15$ of the water saturation s for Case 4, $A = 1, B = 6$, which violates stability conditions of non-isothermal regime.

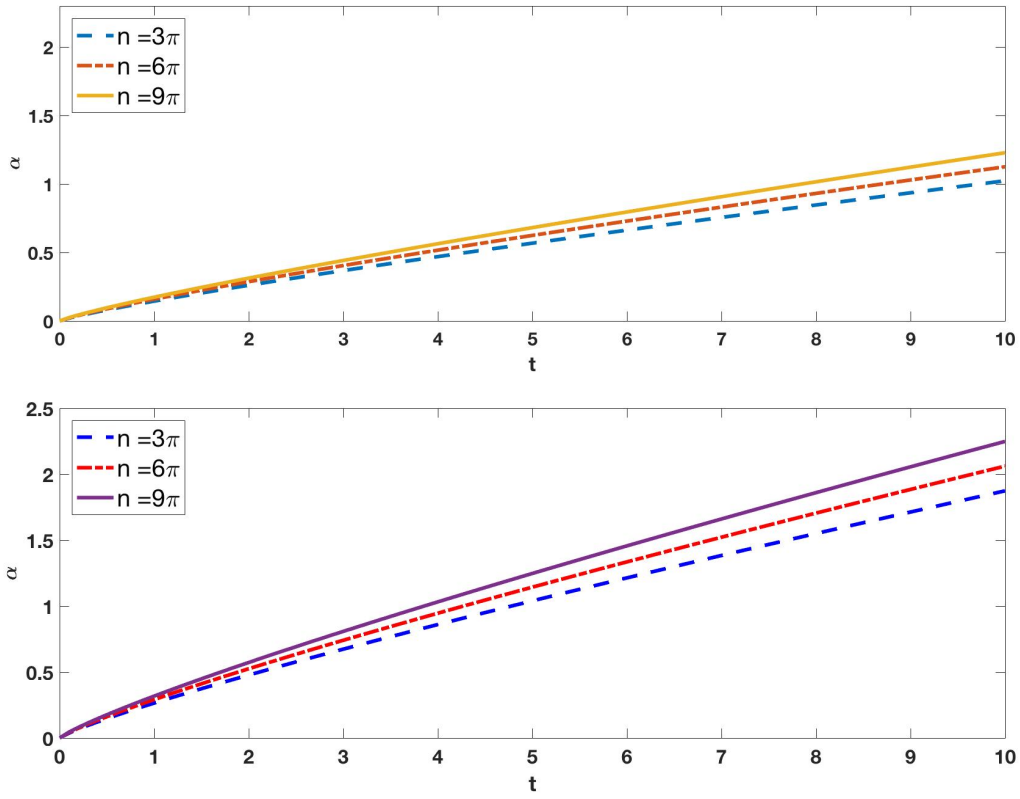

Figure 3.8: The nonlinear amplitude of the front for saturation s for isothermal and non-isothermal regimes at $t = 10$ for perturbation wavenumbers $n = 3\pi$, $n = 6\pi$, $n = 9\pi$ corresponding to the non-linear velocity of the flow ω.

Table 3.1: Initial conditions for saturation of water s, temperature T and pressure p for isothermal and non-isothermal regimes.

Parameters	Symbol	Value	SI Unit
Initial Saturaton	s_{in}	1	[-]
Final Saturaton	s_{fin}	0.1	[-]
Initial Pressure	p_{in}	$100 * 10^5$	$[ML^{-1}T^{-2}]$
Final Pressure	p_{fin}	$50 * 10^5$	$[ML^{-1}T^{-2}]$
Initial Temperature	T_{in}	$273.0 + 95.0$	$[\Theta]$
Final Temperature	T_{fin}	$273.0 + 5.0$	$[\Theta]$

Table 3.2: Non-dimensionalized geothermal reservoir parameters for Darcy, continuity and heat equations.

Parameters	Symbol	Value	SI Unit
Porosity	m	0.2	[-]
Saturated oil	s_0	0.1	[-]
Absolute Permeability	K	1.0	$[LT^{-1}]$
Density of water,	ρ_1	$1.0*10^3$	$[ML^{-3}]$
Density of oil,	ρ_2	$1.0*10^3$	$[ML^{-3}]$
Density of the mixture	ρ_{mix}	$2.2*10^3$	$[ML^{-3}]$
Viscosity of water	μ_1	$1.0*10^{-3}$	$[MT^{-1}L^{-1}]$
Viscosity of oil	μ_2	$e^{A+B/T}$	$[MT^{-1}L^{-1}]$
Thermal conductivity	λ	1.1	$[MLT^{-3}\Theta^{-1}]$
Heat capacity of water ($V = const$)	C_{v_1}	$4.0*10^3$	$[L^2MT^{-2}\Theta^{-1}]$
Heat capacity of oil ($V = const$)	C_{v_2}	$0.8*10^3$	$[L^2MT^{-2}\Theta^{-1}]$
Heat capacity of mixture ($V = const$)	$C_{v_{mix}}$	$3.3*10^3$	$[L^2MT^{-2}\Theta^{-1}]$

Table 3.3: Test cases for total mobility function μ_0 in isothermal and non-isothermal flow regimes.

Parameter	Case 1	Case 2	Case 3	Case 4
A	0.0	3.0	-4.0	1.0
B	0.0	0.0	4.0	6.0

Natalia Siuliukina, Daniel M. Tartakovsky, “Viscous Fingering in Non-Isothermal Filtration’, *in preparation*,

Chapter 4

Global sensitivity analyses using a surrogate model based on support vector regression approach

4.1 Introduction

For several decades, one of the most important research and real world applications in the hydrogeological sciences has been related to aquifer contamination. The work has been studied from the scientific and engineering point of view and related to prediction and remediation of contaminant plumes in natural environment. Most of these problems are arising because of uncertainties related to contaminant sources ([33]). For example, it is often to not know the location of contaminant sources and the properties of geochemical solutes. Also, the data related to groundwater mixtures are collected at multiple wells where the samples are taken with some extended period of time where the data that is been measured is being affected to some errors and uncertainties.

It is very difficult to provide accurate solution complex geophysics models due to the

various factors that all affecting the system simultaneously. It is also very challenging to identify the original groundwater types that is found in aquifer ([91]). The task is solved by using inverse models for groundwater mixing processes in an aquifer where the model calibrates against the available observation data. Respectively, the observation data is characterized by the spatial and temporal distribution of the observed geochemical data ([43], [8]). In these models, we need to simulate numerous different geochemical properties which further complicates the analysis. This often leads to solution involving systems such as coupled partial differential equations which require immense computational power for every iteration. Current analysis of groundwater contamination are implementing various statistical and machine learning techniques ([30], [80]). They have been utilized to build surrogate models based on observational data for substitution of the much more complex and time-consuming physical models used to simulate contamination levels. Such surrogate models have been used to predict contaminant levels in regional groundwater sites ([50]).

Several years years ago a site has began pumping tests at the wells located on the laboratory property with a chromium plume in a regional aquifer. The purpose of pumping ito understand the properties of the plume and evaluate the potential for pumping to remove chromium since the concentrations of chromium exceeded limits to ensure contaminants do no threaten human health or the environment. A network of 20 monitoring wells is used to define and monitor the concentrations of chromium.

In this chapter, we utilize a Supporting Vector Regression (SVR) method for creation a surrogate model capable of describing the behavior of a set of wells with the various input parameters, based on a limited amount of data samples. SVR is applied to analyze and deconstruct the groundwater geochemistry observed in the regional aquifer for characterization of contaminant sources. Global Sensitivity Analysis (GSA) method is aimed at investigating the propagation of uncertainty through a numerical model and a model that has been trained by SVR method, and specifically assessing the contribution to the model output uncertainty from different uncertain

input factors.

Using synthetic and real world site data, we demonstrate that SVR method is capable of accurately build a surrogate model of set of monitoring wells, using only a limited amount of experimental data and simulation results. We use data from a group of four physical wells with six input parameters. We train and build an SVR model on this training set and check its predictions with the real measured concentrations and on a set of simulation data derived by the real physical model developed specifically for the site chromium plume problem.

Finally, we performed global sensitivity analysis on both a) the physical model of these wells developed previously and b) on our new SVR model. The comparison of the GSA results in these two cases demonstrates the feasibility and accuracy of the new SVR model as a fast tool for sensitivity analysis.

In this chapter, we analyze how SVR surrogate model performs when it is applied to approximate the model-predicted behavior of complex time- and scale-dependent contaminant transport in an geologic porous medium (aquifer). Having experimental and simulation data we train an SVR classifier on a limited amount of samples to reproduce the general behavior of the model. Then, using the trained SVR model we predict the contaminant transport and compare the SVR predictions with a large amount of data points obtained by simulations performed by a real physical model. This comparison is necessary to verify and validate the SVR model. Finally, we apply the validated SVR model to understand the behavior of the investigated complex system on a bigger scale [77].

4.2 Methodology

4.2.1 Physical model

We chose to vary the following parameters in the model: the flow velocity in the x-direction of contaminant, the contaminant dispersivity, the time-scale dispersivity of the con-

taminant, the contaminant flux, the start time and the end time, the x-coordinate of the source, and the y-coordinate of the source.

4.2.2 Surrogate models

In a large number of engineering fields there is a need of accurate theoretical models for examining complex real-world phenomena. Many such theoretical models have been built and computationally implemented. Usually, the need to provide a detailed knowledge about a system results in extremely computationally intensive model which outputs depend on many, often poorly known, input parameters. The analysis of the role of these parameters and their sensitivity is an important task that results in simulation times of several hours, several days, or even several weeks per model. These long running times are in a sharp contrast to the contemporary need for real-time answers and efficient decision making.

Recently, another type of effective and fast approaches have become available to model complex real-world systems. Many of these approaches are based on a variety of supervised machine learning methods and have been termed surrogate models. In general, surrogate (aka meta) models ignore the underlying mechanisms of the specific physical model and examine the problem as a black-box that provides certain output for a given input. Usually, the surrogate models are build based on output data from computationally intensive physical model simulations (or experimental measurements) and their variation as a function of a small set input parameters. The trained surrogate model is then applied to a much larger set of input parameters, and after verifying and validating its accuracy, it is used to provide fast (although approximate) results that otherwise may take many weeks to compute. Such models have been already applied in many engineering fields such as electronics [22], aerodynamics [2], and hydrology [65].

The surrogate models based on statistical learning theory [34] allow accurate and efficient approximation of the relationship between the input and output of a complex system, based only on a limited set of training data. Surrogate modeling replaces the original modeling

by iterative re-optimization of analytically tractable and computationally cheap meta-models. While not a trivial task, a proper construction of an approximate model can accurately emulate the behavior of the original model as a function of the input parameters. As such, the use of a suitable surrogate model makes it possible to perform computationally efficient analyses such as prediction, optimization, sensitivity analysis, and uncertainty quantification.

Some of popular methods for developing surrogate models are polynomial response surfaces [68], kriging [37], support vector machines [22], support vector regression [65], space mapping [52], and artificial neural networks [59].

Our study builds and evaluates the performance of a surrogate model based on statistical learning theory, viz., support vector regression (SVR) model, for approximating the behavior of chromium contaminant transport in the local site aquifer.

4.2.3 Support vector regression technique

The Support Vector Regression (SVR) method was developed in the 90s [23] based on the concept of Supporting Vector Machine [14]. In fact, the SVR method is one of the most frequently used models for regression [88]. Due to its industrial concept, SVR is used frequently as a tool for creation of surrogate models applicable in various fields.

In our paper, we analyze how an SVR surrogate model performs when it is applied to approximate the model-predicted behavior of complex time- and scale-dependent contaminant transport in an geologic porous medium (aquifer). Having experimental and simulation data we train an SVR classifier on a limited amount of samples to reproduce the general behavior of the model. Then, using the trained SVR model we predict the contaminant transport parameters and compare the SVR predictions with a large amount of data points obtained by simulations performed by a real physical model. This comparison is necessary to verify and validate the SVR model. Finally, we apply the validated SVR model to understand the behavior of the investigated complex system on a bigger scale [77]. Below we will describe shortly the core concepts of the

SVR technique.

4.2.4 SVR method

Let's consider a data set (the SVR training set), $D = \{(x_1, y_1), ..., (x_l, y_l)\}, x \in R^n, y \in R$, that could be described (approximated) by a linear function,

$$f(x) = \langle \omega, x \rangle + b, \tag{4.1}$$

where $\langle \cdot, \cdot \rangle$ denotes the dot-product in R^n, x_i denotes the set of the input parameters, and y_i is the output of the physical model. To produce an accurate description and prediction of the results from the physical model we need to build function $f(x)$ that will demonstrate relatively small deviations from the target outputs y_i at the set of input parameters x_i. In fact, we will construct our SVR classifier in such a way that it will not accept errors outside of an interval $\pm\varepsilon$. Geometrically, Figure (4.1), it is clear that this can be done by minimizing the vector norm $\|\omega\|^2$, which is a convex optimization problem, that is, we have to minimize

$$min \frac{1}{2} \omega^T \cdot \omega$$

subject to the constraints,

$$\begin{aligned} y_i - \langle \omega, x_i \rangle - b &\leq \varepsilon \\ \langle \omega, x_i \rangle + b - y_i &\leq \varepsilon. \end{aligned} \tag{4.2}$$

Usually, to find such a function, $f(x)$, it is needed to allow some more errors. This can be done by introducing of so called slack variables $\xi_i^+, \xi_i^- \geq 0$, representing the upper and lower constraints on the outputs of the system. Then, the optimal regression function is given by the

minimum of,

$$min\frac{1}{2}\|\omega\|^2 + C\sum_{i=1}^{l}(\xi_i^+ + \xi_i^-), \tag{4.3}$$

subject to

$$\begin{aligned} & y_i - \langle \omega, x_i \rangle - b \leq \varepsilon + \xi_i^+ \\ & \langle \omega, x_i \rangle + b - y_i \leq \varepsilon + \xi_i^-. \\ & \xi_i^+, \xi_i^- \geq 0. \end{aligned} \tag{4.4}$$

Here the constant $C > 0$ is a trade-off parameter (aka penalty parameter) between model complexity and the degree to which errors bigger than ε are tolerated.

We can solve the above optimization problem by constructing Lagrange function with primal objective function (4.3) and corresponding constraints by introducing Lagrange multipliers $\alpha_i^+, \alpha_i^-, \nu_i^+, \nu_i^- \geq 0$.

$$\begin{aligned} L = \tfrac{1}{2}\|\omega\|^2 + C\sum_{i=1}^{l}(\xi_i^+ + \xi_i^-) - (\nu_i^+\xi_i^+\nu_i^-\xi_i^-) - \\ -\alpha_i^+(\varepsilon + \xi_i^+ + y_i - \langle \omega, x_i \rangle - b) - \alpha_i^-(\varepsilon + \xi_i^- + \langle \omega, x_i \rangle + b - y_i), \end{aligned} \tag{4.5}$$

The above Lagrangian has to be minimized with respect to the primal variables: ω, b, ξ and then maximized with respect to ν and α (the dual variables).

$$\frac{\partial L}{\partial b} = 0, \quad \frac{\partial L}{\partial \omega} = 0, \quad \frac{\partial L}{\partial \xi_i^+} = 0, \quad \frac{\partial L}{\partial \xi_i^-} = 0. \tag{4.6}$$

The above equations yields the dual optimization problem:

$$L = \begin{cases} -\frac{1}{2}\sum_{i,j=1}^{l}(\alpha_i^+ - \alpha_i^-)(\alpha_j^+ - \alpha_j^-)\langle x_i, x_j \rangle - \\ \quad -\varepsilon\sum_{i=1}^{l}(\alpha_i^+ + \alpha_i^-) + \sum_{i=1}^{l} y_i(\alpha_i^+ - \alpha_i^-), \end{cases} \tag{4.7}$$

subject to

$$\begin{cases} \sum_{i=1}^{l} (\alpha_i^+ - \alpha_i^-) = 0 \\ \\ \alpha_i^+, \alpha_i^- \in [0, C]. \end{cases} \tag{4.8}$$

After solving the dual optimization problem for $\alpha_i^{\pm}$ we obtain ω that is a linear combination of the training points x_i.

$$\omega = \sum_{i=1}^{l} (\alpha_i^+ - \alpha_i^-) x_i, \tag{4.9}$$

and therefore

$$f(x) = \sum_{i=1}^{l} (\alpha_i^+ - \alpha_i^-) \left\langle x_i x \right\rangle + b. \tag{4.10}$$

4.2.5 Parameter b

To find the parameter b we need to apply Karush - Kuhn - Tucker (KKT) conditions (ref): At the optimal solution the product between the dual variables has to vanish:

$$\alpha_i^+ (\varepsilon + \xi_i^+ - y_i + (\omega \cdot x_i) + b) = 0, \tag{4.11}$$

$$\alpha_i^- (\varepsilon + \xi_i^- + y_i - (\omega \cdot x_i) - b) = 0, \tag{4.12}$$

and

$$(C - \alpha_i^+) \xi_i^+ = 0, \tag{4.13}$$

$$(C - \alpha_i^-) \xi_i^- = 0. \tag{4.14}$$

There never be a set of dual variables α_i^+, α_i^- which are both non-zero in the same time as it

would require non-zero slacks in both directions. From here we can compute b as:

$$b = -\varepsilon + y_i - (\omega \cdot x_i), \quad \alpha_i^+ \in (0, C) \tag{4.15}$$

$$b = \varepsilon + y_i - (\omega \cdot x_i), \quad \alpha_i^- \in (0, C) \tag{4.16}$$

So far we described the procedure of finding a linear function $f(x)$ ([65], [62], [41]). If such a linear function does not exist, i.e., the problem is non-linear, we can apply the "kernel trick" [14]. That is, we can map the data, by using the "Vapnik mapping" ([96]) $\phi(x)$ that maps x into a higher dimensional feature space, where we will have again a linear case that we can solve using the described above procedure. In fact, in the linear case we are only dealing with the inner product $x \cdot x$ and hence in the nonlinear case (after the mapping) we will need only $\phi(x) \cdot \phi(x)$. We can actually choose the mapping ϕ and employ different basis functions by using $\psi = \phi \cdot \phi$,

$$f(x) = \sum_{i=1}^{l} (\alpha_i^+ - \alpha_i^-) \psi_i + b. \tag{4.17}$$

The kernel trick allows us to compute the inner products between the images of all pairs of data in the feature space. This operation is often computationally cheaper than the explicit computation of the coordinates. There are different choices for the type of kernel functions, $\phi(x)$, the most common are the linear, polynomial, Gaussian and sigmoid kernels ([74]). We performed preliminary tests on the data using different kernel functions and determined that the Gaussian kernel is the one giving the best results. The Gaussian kernel is described by the formula:

$$\phi(x_i, x_j) = exp(-\gamma ||x_i - x_j||^2). \tag{4.18}$$

After the kernel substitution we can find the support vectors by solving the dual optimization problem, that is, by minimizing

$$L = \begin{cases} -\frac{1}{2}\sum_{i,j=1}^{l}(\alpha_i^+ - \alpha_i^-)(\alpha_j^+ - \alpha_j^-)\phi(x_i x_j) - \\ \quad -\varepsilon\sum_{i=1}^{l}(\alpha_i^+ + \alpha_i^-) + \sum_{i=1}^{l} y_i(\alpha_i^+ - \alpha_i^-). \end{cases} \tag{4.19}$$

subject to

$$\begin{cases} \sum_{i=1}^{l}(\alpha_i^+ - \alpha_i^-) = 0 \\ \quad \alpha_i^+, \alpha_i^- \in [0, C]. \end{cases} \tag{4.20}$$

4.2.6 Examples for kernels

To increase the reading facility, the kernel function could be designed as

$$K(x_i, x_j) = \phi(x_i)\phi(x_j) = Q_{ij}, \tag{4.21}$$

The matrix Q_{ij} is called kernel matrix and and contains values of the kernel function. It is useful to save kernel function values in this way for computational reasons. Some of the common examples of kernel functonals are represented below:

1. Polynomial kernel $K(x_i, x_j)$ with the parameters $p, c \in N$

$$K(x_i, x_j) = (x_i \cdot x_j + c)^p, \tag{4.22}$$

2. Hyperbolic tangent kernel $K(x_i, x_j)$ with the parameter $\Theta > 0$

$$K(x_i, x_j) = \tanh(\theta + \phi(x_i \cdot x_j)), \tag{4.23}$$

3. Gaussian radial basis function (RBF) kernel $K(x_i, x_j)$ with the parameters $\gamma > 0$

$$K(x_i, x_j) = exp(-\gamma \|x_i - x_j\|^2)), \tag{4.24}$$

4. Anova radial basis kernel $K(x_i, x_j)$ with the parameter σ, k, d

$$K(x_i, x_j) = \sum_{i=1}^{n} \exp(-\sigma(x_i^k - x_j^k)^2)^d. \tag{4.25}$$

4.2.7 eFAST global sensitivity analysis

The computational cost associated with the use of high-fidelity computational fluid dynamics (CFD) models poses a serious impediment to the successful application of formal sensitivity analysis in engineering design. In many engineering design problems, thousands of function evaluations may be required to undertake a sensitivity analysis. As a result, CFD models are often impractical to use for design sensitivity analyses. In contrast, surrogate models are compact and cheap to evaluate (order of seconds or less) and can therefore be easily used for such tasks.

The foundational idea of global sensitivity analysis (GSA) is to quantify how input parameter variations affect our model output. Measuring the sensitivity of parameters is critical when building any sort of precise and robust model. Although many have preferred the use of GSA algorithms such as Monte Carlo [55], we have decided to use the extended Fourier Amplitude Sensitivity Test (eFAST) for our sensitivity calculations due to it's computational speed. eFAST allows the computation of both the independent contribution of each parameter to model uncertainty ("main sensitivity indices"), and also variance due to a parameter including all interactions between other parameters ("total sensitivity indices"). Although eFAST cannot calculate the contributions to uncertainty of every interaction like other GSA algorithms such as Monte Carlo, this would require $N_s(2^n - 1)$ model evaluations where n is the number of parameters and

N_s is our sample size. Calculating just the main and total sensitivity indices, on the other hand, requires $2(N_s n)$ model evaluations. Studies have shown that typically eFAST is much more efficient than Monte Carlo when calculating main and total sensitivity indices [1]. For our purposes, the main and total sensitivity indices will give enough intuition to determine which parameters are the greatest contributors to model uncertainty.

Variance-based GSA methods are utilized in this project as they are attractive for two main reasons: they allow a quantitative breakdown regarding each parameters independent contribution to the uncertainty of the model, and they also provide insight into variance due to interactions between parameters in non-additive models. Often the most significant issue in employing variance-based SA is the computational cost of the thousands of model evaluations that are typically required. Variance-based sensitivity analysis methods such as Sobol's Monte Carlo technique or the extended Fourier Amplitude Sensitivity Test (eFAST) are attractive for a few reasons. First, they are absolute measures, that is, their value can be used to assess the relative importance of the input factors but it also has a clear interpretation: it is the fraction of output variance due to uncertainty in the factor under study. Second, since they can be approximated by an algebraic formula [1], their computation is quite straightforward and does not require to specify any tuning parameter besides the number of random samples that should be employed. One major limitation of this approach is that the number of random samples needs to be quite high to obtain a reliable approximation of the variance-based measures in many cases, which can become a problem in case of time-consuming simulation models.

The eFAST algorithm exploits properties of the frequency domain to calculate main and total sensitivity indices more efficiently than traditional GSA methods such as a Monte Carlo algorithm. The key idea behind the strength of eFAST is the ergodic theorem. The ergodic theorem allows us to reduce the dimensionality of a Fourier series expansion of the model from n to 1. We use the following transformation to accomplish this:

eFAST begins by representing the model function as a multi-dimensional Fourier series

expansion:

$$f(\mathbf{X}) = \sum_{m_1=-\infty}^{\infty} \sum_{m_2=-\infty}^{\infty} ... \sum_{m_n=-\infty}^{\infty} C_{m_1 m_2 ... m_n} exp[2\pi i(m_1 X_1 + m_2 X_2 + ... + m_n X_n)] \tag{4.26}$$

for integers $m_1, m_2, ..., m_n$ where $\mathbf{X} = \left\langle X_1, X_2, ..., X_n \right\rangle$

The coefficients of the expansion are, respectively:

$$A_{m_j} = \int_0^1 ... \int_0^1 f(X_1, X_2, ..., X_n) \cos(2\pi m_j X_j) \, dX_1 dX_2 ... dX_3 \tag{4.27}$$

$$B_{m_j} = \int_0^1 ... \int_0^1 f(X_1, X_2, ..., X_n) \sin(2\pi m_j X_j) \, dX_1 dX_2 ... dX_3 \tag{4.28}$$

$$x_i(s) = \frac{1}{2} + \arcsin(sin(\omega_i s + \phi_i)) \tag{4.29}$$

[1]

This transformation creates a set of straight lines, approximately uniformly distributed across the parameter space. ϕ_i is a random phase shift chosen between $[0, 2\pi)$ which allows the search curve to begin at any point. By searching the entire parameter space with only a single parameter, eFAST is able to calculate accurate sensitivity indices using far less model evaluations than a Monte Carlo analysis.

The following figure demonstrates the accuracy of eFAST over Monte Carlo. Both algorithms were tested on the Sobol G function, defined as:

$$\prod_{i=1}^{d} |\frac{4x_i - 2| + a_i}{1 + a_i} \tag{4.30}$$

where

$$a_i = \frac{i-2}{2}, \quad i\varepsilon[1, ..., d] \tag{4.31}$$

As the Sobol G function's sensitivity indices [6] can be calculated analytically, it is almost universally used as a benchmark for global sensitivity analysis algorithms. Both eFAST and Monte Carlo were tested over $N = 15,000$ iterations. Both algorithms center around the analytical indices but the spread for eFAST is significantly smaller as we can see in Figure (4.2).

$$A_{m_j} \approx \frac{1}{2\pi} \int_{-\pi}^{\pi} f(s) cos(\omega_j s)\, \mathrm{d}s \tag{4.32}$$

$$B_{m_j} \approx \frac{1}{2\pi} \int_{-\pi}^{\pi} f(s) sin(\omega_j s)\, \mathrm{d}s \tag{4.33}$$

The model function is then decomposed a second time using the Fourier-Haar wavelet decomposition [78]:

$$f(\mathbf{X}) = f_0 + \sum_{i=1}^{n} f_i(X_i) + \sum_{i<j}^{n} f_{ij}(X_i, X_j) + ... + f_{12...n} \tag{4.34}$$

4.3 Results

Several years ago a site has began pumping tests at wells located on the site property with a chromium plume in a regional aquifer. The purpose of pumping is to understand the properties of the plume and evaluate the potential of the pumping to remove chromium because the local concentrations of chromium began to exceeded the limits. Thus, a network of 20 monitoring physical wells was built and used to evaluate, monitor, and eventually mitigate the concentrations of chromium.

The purpose of using SVR in this problem is to build a surrogate model of set of these wells, using only a limited amount of experimental data and simulation results. Below, we use data from a group of four physical wells with 10 input parameters (the time was treated also as a parameter). We train and build an SVR model on this training set and check its predictions with the real measured concentrations and on a set of simulation data derived by the real physical

model developed specifically for the site chromium plume problem. Finally, we performed global sensitivity analysis on both a) the physical model of these wells developed previously and b) on our new SVR model. The comparison of the GSA results in these two cases demonstrates the feasibility and accuracy of the new SVR model as a fast tool for sensitivity analysis.

4.3.1 The SVR model of the chromium plume problem

We build an SVR based surrogate model that describe accurately the site pumping wells based on a training data set derived both via simulations and measurements. Our SVR trainer was coded in Julia, an advanced high-level dynamic high-performance scientific programming language developed recently by MIT [13], and based on the quadratic programming algorithm quadprog [85]. The minimization procedure (described in Methods), needed to find the supporting vectors, was performed using the **Ipopt** Julia package. However, to be able to use this SVR trainer code and to build our SVR model we need first to define several parameters needed to build the SVR model. The non-linear regression method of SVR rely on a set of hyperparameters (tube sensitivity ε, bounds for trade-off parameter C, and kernel width for RBF γ) which optimize the objective function L. Choosing the best hyperparameters for our dataset is not a trivial task, because we need to analyze their effect on the regression accuracy and how to choose an admissible range of parameters. A standard way of finding these optimal hyperparameters is by doing a grid search, i.e. systematically evaluating each possible combination of parameters within a given range.

4.3.2 The parameters C, ε, and γ

We need first to asses the parameters: C and ε used in (4.3) as well as the Gaussian kernel parameter γ that appears in (4.18). The parameters C and ε control the trade-off between the over-fitting and knowledge in the SVR model. Specifically, a small constant C leads to

a relatively flatter prediction (more emphasis on minimizing $\frac{1}{2}\|\omega\|^2$), while a larger constant C will lead to a closer fitting of the data (more emphasis on minimizing $\sum_{i=1}^{l}(\xi_i^+ + \xi_i^-)$). The parameter ε estimates how closely we have to reproduce the training data set. Usually, the effort is to choose C and ε that will produce an SVR model with the best possible generalization. The γ parameter defines the distance of the influence of the training set. The behavior of the SVR model is very sensitive to the γ parameter. If γ is too large, the area of influence of each support vector only includes the support vector itself and C will be not able to prevent overfitting. When γ is very small, the model is too constrained and cannot capture the whole complexity of the data. In this case the region of influence of any selected support vector would include almost the whole training set. A low C makes the surface smooth, while a high C classifies all training examples correctly by giving the model freedom to select more support vectors samples. Thus, the choices of the C and γ parameters are interrelated. The performances of every SVR model highly depends on the choice of these parameters [65]. For our SVR model, we set the value of the parameter ε between $\varepsilon = 2^{-7}$ to 2^{-3} , as in order to perfor a 3D search between all available parameters.

For the trade-off parameters C, ε and kernel parameter γ we utilized a grid search cross-validation strategy, following the standard protocol [45]. The grid search method consists in varying the parameters C, ε and γ with exponentially growing sequences of values. For C, we start from $C = 2^8$ and stop at 2^{15}; for γ, we start at $\gamma = 2^{-7}$ and stop at 2^0 [22]. To derive the parameters C and γ for every fixed value of ε we applied a standard minimization procedure and create a heatmap, Fig. 4.3, that illustrates the results. Thus, Figure 4.3 is a heatmap that demonstrates the SVR cross-validation accuracy as a function of the choice of C and γ with the best choise of ε equal 2^{-5}. The color corresponds to the value of the Mean Square Error (MSE), which is defined as the mean of the square of errors by which predicted results obtained by our

SVR model differ from actual values of the expected quantity, that is,

$$MSE = \frac{1}{n}\sum_{i_1}^{i=n}(e_y - p_y)^2 \tag{4.35}$$

where p_y is the predicted output calculated by the surrogate model function and e_y is the real expected output. The point on the heatmap with coordinates (C, γ) that corresponds to the smallest value of the MSE is considered optimal.

We can see on the heatmap that there are several good SVR models on an upper diagonal of C and γ. Lower γ values gives us smooth SVR models which can be made more complex by selecting a larger number of support vectors with larger C values. For some median values of γ we get equally good performing models when C becomes very large: it is not necessary to regularize the model by limiting the number of support vectors. On the other hand, if we use a lower value of C to limit the number of support vectors our SVR model will use less memory and will be faster in producing predictions.

Based on the heatmap, for our SVR model we chose one (minimum) value of MSE equal 7.35 with corresponding optimal parameters (C, γ) with values of (2^5, 1).

We also going to use additional criteria for model validation and to evaluate the prediction results by the following measures such as squared correlation coefficient R^2:

$$R^2 = \frac{(n\sum_{i_1}^{i=n} e_y p_y - \sum_{i_1}^{i=n} e_y \sum_{i_1}^{i=n} p_y)^2}{(n\sum_{i_1}^{i=n} e_y^2 - (\sum_{i_1}^{i=n} e_y)^2)(n\sum_{i_1}^{i=n} p_y^2 - (\sum_{i_1}^{i=n} p_y)^2)} \tag{4.36}$$

This coefficient varies in the interval $[0, 1]$ with 1 being the best possible value achievable, it does not depend on the scale of the output, and it indicates how well the SVR model fit the original data. For the one well using the above listed parameters we achieved result of $R^2 = 0.999791$.

4.3.3 The number of the data points in the training set

The final question, before to build our SVR model, is how big should be our training sets, to make the best predictions.

We can find this minimal number of points in the SVR training subset by investigating how our SVR model performs when it was trained on various number of points, that is, using consecutively a number of data points $N_t = 10, 20, 30, 50, 75, 100, 150, 200, 250, 300$, and compare the performance. Specifically, for each N_t, we built and trained an SVR model and then the SVR model is used to predict a larger data set of 5000 data points and compared its predictions with the corresponding data points obtained with the real physical model. Again, the criterion of this performance is the calculated MSE. As shown in Figure (**??**), MSE is large when a very small N_t is used, then MSE decreases with the increase of Nt. When Nt reaches $\sim$100, the variation of MSE tend to be slowed down and the MSE reach a plateau. Hence, considering a maximum of the speed of calculations, N_t =100 was utilized in our SVR model.

4.3.4 SVR model trained on 1 well

We first trained an SVR model on a training set derived from one well. Taking a sample data from one of the wells, we wanted to visualize our SVR model and compare its predictions with experimental data points. The specific goal here is to show how the concentration of chromium progresses with time up to 50 months and how well the SVR model matches with real data. For visualizing purposes, for an input parameter we chose only the time. In this case, the training set contained 12 data points randomly distributed over the whole time domain. We built and trained an SVR model on this set, and after that produced with this model 500 new data points (the red points on the Figure 4.6), and compared these predictions with the green line containing 50 points of real data. As it can be seen, all the points lie inside of the ε-tube and our SVR model predicts very well the real data.

4.3.5 SVR trained on 4 wells

The next step for us was to train and to build SVR model on multiple wells. Since our task was very computationally demanding, we needed to speed up the process of building the SVR model. One way of doing that is using using the best open source machine-learning library LIBSVM for building supporting vector machines (SVM) for regression models. In general, LIBSVM implements simple minimization based on the quadratic programing and it was built for nonlinear SVMs. We implemented LIBSVM in Julia language that as fast as C but has simple syntax similar to the syntax of MATLAB and Python. Having that transformation helped us to preform grid search on 4 wells with varying C, ε and γ. After getting the best results from the heatmap (Figure 4.4), randomly chose 4 wells (out of given 20) that have the closest coordinates, trained and built SVR model on these 4 wells and produced predictions which compared with the transport of 4 wells simulated by Anasol ([90]). The The MSE of the prediction rate was 13 and the mean square error $R^2 = 0.990654$, which demonstrates that our SVR surrogate model can be very accurate if compared with experimental data points and simulation data obtained by physical models.

4.3.6 Sensitivity results

Figure 4.7 demonstrates the main and total sensitivity indices for the parameters ((A)-(G)) that were calculated using both the real and surrogate models. In most plots the sensitivity indices calculated using the surrogate model are almost indistinguishable from that of the original model, that we can see a comparison on Table 2. The mean square error (MSE) for main and total sensitivity indices calculated using the original model and SVR is tabulated below. The errors were calculated after truncating the first four data points, as these points are undefined in the original model.These results provide confidence that predictions based on the surrogate model within the prescribed parameter ranges are extremely reliable. Model evaluations for $t \leq 4$ were

undefined and excluded from figures.

Featured below is a figure of spaghetti plots, showing the range in model output from varying a single parameter at a time in Figure 4.8. Each parameter was varied in a range centered around their initial value: $(P_{init} \pm pP_{init})$ where P_{init} is the initial value of said parameter and p is a percentage. We show these variations in model output to illustrate that our range of parameter choices was not too strictly constrained ; even when varying seven parameters simultaneously over the ranges illustrated, the SVR surrogate model was still able to predict accurate model results. Similar plots were created using the surrogate model, but are not shown as there was no visible difference between the variation in model output.

4.4 Conclusion

In this work we employed surrogate modeling via support vector regression (SVR) and global sensitivity analysis (GSA) using the extended Fourier amplitude sensitivity test (eFAST). Both procedures have been developed parallel in Julia language, a relatively new high-level language created at MIT. The final result of this project aims to demonstrate the power and accuracy of applying both SVR and eFAST to a highly nonlinear geophysical model. Our study leads to the following major conclusions:

- As a result we got an extremely fast method of performing GSA, allowing analyses that would have previously been impractical to execute.
- SVR and eFAST algorithms are incorporated into the MADS (Model Analyses & Decision Support) Julia toolbox.
- We analyzed how surrogate models based on support vector regression (SVR) perform when they are applied to approximate the model-predicted behavior of complex time- and scale-dependent contaminant transport in an geologic porous medium (aquifer).

- A comprehensive analysis of the model's output and sensitivity indices can be accurately calculated with drastically lower costs.

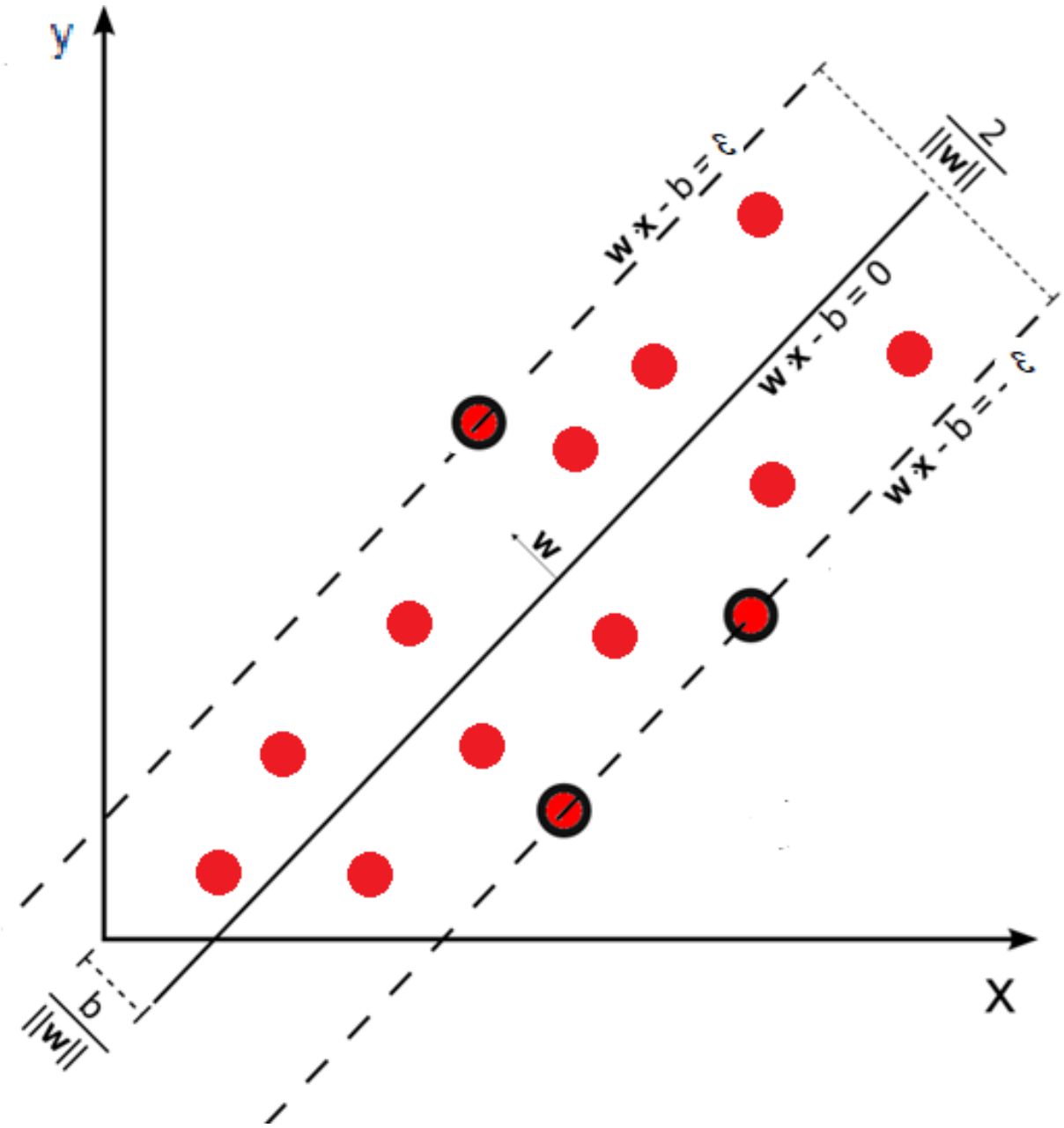

Figure 4.1: One-dimensional Linear Supporting Vector Regression model, where b is the parameter and w is the width of the $\varepsilon-$tube .

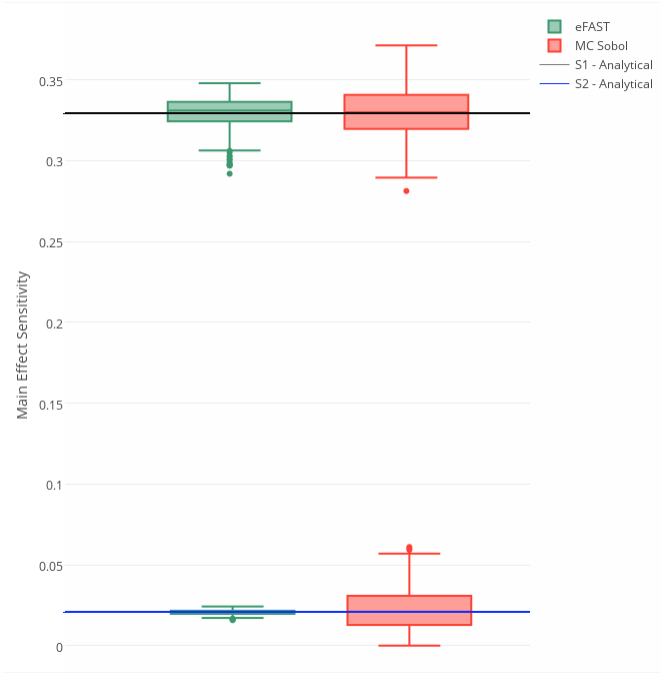

Figure 4.2: Comparison between Monte Carlo and eFAST methods, green bar is the eFast, red bar is the MC Sobol methods.

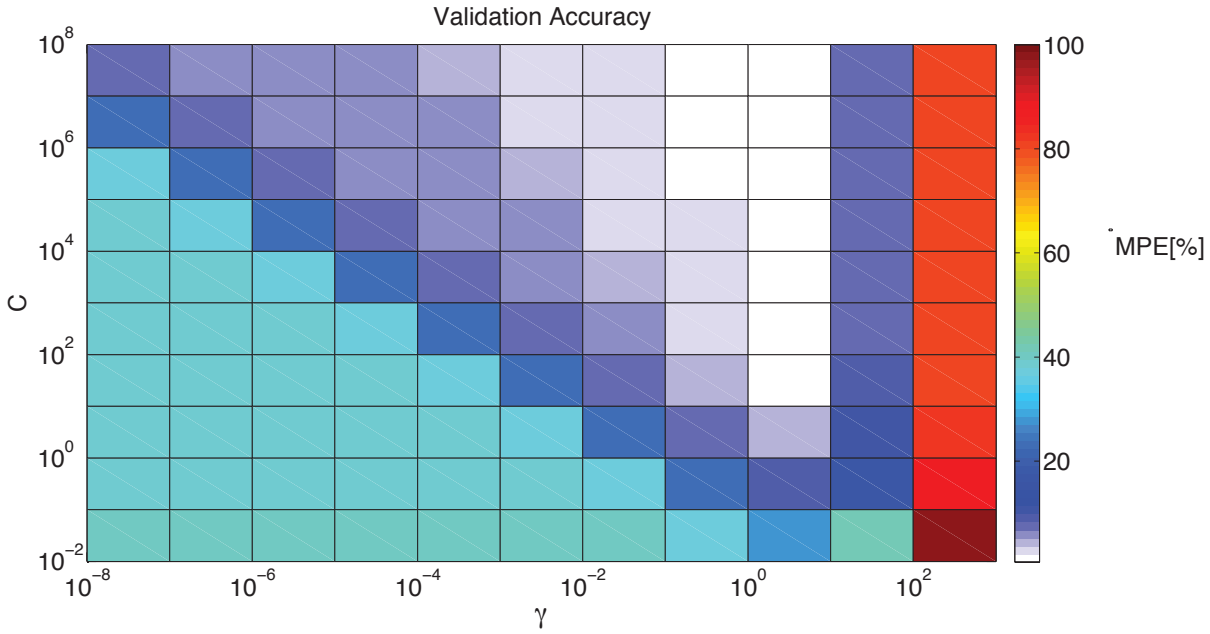

Figure 4.3: The heatmap of the SVR for one well as cross-validation accuracy as a function of (C, γ).

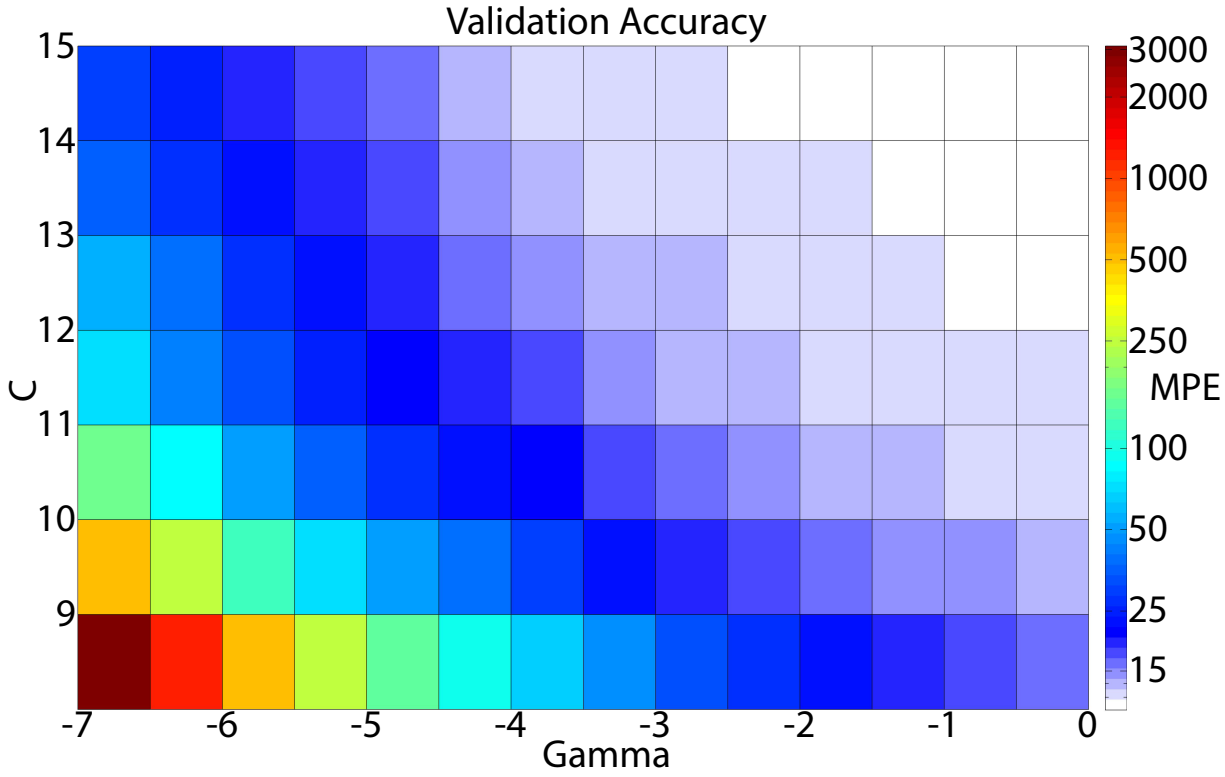

Figure 4.4: The heatmap of the Support Vector Regression for four wells as cross-validation accuracy as a function of (C, ε and γ).

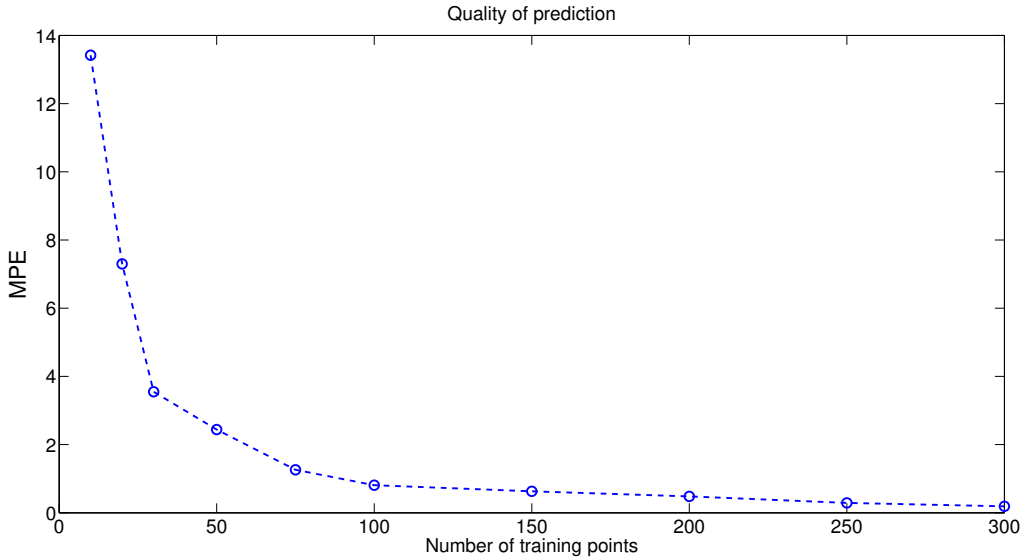

Figure 4.5: The optimal number of training sets for Support Vector Regression one well surrogate model.

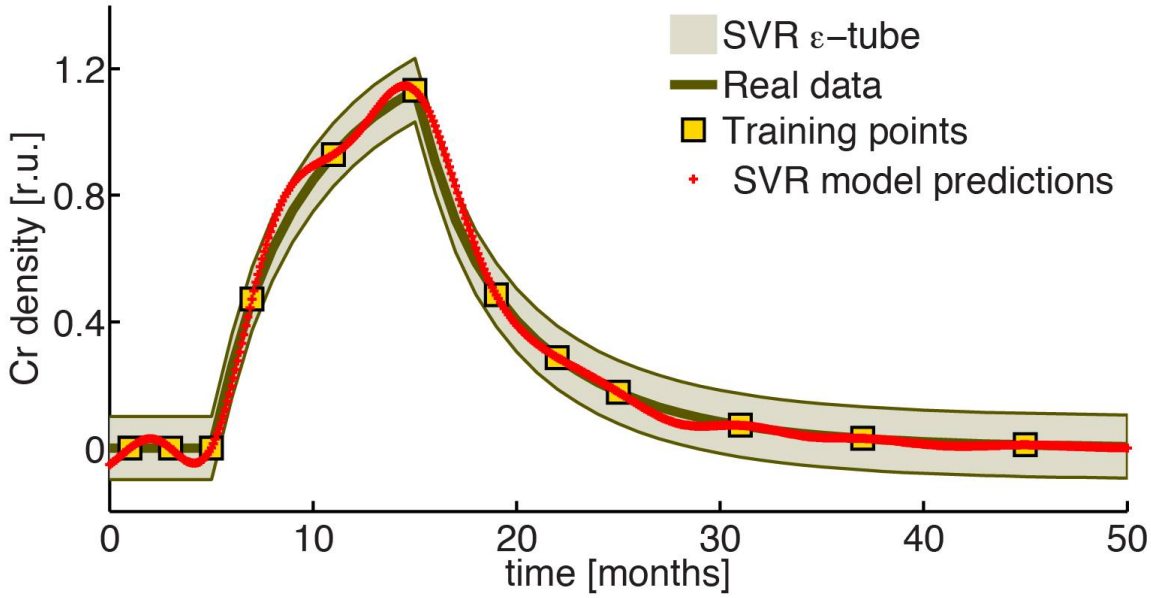

Figure 4.6: SVR Modeling of the chromium density in one well treating time as a parameter, all the training and predicting point lay within the ε tube. The model was trained on 12 training points.

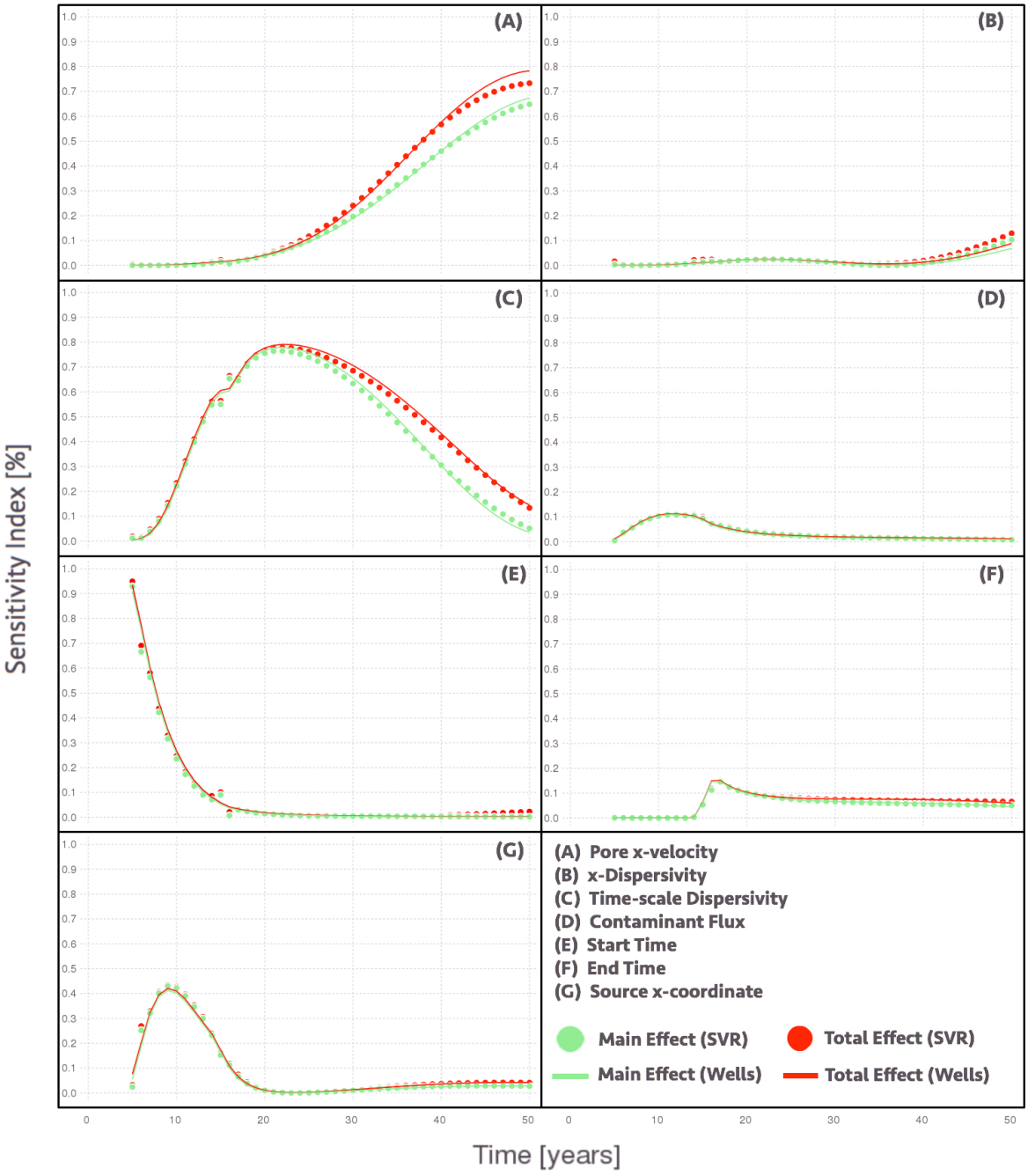

Figure 4.7: Main and total sensitivity indices calculated using the real and surrogate SVR model in one well.

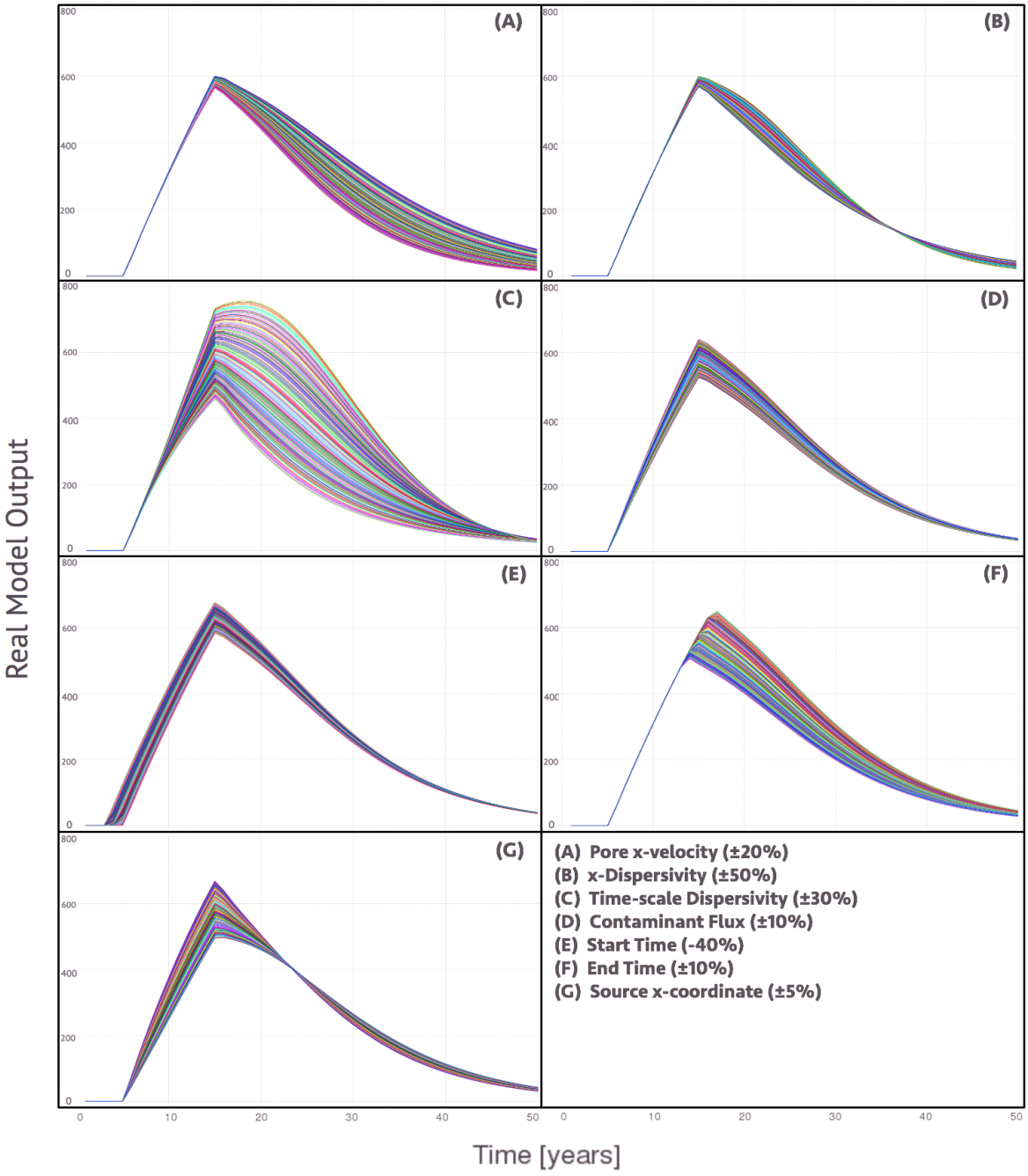

Figure 4.8: Temporal snapshots of spaghetti plots of real model output, varying a single parameter at a time.

Table 4.1: Description of used parameters and bounds of variation (p_{init} - initial value of parameter).

Parameter	Description	Bounds of Variation
v_x	Flow velocity (x-direction) of contaminant from pore	$p_{init} \pm (p_{init} \times 20\%)$
a_x	Contaminant dispersivity (x-direction)	$p_{init} \pm (p_{init} \times 50\%)$
ts_{dsp}	Time-scale dispersivity of contaminant	$p_{init} \pm (p_{init} \times 30\%)$
f	Contaminant flux	$p_{init} \pm (p_{init} \times 10\%)$
t_0	Start time	$[p_{init} - p_{init} \times 40\%, p_{init}]$
t_1	End time	$p_{init} \pm (p_{init} \times 10\%)$
x	X-coordinate of source	$p_{init} \pm (p_{init} \times 5\%)$

Table 4.2: Mean square error between sensitivity indices calculated using real model output vs. SVR model.

Parameter	Main Sensitivity Error	Total Sensitivity Error
Pore x-velocity	3.43%	4.91%
x-Dispersivity	45.6%	44.6%
Time-scale Dispersivity	3.62%	3.31%
Contaminant Flux	7.47%	8.10%
Start Time	7.92%	7.67%
End Time	8.42%	8.59%
Source x-coordinate	8.06%	7.33%

Nataliia Siuliukina, Boian S. Alexandrov, ”Global sensitivity analyses using a surrogate model based on support vector regression approach”, *in preparation*.

Chapter 5

Conclusions

The dissertation leads to the following major conclusions:

1. We developed a hybrid model of propagation of dynamic reactive fronts. A set of numerical experiments for multicomponent reactive flow in a horizontal open fracture is performed to demonstrate that dynamic reactive fronts might not be amenable to Darcy-scale modeling. Our hybrid algorithm couples the pore-scale model in the vicinity of a moving reaction front with the Darcy-scale model elsewhere in the fracture.

2. We showed necessary conditions for the breakdown of Darcy-scale models of dynamic reactive fronts and confirmed that the range of applicability of macroscopic ARDEs and various transport regimes can be adequately described by a phase diagram in a space spanned by the dimensionless Péclet (Pe) and Damkohler (Da) numbers.Our simulations provide an example of the failure of a Darcy-scale model whose parameters fall outside the homogenizability region in this diagram.Its α and β parameters correspond to the faster advection and diffusion at the microscale. The faster advection and diffusion makes homogenizability constraints to be violated and this system is outside of the the homogenizability regime. Faster diffusion rates makes values of Da being larger, while faster advection corresponds to the higher Pe number which forces the failure of macroscopic descriptions

based on local ARDEs leading to an absolute error $E > \varepsilon$ along the fracture.The observed failure of the Darcy-scale model of reaction fronts in an open fracture is not only quantitative but also qualitative. While the Darcy-scale model predicts a Gaussian behavior, the true dynamics is non-Gaussian, as evidenced by the asymmetric, long-tailed concentration profiles.

3. The representational accuracy of our hybrid algorithm is comparable to that of high-fidelity pore-scale simulations at the fraction of computational cost. The hybrid's accuracy (and computational cost) can be increased by enlarging the region of the computational domain, wherein the pore-scale simulations are performed. Alternatively, the hybrid's computational cost can be reduced by decreasing the size of the domain, at the cost of reducing the hybrid's accuracy. Refining the mesh size and time step of the Darcy-scale component of the hybrid is relatively inexpensive but does not yield a significant improvement in the relative model error. The hybrid formulation for the moving dynamic fronts suggests its high adaptability to a wide variety of problems and different numerical schemes.

4. A linear stability analysis of thermo-viscous immiscible flow in two phase homogeneous porous media of rectilinear geometry has been carried out. The growth rates of the physical perturbation disturbances are obtained analytically. Were analyzed the effects of viscosity mobility ratio in both isothermal and non-isothermal cases, representing the effects of mass and heat transfer on the flow viscosity. In isothermal case, the increase of mobility ratio could be caused not only by viscosity ratios but also in the increase of power of relative permeabilities. The quadratic relative permeability $\gamma = 2$ gives the critical number $M = 3$ for the achievement of stability, and with cubic and the fourth order of $\gamma = 3, \gamma = 4$ the ratios of the critical numbers for stability are $M = 10, M = 19$ respectively.

5. We also investigated the conditions for linear stability analysis for the non-isothermal regime. A set of numerical experiments for isothermal and non-isothermal immiscible

flow in a horizontal open fracture is performed to verify the stability regimes.

6. We developed a two phase non-isothermal model for the immiscible fluid flow in porous media. With full nonlinear simulations the conclusions obtained from the linear stability analysis are in concordance with those attained from nonlinear evolution of fingers. Necessary conditions for the breakdown of stability conditions of the immiscible non-isothermal fluid flow in porous media are presented as a phase diagram.

7. The stability of planar fronts in two phase immiscible flow in a porous medium is governed by the mobility difference between the two phases. With quadratic or cubic relative permeability ratios, to stabilize a front in which water is displacing oil, the displacing fluid should be a mixture of oil and water. The analysis indicate the stability conditions for these these fronts.

8. In practical terms, the results of the analysis shows that heat effects make the displacement less unstable in the sense that initial disturbances will have faster growth rates and, hence, one should expect faster growth of instabilities.The amplitude of the instability has the twice of the growth rate in non-isothermal regime versus isothermal regime with analyzing nonlinear velocity. Finally, it should be pointed that these trends will be less noticeable if the rate of heat loss from the fluids to the surrounding medium took into account. In such a case, thermal effects will play a role in the displacement process which becomes dominated by viscous effects.

9. We employed a data driven simulation of surrogate modeling via support vector regression (SVR) and global sensitivity analysis (GSA) using the extended Fourier amplitude sensitivity test (eFAST). The final result of this project aims to demonstrate the power and accuracy of applying both SVR and eFAST to a highly nonlinear geophysical model. As a result we got an extremely fast method of performing GSA, allowing analyses that would

have previously been impractical to execute. SVR and eFAST algorithms are incorporated into the MADS (Model Analyses & Decision Support) Julia toolbox.

10. We analyzed how surrogate models based on support vector regression (SVR) perform when they are applied to approximate the model-predicted behavior of complex time- and scale-dependent contaminant transport in an geologic porous medium (aquifer). A comprehensive analysis of the model's output and sensitivity indices can be accurately calculated with drastically lower costs.

Appendix A

Appendix A

The following is the standard unpreconditioned BiCGStab algorithm [19] for solving a linear system $Ax = b$, using x_0 as the initial vector:

1. $r_0 = b - Ax_0, \quad r^*$ arbitrary, but $(r^*, r_0) \neq 0$
2. $p_0 = r_0$
3. **For** j = 1, 2... **until convergence do**
4. $\alpha_j = \frac{(r^*, r_j)}{(r^*, Ap_j)}$
5. $s_j = r_j - \alpha_j Ap_j$
6. $\omega_j = \frac{(As_j, s_j)}{(As_j, As_j)}$
7. $x_{j+1} = x_j + \alpha_j p_j + \omega_j s_j$
8. $r_{j+1} = s_j - \omega_j As_j$
9. $\sigma_j = \frac{(r_{j+1}, r^*)}{(r_j, r^*)} \cdot \frac{\alpha_j}{\omega_j}$
10. $p_{j+1} = r_{j+1} + \sigma_j (p_j - \omega_j Ap_j)$

11. **end**

The coefficient iterates α_j and σ_j are derived for updating the residual vectors and the search direction vectors. Furthermore, ω_j is defined to minimize the 2-norm of the residual vector r_{j+1} given s_j and As_j .When the algorithm is used with a preconditioner $M \approx A$, the right preconditioning consists of solving the system $AM^{-1}, y = b, y = Mx$. One way to derive the preconditioned iteration is, in the above unpreconditioned version, to replace the symbol A by AM^{-1} and x_j by y_j, and then substitute y_j back by Mx_j. The preconditioner M considered is the incomplete LU factorization (ILU(0)) of the coefficient matrix A. The ILU(0) factorization of A is given by $A = LU$ where L and U are lower triangular and unit upper triangular matrices, Let Z be a subset of the set of indices $\{(i, j) : 1 \geq i, j < N, i \neq j\}$, where $A - LU$ has structural zeros. Let $\bar{Z}$ be the complement of Z. Then the ILU(0) factorization of A satisfies:

For $j = 1, 2.., n$:

- **For** $k = 1, 2.., i-1$ **and** $(i,k) \in \bar{Z}$: $\alpha_{i,k} = \alpha_{i,k}/\alpha_{k,k}$
- **For** $j = k+1, ..., n$ **and** $(i,k) \in \bar{Z}$: $\alpha_{i,j} = \alpha_{i,j} - \alpha_{i,k}\alpha_{k,j}$

Taking the ILU(0) factorization of A as the preconditioning matrix allows the preservation of the exact sparsity pattern in A, and so permits the arrays storing LU and A to share the same array of indices.

Appendix B

Appendix B

To approximate a finite difference scheme we are going to rewrite the system of non-isothermal equation for fluid flow in the following way:

$$m\frac{\partial s}{\partial t} + \nabla \cdot (\phi_1(s) \bigtriangledown p) = 0, \tag{B.1}$$

$$\nabla \cdot (\phi(s) \bigtriangledown p) = 0, \tag{B.2}$$

$$\frac{\partial}{\partial t}((1-s)T + bsT + aT) - \nabla \cdot (\mu_0(T)k_2(1-s) \bigtriangledown pT + bk_1(s) \bigtriangledown pT) = \tilde{\lambda} \bigtriangleup T, \tag{B.3}$$

where

$$a = \frac{\rho_s}{\rho}\frac{1-m}{m}\frac{C_{v_s}}{C_{v_2}}, \quad b = \frac{C_{v_1}}{C_{v_2}}, \quad \tilde{\lambda} = \frac{\lambda \mu_1}{\rho p_0 K C_{v_2}} \tag{B.4}$$

We are going to find a solutions for pressure, saturation and temperature in (i+1/2, j+1/2). First, we are going to find pressure and saturation without temperature dependence, i.e in isothermal case.

To find pressure according to (B.1) we will use local one dimensional difference scheme [73]:

$$\frac{\tilde{p}_{i+1/2,j+1/2} - p_{i+1/2,j+1/2}}{\tau} = -\frac{\tilde{w}_{x,i+1,j+1/2} - \tilde{w}_{x,i,j+1/2}}{h_x}, \tag{B.5}$$

$$\frac{\hat{p}_{i+1/2,j+1/2} - p_{i+1/2,j+1/2}}{\tau} = -\frac{\tilde{w}_{y,i+1/2,j+1} - \tilde{w}_{y,i+1/2,j}}{h_y}, \tag{B.6}$$

$$\tilde{w}_{x,i,j+1/2} = -\frac{2\phi(s_{i+1/2,j+1/2})\phi(s_{i-1/2,j+1/2})}{\phi(s_{i+1/2,j+1/2}) + \phi(s_{i-1/2,j+1/2})} \frac{\tilde{p}_{i+1/2,j+1/2} - \tilde{p}_{i-1/2,j+1/2}}{h_x} \tag{B.7}$$

$$\hat{w}_{y,i+1/2,j} = -\frac{2\phi(s_{i+1/2,j+1/2})\phi(s_{i+1/2,j-1/2})}{\phi(s_{i+1/2,j+1/2}) + \phi(s_{i+1/2,j-1/2})} \frac{\hat{p}_{i+1/2,j+1/2} - \hat{p}_{i-1/2,j+1/2}}{h_y} \tag{B.8}$$

The pressure equations (B.14) are solved using Thomas algorithm [95]. Now we are going to use Finite-volime method scheme [48] to solve the hyperbolic saturation equation (B.1)

$$m\frac{\hat{s}_{i+1/2,j+1/2} - s_{i+1/2,j+1/2}}{\tau} + \frac{K_{i+1,j+1/2} - K_{i,j+1/2}}{h_x} + \frac{G_{i+1/2,j+1} - G_{i+1/2,j}}{h_y} = 0, \tag{B.9}$$

where

$$K_{i,j+1/2} = -F(\hat{s}^x_{upw})\frac{\hat{p}_{i+1/2,j+1/2} - \hat{p}_{i-1/2,j+1/2}}{h_x}, \tag{B.10}$$

$$G_{i+1/2,j} = -F(\hat{s}^y_{upw})\frac{\hat{p}_{i+1/2,j+1/2} - \hat{p}_{i+1/2,j-1/2}}{h_y}, \tag{B.11}$$

For s^x_{upw} approximation we are going to use the upwind scheme

$$\hat{s}^x_{upw} = \begin{cases} \hat{s}_{i-1/2,j+1/2}, & \hat{p}_{i+1/2,j+1/2} - \hat{p}_{i-1/2,j+1/2} < 0 \\ \hat{s}_{i+1/2,j+1/2}, & \hat{p}_{i+1/2,j+1/2} - \hat{p}_{i-1/2,j+1/2} > 0 \end{cases} \tag{B.12}$$

$$\hat{s}^y_{upw} = \begin{cases} \hat{s}_{i+1/2,j-1/2}, & \hat{p}_{i+1/2,j+1/2} - \hat{p}_{i+1/2,j-1/2} < 0 \\ \hat{s}_{i+1/2,j+1/2}, & \hat{p}_{i+1/2,j+1/2} - \hat{p}_{i+1/2,j-1/2} > 0 \end{cases} \tag{B.13}$$

Since the (B.9) is implicit then for linearization we use a Newton Method [54] and for the linear system of equation we use BiCGStab algorithm with the preconditioner ILU(0). (ref appendix A)

To find the temperature, we need to add the heat equation to the system and add the viscosity dependence on temperature. In the same way we'll use Finite-volume method scheme to solve temperature equation in (B.1)

$$\frac{(1-\hat{s}_{i+1/2,j+1/2})\hat{T}_{i+1/2,j+1/2}-(1-s_{i+1/2,j+1/2})T_{i+1/2,j+1/2}}{\tau}+ \tag{B.14}$$

$$+a\frac{\hat{T}_{i+1/2,j+1/2}-T_{i+1/2,j+1/2}}{\tau}+ \tag{B.15}$$

$$+b\frac{\hat{s}_{i+1/2,j+1/2}\hat{T}_{i+1/2,j+1/2}-s_{i+1/2,j+1/2})T_{i+1/2,j+1/2}}{\tau}- \tag{B.16}$$

$$-[\frac{W^x_{i+1,j+1/2}-W^x_{i,j+1/2}}{h_x}+\frac{W^y_{i+1/2,j+1}-W^y_{i+1/2,j}}{h_y}]- \tag{B.17}$$

$$-b[\frac{V^x_{i+1,j+1/2}-V^x_{i,j+1/2}}{h_x}+\frac{V^y_{i+1/2,j+1}-V^y_{i+1/2,j}}{h_y}]= \tag{B.18}$$

$$=\tilde{\lambda}(\frac{\hat{T}_{i+3/2,j+1/2}-2\hat{T}_{i+1/2,j+1/2}+\hat{T}_{i-1/2,j+1/2}}{h_x^2}+\frac{\hat{T}_{i+1/2,j+3/2}-2\hat{T}_{i+1/2,j+1/2}+\hat{T}_{i+1/2,j-1/2}}{h_y^2}), \tag{B.19}$$

where

$$W^x_{i,j+1/2} = \frac{\mu_0(\hat{T}_{i+1/2,j+1/2)) + \mu_0(\hat{T}_{i-1/2,j+1/2)}}{2} * \frac{k_2(1-\hat{s}_{i+1/2,j+1/2)) + k_2(1-\hat{s}_{i-1/2,j+1/2)}}{2} * \tag{B.20}$$

$$* \frac{\hat{p}_{i+1/2,j+1/2)} + \hat{p}_{i-1/2,j+1/2}}{2} * \frac{\hat{T}_{i+1/2,j+1/2} + \hat{T}_{i-1/2,j+1/2}}{2}, \tag{B.21}$$

$$W^y_{i+1/2,j} = \frac{\mu_0(\hat{T}_{i+1/2,j+1/2)) + \mu_0(\hat{T}_{i+1/2,j-1/2)}}{2} * \frac{k_2(1-\hat{s}_{i+1/2,j+1/2)) + k_2(1-\hat{s}_{i+1/2,j-1/2)}}{2} * \tag{B.22}$$

$$* \frac{\hat{p}_{i+1/2,j+1/2)} + \hat{p}_{i+1/2,j-1/2}}{2} * \frac{\hat{T}_{i+1/2,j+1/2} + \hat{T}_{i+1/2,j-1/2}}{2}, \tag{B.23}$$

In the same manner,

$$V^x_{i,j+1/2} = \frac{k_1(\hat{s}_{i+1/2,j+1/2)) + k_1(\hat{s}_{i-1/2,j+1/2)}}{2} * \tag{B.24}$$

$$* \frac{\hat{p}_{i+1/2,j+1/2)} + \hat{p}_{i-1/2,j+1/2}}{2} * \frac{\hat{T}_{i+1/2,j+1/2} + \hat{T}_{i-1/2,j+1/2}}{2}, \tag{B.25}$$

$$V^y_{i+1/2,j} = \frac{k_2(1-\hat{s}_{i+1/2,j+1/2)) + k_2(1-\hat{s}_{i+1/2,j-1/2)}}{2} * \tag{B.26}$$

$$* \frac{\hat{p}_{i+1/2,j+1/2)} + \hat{p}_{i+1/2,j-1/2}}{2} * \frac{\hat{T}_{i+1/2,j+1/2} + \hat{T}_{i+1/2,j-1/2}}{2}, \tag{B.27}$$

We use the Finite-volume scheme for temperature (B.14)- (B.24) using Newton linearization method and for the system of linear equations are solved by BiCGStab algorithm with the preconditioner ILU(0).

Bibliography

[1] S. T. . K. P.-S. C. A. Saltelli. A quantitative model-independent method for global sensitivity analysis of model output. *Technometrics*, 1999.

[2] M. Ahmed and N. Qin. Surrogate-based aerodynamics design optimization: Use of surrogates in aerodynamics design optimization. In *13th International Conference on Aerospace Science & Aviation Technology, Cairo, Egypt*, pages 26–28, 2009.

[3] F. J. Alexander, A. L. Garcia, and D. M. Tartakovsky. Algorithm refinement for stochastic partial differential equations: I. linear diffusion. *Journal of Computational Physics*, 182(1):47–66, 2002.

[4] F. J. Alexander, A. L. Garcia, and D. M. Tartakovsky. Algorithm refinement for stochastic partial differential equations: Ii. correlated systems. *Journal of Computational Physics*, 207(2):769–787, 2005.

[5] F. J. Alexander, D. M. Tartakovsky, and A. L. Garcia. Noise in algorithm refinement methods. *Computing in science & engineering*, 7(3):32–38, 2005.

[6] G. Archer, A. Saltelli, and I. Sobol. Sensitivity measures, anova-like techniques and the use of bootstrap. *Journal of Statistical Computation and Simulation*, 58(2):99–120, 1997.

[7] R. Aris. On the dispersion of a solute in a fluid flowing through a tube. *Proc. Roy. Soc. London A*, 235(1200):67–77, 1956.

[8] J. Atmadja and A. C. Bagtzoglou. State of the art report on mathematical methods for groundwater pollution source identification. *Environmental forensics*, 2(3):205–214, 2001.

[9] M. T. Balhoff, S. G. Thomas, and M. F. Wheeler. Mortar coupling and upscaling of pore-scale models. *Comput. Geosci.*, 12(1):15–27, 2008.

[10] G. I. Barenblatt, V. M. Entov, and V. M. Ryzhik. Theory of fluid flows through natural rocks.

[11] I. Battiato, D. M. Tartakovsky, A. M. Tartakovsky, and T. Scheibe. On breakdown of macroscopic models of mixing-controlled heterogeneous reactions in porous media. *Adv. Water Resour.*, 32:1664–1673, 2009.

[12] I. Battiato, D. M. Tartakovsky, A. M. Tartakovsky, and T. D. Scheibe. Hybrid models of reactive transport in porous and fractured media. *Adv. Water Resour.*, 34(9):1140–1150, 2011.

[13] J. Bezanson, S. Karpinski, V. B. Shah, and A. Edelman. Julia: A fast dynamic language for technical computing. *arXiv preprint arXiv:1209.5145*, 2012.

[14] B. E. Boser, I. M. Guyon, and V. N. Vapnik. A training algorithm for optimal margin classifiers. In *Proceedings of the fifth annual workshop on Computational learning theory*, pages 144–152. ACM, 1992.

[15] F. Boso and I. Battiato. Homogenizability conditions for multicomponent reactive transport. *Adv. Water Resour.*, 62:254–265, 2013.

[16] S. E. Buckley, M. Leverett, et al. Mechanism of fluid displacement in sands. *Transactions of the AIME*, 146(01):107–116, 1942.

[17] C.-C. Chang and C.-J. Lin. Libsvm: a library for support vector machines, software (2001), 2004.

[18] C.-C. Chang and C.-J. Lin. Libsvm: A library for support vector machines. *ACM Transactions on Intelligent Systems and Technology (TIST)*, 2(3):27, 2011.

[19] J. Chen, L. C. McInnes, and H. Zhang. Analysis and practical use of flexible bicgstab. *Journal of Scientific Computing*, 68(2):803–825, 2016.

[20] A. J. Chorin. The instability of fronts in a porous medium. *Communications in mathematical physics*, 91(1):103–116, 1983.

[21] R. Chuoke, P. Van Meurs, C. van der Poel, et al. The instability of slow, immiscible, viscous liquid-liquid displacements in permeable media. 1959.

[22] A. Ciccazzo, G. Di Pillo, and V. Latorre. Support vector machines for surrogate modeling of electronic circuits. *Neural Computing and Applications*, 24(1):69–76, 2014.

[23] C. Cortes and V. Vapnik. Support-vector networks. *Machine learning*, 20(3):273–297, 1995.

[24] P. V. Coveney and P. W. Fowler. Modelling biological complexity: a physical scientist's perspective. *J. Roy. Soc. Interface*, 2(4):267–280, 2005.

[25] Z. Danes. Dynamics of lava flows. *Journal of Geophysical Research*, 77(8):1430, 1972.

[26] A. De Wit. Miscible density fingering of chemical fronts in porous media: nonlinear simulations. *Phys. Fluids*, 16(1):163–175, 2004.

[27] A. De Wit. Chemo-hydrodynamic patterns in porous media. *Phil. Trans. R. Soc. A*, 374(2078):20150419, 2016.

[28] A. De Wit and G. Homsy. Viscous fingering in periodically heterogeneous porous media. i. formulation and linear instability. *The Journal of chemical physics*, 107(22):9609–9618, 1997.

[29] C. Deck, C. Ni, K. Vecchio, and P. Bandaru. The response of carbon nanotube ensembles to fluid flow: Applications to mechanical property measurement and diagnostics. *Journal of Applied Physics*, 106(7):074304, 2009.

[30] H. Drucker, D. Wu, and V. N. Vapnik. Support vector machines for spam categorization. *IEEE Transactions on Neural networks*, 10(5):1048–1054, 1999.

[31] R. Farajzadeh, A. Andrianov, and P. Zitha. Investigation of immiscible and miscible foam for enhancing oil recovery. *Industrial & Engineering chemistry research*, 49(4):1910–1919, 2009.

[32] J. Fernandez and G. M. Homsy. Viscous fingering with chemical reaction: effect of in-situ production of surfactants. *J. Fluid Mech.*, 480:267–281, 2003.

[33] C. Fetter. Contaminant hydrogeology. 1999. *Wisconsin University. Pp458. Ed: Mc Graw Hill*.

[34] A. I. Forrester and A. J. Keane. Recent advances in surrogate-based optimization. *Progress in Aerospace Sciences*, 45(1):50–79, 2009.

[35] N. Fujii and S. Uyeda. Thermal instabilities during flow of magma in volcanic conduits. *Journal of Geophysical Research*, 79(23):3367–3369, 1974.

[36] L. Gálfi and Z. Rácz. Properties of the reaction front in an $A + B \rightarrow C$ type reaction-diffusion process. *Phys. Rev. A*, 38(6):3151, 1988.

[37] B. Gaspar, A. Teixeira, and C. G. Soares. Assessment of the efficiency of kriging surrogate models for structural reliability analysis. *Probabilistic Engineering Mechanics*, 37:24–34, 2014.

[38] F. Girosi. An equivalence between sparse approximation and support vector machines. *Neural computation*, 10(6):1455–1480, 1998.

[39] R. J. Glass, G. H. Oosting, and T. S. Steenhuis. Preferential solute transport in layered homogeneous sands as a consequence of wetting front instability. *Journal of Hydrology*, 110(1-2):87–105, 1989.

[40] T. Graf and R. Therrien. Stable–unstable flow of geothermal fluids in fractured rock. *Geofluids*, 9(2):138–152, 2009.

[41] S. R. Gunn et al. Support vector machines for classification and regression. *ISIS technical report*, 14, 1998.

[42] S. P. Gupta and R. A. Greenkorn. An experimental study of immiscible displacement with an unfavorable mobility ratio in porous media. *Water Resources Research*, 10(2):371–374, 1974.

[43] A. Hamdi and I. Mahfoudhi. Inverse source problem in a one-dimensional evolution linear transport equation with spatially varying coefficients: application to surface water pollution. *Inverse Problems in Science and Engineering*, 21(6):1007–1031, 2013.

[44] K. R. Helfrich. Thermo-viscous fingering of flow in a thin gap: a model of magma flow in dikes and fissures. *Journal of fluid mechanics*, 305:219–238, 1995.

[45] C.-W. Hsu, C.-C. Chang, C.-J. Lin, et al. A practical guide to support vector classification, 2003.

[46] M. Islam and J. Azaiez. Miscible thermo-viscous fingering instability in porous media. part 1: Linear stability analysis. *Transport in porous media*, 84(3):821–844, 2010.

[47] M. Islam and J. Azaiez. Miscible thermo-viscous fingering instability in porous media. part 2: Numerical simulations. *Transport in porous media*, 84(3):845–861, 2010.

[48] A. Jameson, W. Schmidt, and E. Turkel. Numerical solution of the euler equations by finite volume methods using runge kutta time stepping schemes. In *14th fluid and plasma dynamics conference*, page 1259, 1981.

[49] J. N. Johnson, P. K. Tang, and C. A. Forest. Shock-wave initiation of heterogeneous reactive solids. *J. Appl. Phys.*, 57(9):4323–4334, 1985.

[50] A. Khalil, M. N. Almasri, M. McKee, and J. J. Kaluarachchi. Applicability of statistical learning algorithms in groundwater quality modeling. *Water Resources Research*, 41(5), 2005.

[51] X. Kong, M. Haghighi, and Y. Yortsos. Visualization of steam displacement of heavy oils in a hele-shaw cell. *Fuel*, 71(12):1465–1471, 1992.

[52] S. Koziel and J. W. Bandler. Space-mapping optimization with adaptive surrogate model. *Microwave Theory and Techniques, IEEE Transactions on*, 55(3):541–547, 2007.

[53] J. Kuang and T. Maxworthy. The effects of thermal diffusion on miscible, viscous displacement in a capillary tube. *Physics of Fluids*, 15(5):1340–1343, 2003.

[54] E. S. Lee. Quasilinearization. In *The Bellman Continuum*, pages 501–550. World Scientific, 1986.

[55] J. Lee. New monte carlo algorithm: entropic sampling. *Physical Review Letters*, 71(2):211, 1993.

[56] Y. Li, X. Shao, and W. Cai. A consensus least squares support vector regression (ls-svr) for analysis of near-infrared spectra of plant samples. *Talanta*, 72(1):217–222, 2007.

[57] A. Mcdowell, S. J. Zarrouk, and R. Clarke. Modelling viscous fingering during reinjection in geothermal reservoirs. *Geothermics*, 64:220–234, 2016.

[58] P. Meakin and A. M. Tartakovsky. Modeling and simulation of pore-scale multiphase fluid flow and reactive transport in fractured and porous media. *Reviews of Geophysics*, 47(3), 2009.

[59] A. Melo, D. Cóstola, R. Lamberts, and J. Hensen. Development of surrogate models using artificial neural network for building shell energy labelling. *Energy Policy*, 69:457–466, 2014.

[60] D. OMalley and V. Vesselinov. Analytical solutions for anomalous dispersion transport. *Advances in Water Resources*, 68:13–23, 2014.

[61] S. Park and J. D. Iversen. Dynamics of lava flow: Thickness growth characteristics of steady two-dimensional flow. *Geophysical Research Letters*, 11(7):641–644, 1984.

[62] F. Parrella. Online support vector regression. *Master's Thesis, Department of Information Science, University of Genoa, Italy*, 2007.

[63] L. D. Plante, P. M. Romano, and E. J. Fernandez. Viscous fingering in chromatography visualized via magnetic resonance imaging. *Chemical engineering science*, 49(14):2229–2241, 1994.

[64] D. Pritchard. The instability of thermal and fluid fronts during radial injection in a porous medium. *Journal of Fluid Mechanics*, 508:133–163, 2004.

[65] S. Razavi, B. A. Tolson, and D. H. Burn. Review of surrogate modeling in water resources. *Water Resources Research*, 48(7), 2012.

[66] A. Riaz and H. A. Tchelepi. Linear stability analysis of immiscible two-phase flow in porous media with capillary dispersion and density variation. *Physics of Fluids*, 16(12):4727–4737, 2004.

[67] A. Riaz and H. A. Tchelepi. Numerical simulation of immiscible two-phase flow in porous media. *Physics of Fluids*, 18(1):014104, 2006.

[68] B. Rosenbaum and V. Schulz. Efficient response surface methods based on generic surrogate models. *SIAM Journal on Scientific Computing*, 35(2):B529–B550, 2013.

[69] D. Roubinet and D. M. Tartakovsky. Hybrid modeling of heterogeneous geochemical reactions in fractured porous media. *Water Resour. Res.*, 49(12):7945–7956, 2013.

[70] P. G. Saffman and F. S. G. Taylor. The penetration of a fluid into a porous medium or hele-shaw cell containing a more viscous liquid. In *Dynamics of Curved Fronts*, pages 155–174. Elsevier, 1988.

[71] M. Saghir, O. Chaalal, and M. Islam. Numerical and experimental modeling of viscous fingering during liquid–liquid miscible displacement. *Journal of Petroleum Science and Engineering*, 26(1-4):253–262, 2000.

[72] A. Samarskii. Introduction to the theory of difference schemes [in russian], moscow (1971). *Google Scholar*, page 550.

[73] A. A. Samarskii. Local one dimensional difference schemes on non-uniform nets. *USSR Computational Mathematics and Mathematical Physics*, 3(3):572–619, 1963.

[74] B. Scholkopf and A. J. Smola. *Learning with kernels: support vector machines, regularization, optimization, and beyond*. MIT press, 2001.

[75] A. Shafiei and M. B. Dusseault. Geomechanics of thermal viscous oil production in sandstones. *Journal of Petroleum Science and Engineering*, 103:121–139, 2013.

[76] H. R. SHAW. Rheology of basalt in the melting range. *Journal of Petrology*, 10(3):510–535, 1969.

[77] A. J. Smola and B. Schölkopf. A tutorial on support vector regression. *Statistics and computing*, 14(3):199–222, 2004.

[78] R. S. Stanković and B. J. Falkowski. The haar wavelet transform: its status and achievements. *Computers & Electrical Engineering*, 29(1):25–44, 2003.

[79] Y. Tang, A. J. Valocchi, and C. J. Werth. A hybrid pore-scale and continuum-scale model for solute diffusion, reaction, and biofilm development in porous media. *Water Resources Research*, 51(3):1846–1859, 2015.

[80] S. R. Tariq, M. H. Shah, N. Shaheen, M. Jaffar, and A. Khalique. Statistical source identification of metals in groundwater exposed to industrial contamination. *Environmental Monitoring and Assessment*, 138(1-3):159–165, 2008.

[81] A. M. Tartakovsky, P. Meakin, T. D. Scheibe, and R. M. E. West. Simulations of reactive transport and precipitation with smoothed particle hydrodynamics. *Journal of Computational Physics*, 222(2):654–672, 2007.

[82] A. M. Tartakovsky, D. M. Tartakovsky, T. D. Scheibe, and P. Meakin. Hybrid simulations of reaction-diffusion systems in porous media. *SIAM J. Sci. Comput.*, 30(6):2799–2816, 2008.

[83] S. Taverniers, F. J. Alexander, and D. M. Tartakovsky. Noise propagation in hybrid models of nonlinear systems: The ginzburg–landau equation. *Journal of Computational Physics*, 262:313–324, 2014.

[84] P. Tomin and I. Lunati. Hybrid multiscale finite volume method for two-phase flow in porous media. *J. Comput. Phys.*, 250:293–307, 2013.

[85] O. Toolbox. Users guide, the mathworks. *Inc.: Natick, MA, USA*, 2010.

[86] W. Um, R. J. Serne, S. B. Yabusaki, and A. T. Owen. Enhanced radionuclide immobilization and flow path modifications by dissolution and secondary precipitates. *Journal of environmental quality*, 34(4):1404–1414, 2005.

[87] P. Van Leemput, C. Vandekerckhove, W. Vanroose, and D. Roose. Accuracy of hybrid lattice boltzmann/finite difference schemes for reaction-diffusion systems. *Multiscale Modeling & Simulation*, 6(3):838–857, 2007.

[88] V. N. Vapnik and V. Vapnik. *Statistical learning theory*, volume 1. Wiley New York, 1998.

[89] V. Vesselinov and D. Harp. Model analysis and decision support (mads) for complex physics models. In *XIX International conference on water resources-CMWR*, 2012.

[90] V. Vesselinov, D. OMalley, B. Alexandrov, and B. Moore. Reduced order models for decision analysis and upscaling of aquifer heterogeneity (invited), 01 2016.

[91] B. J. Wagner. Simultaneous parameter estimation and contaminant source characterization for coupled groundwater flow and contaminant transport modelling. *Journal of Hydrology*, 135(1-4):275–303, 1992.

[92] D. Wall and S. Wilson. The linear stability of channel flow of fluid with temperature-dependent viscosity. *Journal of Fluid Mechanics*, 323:107–132, 1996.

[93] J. H. Walther, T. Werder, R. Jaffe, and P. Koumoutsakos. Hydrodynamic properties of carbon nanotubes. *Physical Review E*, 69(6):062201, 2004.

[94] Y. Wang, C. Zhang, N. Wei, M. Oostrom, T. W. Wietsma, X. Li, and A. Bonneville. Experimental study of crossover from capillary to viscous fingering for supercritical co2–water displacement in a homogeneous pore network. *Environmental science & technology*, 47(1):212–218, 2012.

[95] J. Weickert, B. T. H. Romeny, and M. A. Viergever. Efficient and reliable schemes for nonlinear diffusion filtering. *IEEE transactions on image processing*, 7(3):398–410, 1998.

[96] J. Weston, S. Mukherjee, O. Chapelle, M. Pontil, T. Poggio, and V. Vapnik. Feature selection for svms. In *Advances in neural information processing systems*, pages 668–674, 2001.

[97] S. Whitaker. *The method of volume averaging*, volume 13. Springer, 1998.

[98] Y. Yortsos and F. Hickernell. Linear stability of immiscible displacement in porous media. *SIAM Journal on Applied Mathematics*, 49(3):730–748, 1989.

[99] M. Zayernouri, S.-W. Park, D. M. Tartakovsky, and G. E. Karniadakis. Stochastic smoothed profile method for modeling random roughness in flow problems. *Comput. Meth. Appl. Mech. Eng.*, 263:99–112, 2013.